Imperial College London
Department of Mechanical Engineering
Exhibition Road, London, SW7 2AZ, UK

On the Mechanics of Oscillating Flames

Martin Jurisch

October 2015

Submitted in part fulfilment of the requirements for the degree of Doctor of Philosophy in Mechanical Engineering of Imperial College London

Declaration of Originality

I declare that the work presented in this thesis is my own and expressed in my own words except where declared otherwise. Any work used by any other author(s) in any form has been properly acknowledged where used. A list of all the references used has been included. This work has not already been submitted for any other degree and is not being submitted concurrently for any other degree.

London, October 2015
Martin Jurisch

Copyright Declaration

London, October 2015
Martin Jurisch

Abstract

The major drive to advance the understanding of flames comes from industry as many technical devices propelled by flames are in constant need of design revisions and efficiency improvements. Lean-premixed combustion technology was one of such areas, which saw major advancements. Unfortunately, combustion devices operating in premixed mode often exhibit undesired flame oscillations, which may lead to damage or even failure of the combustor. The present work is dedicated to better understanding and predicting flame oscillation. A modelling framework based on high-order accurate Discontinuous Galerkin methods is presented to investigate the interaction of steadily propagating flames with pressure waves. The analysis of the results show that the time scale associated with the pressure wave incident upon the flame must be of the same order as the time scales in the primary reaction zone to lead to partial wave reflection and wave transmission at the flame. Hence providing a mechanism for initiating flame oscillation.

The predictive capabilities of the Large Eddy Simulation technique in conjunction with the Probability Density Function model of the unresolved turbulence-chemistry interaction are demonstrated in the simulation of flame oscillation in industrially relevant combustors. Two test cases with increasing complexity are considered: a forced oscillating flame in a bluff-body stabilised combustor, and a self-excited flame oscillation in a swirl combustor with complex geometry. Good agreement between the measurements and the simulations is obtained. The flame dynamics are well captured by both simulations. The results obtained in the study of the bluff-body flame are used to identify suitable chemical markers which correlate well with the total heat release rate. The product of molecular oxygen and the ketenyl radical is found to correlate better with the total heat release rate than the commonly used formaldehyde-based markers in the investigated premixed fuel-lean ethylene-air flame. In the case of the swirl burner the predictions lead to the suggestion of a self-excited flame oscillation in the lateral direction as the result of an interaction of the flame with a vortex ring. The difference between the predicted and experimentally determined frequency of oscillation is 11 %.

Acknowledgements

I would like to express my gratitude to my supervisor Professor Bill Jones. I am thankful for his continuous support, guidance, and encouragement during my Ph.D. time. He gave me the essential freedom in my research, that allowed me to explore the topic of combustion. I am also very grateful to my co-supervisor Dr. A. J. Marquis for his assistance with coding and debugging.

I am indebted to my industrial supervisor Dr. Ghenadie Bulat. Without his comprehensive support, this thesis would not be. During my Ph.D. time, Ghena has also become a good friend of mine and I am very thankful for his contributions to all areas of my life.

My time at Imperial was extremely enjoyable in large part due to my research group and friends that I made there. My thanks goes to Dongwon Noh, Timothy Brauner, Fabian Sewerin, Panayiotis Koniavitis, Fabian Denner, Fabian Hampp, and John Pennefather. I am grateful for the time spent with them, discovering the best of London and spending sleepless nights at the university, for fruitful conversations we held in the office and for all great and hard moments we went through.

Finally, I want to say thanks to my family, for their support despite the vast distances between us. A special thanks goes to my beloved wife, who spent so many sleepless nights by my side, being there at the hardest moments, when there was no one to give me answers. And for being my best critic and editor.

I gratefully acknowledge financial support provided by Siemens Industrial Turbomachinery Ltd, Lincoln.

Table of Contents

A. Introduction

Manufacturers of stationary gas turbine combustors are challenged to develop efficient and low-emission combustion devices in order to comply with legislation to reduce carbon emissions. Lean-premixed combustion technology is at the centre of this development, but often exhibits detrimental flame oscillation which adversely affects the performance of the combustion device and may even lead to failure of the entire combustion system. Flame oscillation is characterised by quasi-periodic large-amplitude variations of the fields describing the motion of the mixture, such as temperature, pressure, and velocity, and must clearly be distinguished from irregular fluctuations with comparatively low-amplitude induced by turbulence. The ongoing attempts to gain better understanding of flame oscillation led to a range of literature dealing with the various aspects of predicting and controlling flame oscillation.

A popular approach which belongs to the former category is the so-called Flame Transfer Function (FTF) approach introduced by Tsien [101] and Crocco and Cheng [24]. The FTF is used to characterise the interaction between flames and acoustic waves by measuring the response of the heat release rate to imposed velocity perturbations, *cf.* Duchaine and Poinsot [34]. In this approach the flame is treated as an acoustic element which, when interacting with acoustic waves, may amplify or attenuate the incident acoustic waves. A review on the subject matter is given by Lieuwen [63]. The response of laminar flames to prescribed inflow velocity perturbations in combustors with simple geometries has been studied extensively by both experiment and simulation. Kornilov *et al.* [60] investigated the response of premixed methane-air flames to acoustic waves in a multi-slit Bunsen burner both experimentally and numerically, and obtained comparable results for the FTF. Similar experiments have been conducted by Bourehla and Baillot [13] and Coats *et al.* [22]. The latter work provides a comparison between the measured and predicted FTF and suggests a modelling framework for the FTF in burner designs which render the flame base immobile. Truffin and Poinsot [100] reproduced numerically an experiment on laminar propane-air flames excited by loudspeakers. The authors compare the experimentally determined with the predicted FTF and propose an extended model for the determination of the FTF independent of the acoustic conditions upstream and downstream of the flame position.

Using experiments to study the oscillation of turbulent flames in combustors with complex geometry is often difficult and expensive. Simulations offer a cheaper alternative and produce more information on the flow properties which can then be used to investigate the mechanisms leading to sustained flame oscillation. A well-suited method to simulate turbulent flames is Large Eddy Simulation (LES). A number of investigations [3, 37, 49, 50, 67, 88] have already demonstrated that LES is able to predict flame oscillation and acoustic flow properties in industrial gas turbine combustors. The accuracy of LES for reacting mixtures crucially depends on the representation of the unresolved turbulence-chemistry interaction. Various models, such as the Eddy-Break-Up model, the Artificially-Thickened Flame model and the G-equation model [78, Section 5.4] have been suggested in the literature on turbulent premixed flames. Another model for the

unresolved turbulence-chemistry interaction is the so-called transported Probability Density Function (PDF) approach, which offers a wide range of applicability, including non-premixed, and premixed, as well as stratified and spray combustion, *cf.* Bulat *et al.* [20] and Jones *et al.* [54–56]. The PDF model has thus far not been applied in the simulation of oscillating turbulent flames.

A common practice associated with the control of flame oscillation is to treat the entire combustion system as a dynamical system. This approach permits the application of elements of control theory and can therefore facilitate the development of control strategies to suppress flame oscillation. Control strategies can be distinguished into two categories: passive and active control. Passive control strategies, such as mounting baffles, mufflers and perforated plates optimised for specific operating conditions on the combustor wall, are widely used in the design process to damp flame oscillation. This approach requires *a priori* knowledge of the conditions under which flame oscillation occurs in a given combustor geometry. Major drawbacks of this approach are the costly design process in conjunction with possible performance losses by a change in the operating conditions of the combustor. These limitations led to further examination of the potential of active control strategies, which are intended to suppress flame oscillation over a wide range of operating conditions by parametric control of an actuator modulating the flow field during operation. Excellent reviews on the subject matter are given by Docquier and Candel [30] and Dowling and Morgans [33].

The present work continues on the subject of the prediction of oscillating flames. Essentially two approaches are pursued. The first approach is based on studying the interaction of a single pressure wave with a steadily propagating plane flame. The specific objective is to assess whether flame oscillation is the result of an intrinsic response of the flame, *i.e.* the perturbation of the reaction-diffusion processes in the flame layer, to pressure waves. The investigation is motivated by the experiments of Kaskan [58] and Yang *et al.* [108] on premixed flames propagating in tubes with circular cross-section. After approaching a state of steady propagation, the flames develop suddenly to an unstable regime characterised by an oscillating motion of the flame. The oscillating motion persists only for a short period of time and then fades away to result again in steady flame propagation until the flame reaches the end of the tube. The flame-wave interaction is simulated using a Discontinuous Galerkin method, which is presented in chapter 2. The investigation is still at an early stage, but the initial results suggest that the wave length of the pressure wave incident to the flame must be of the same order as the thickness of the primary reaction zone to lead to wave reflection and transmission at the flame. This may develop into a complex wave pattern which could initiate flame oscillation.

The second approach is based on the use of the LES-PDF method for predicting oscillating flames in combustor configurations relevant to industry. The specific objective is to assess the predictive capabilities of the LES-PDF model in the context of oscillating turbulent flames which is motivated by the continued need for better simulation tools to identify flame oscillation already at the design stage. Two test cases are considered with different level of complexity. The first test case is a bluff-body stabilised premixed flame excited harmonically by loudspeakers modulating the mass flow rate into the combustion chamber. The frequency of the flame oscillation is determined by the excitation signal which serves as a reference time signal to measure the flame response in the combustion chamber. The results of this investigation are presented in chapter 3. The second test case is a swirl-stabilised partially-premixed turbulent flame in the Siemens SGT-100 combustor, which is considerably more challenging to simulate than the previous test case. The

simulation retains the complex geometrical features of the combustor, including the swirl generator, pre-chamber, combustion chamber and transition duct to the exhaust pipe. A weak self-excited flame oscillation is reported in the experiment, which is investigated in more detail. The obtained simulation results suggest a cyclic variation of the total heat release rate, but the resolved time frame is too short to have sufficient statistical reliability. The results of this investigation are presented in chapter 4. Chapter 5 summarises the findings of the present work and gives a brief outlook on future work.

B. Nomenclature

For the most part of the present work formulas are given in the *component-free* or *direct* notation. A quantity associated with a particular constituent of the mixture is identified by placing a German minuscule below the symbol by which it is denoted. Summations over quantities associated with a particular constituent are indicated by a summation sign. Variables are given in the following dimensions

- [T] dimension of time
- [L] dimension of length
- [M] dimension of mass
- [Θ] dimension of temperature
- [C] dimension of the amount of chemical substance

The basis for the notation is as follows

- *Italic letters* $A,\ a, \ldots$, etc. represent scalars and indices of vectors and tensors.
- *Bold-face letters* $\mathbf{A},\ \mathbf{a}, \ldots$, etc. denote tensors, vectors and matrices.
- *German indices* $\mathfrak{a}, \mathfrak{N}, \ldots$ serve to represent enumerative indices (constituents in the mixture), and are not indicating tensor character.

Symbol	Name and first occurrence	Dimension
	Upper-case Roman	
$\breve{\mathbf{U}}_i^k$	Nodal values of the approximate solution, see equation (2.16)	$[-]$
$\mathbf{D}$	Rate of deformation tensor of the mixture, see equation (1.3)	$[\mathsf{T}^{-1}]$
$\mathbf{D}_\mathfrak{a}$	Rate of deformation tensor of the $\mathfrak{a}$th constituent, see equation (A.2)	$[\mathsf{T}^{-1}]$
D^k	Discrete element in DG method, see equation (2.16)	$[-]$
$\mathbf{D}$	Set of diffusive fluxes, see equation (2.15)	$[-]$
$\mathbf{F}$	Set of convective fluxes, see equation (2.15)	$[-]$
$M_\mathfrak{a}$	Molecular weight of the $\mathfrak{a}$th constituent, see equation (A.40)	$[\mathsf{MC}^{-1}]$
$\mathbf{J}_\mathfrak{a}$	Diffusion flux of the $\mathfrak{a}$th constituent, see equation (1.7)	$[\mathsf{ML}^{-2}\mathsf{T}^{-1}]$
$\mathbf{S}$	Set of supply terms, see equation (2.15)	$[-]$
$\mathbf{T}$	Total stress, see equation (1.5)	$[\mathsf{ML}^{-1}\mathsf{T}^{-2}]$
$\mathbf{T}_\mathfrak{a}$	Partial stress, see equation (A.8)	$[\mathsf{ML}^{-1}\mathsf{T}^{-2}]$
$\mathbf{U}$	Set of balanced variables, see equation (2.15)	$[-]$
A_c, A'_c	Pre-exponential factor for the cth reaction, see equation (A.72)	$[\mathsf{T}^{-1}]$
E_c, E'_c	Activation energy for the cth reaction, see equation (A.72)	$[\mathsf{ML}^2\mathsf{C}^{-1}\mathsf{T}^{-2}]$
K	Number of elements, see equation (2.16)	$[-]$
N	Order of the polynomial approximation, $N_p - 1$, see equation (2.16)	$[-]$

N_p	Number of grid points in D^k, see equation (2.16)	$[-]$
$P_c^{\mathfrak{a}}$	Stoichiometric matrix, see equation (A.40)	$[-]$
Q	Heat release rate per unit volume, see equation (2.1)	$[\mathsf{ML}^{-1}\mathsf{T}^{-3}]$
R	Universal gas constant, see equation (A.72)	$[\mathsf{ML}^2\Theta^{-1}\mathsf{C}^{-1}\mathsf{T}^{-2}]$

Lower-case Roman

$c_{\mathfrak{a}}$	Mass fraction of the $\mathfrak{a}$th constituent, see equation (1.2)	$[-]$
$\widehat{c}_{\mathfrak{a}}$	Chemical source term of the $\mathfrak{a}$th constituent, see equation (1.4)	$[\mathsf{ML}^{-3}\mathsf{T}^{-1}]$
$\mathbf{d}_{\mathfrak{a}}$	Density gradient of the $\mathfrak{a}$th constituent, see equation (A.4)	$[\mathsf{ML}^{-4}]$
$\Delta h^0_{\mathfrak{a}}$	Enthalpy of formation, see equation (2.27)	$[\mathsf{L}^2\mathsf{T}^{-2}]$
$\mathbf{g}$	Temperature gradient, see equation (A.4)	$[\Theta\mathsf{L}^{-1}]$
$\widehat{j}_a$	Net reaction rate density of the ath reaction, see equation (A.40)	$[\mathsf{CM}^{-1}\mathsf{T}^{-1}]$
$\widehat{j}_a^{\,b}$	Backward reaction rate density of the ath reaction, see equation (A.70)	$[\mathsf{CM}^{-1}\mathsf{T}^{-1}]$
$\widehat{j}_a^{\,f}$	Forward reaction rate density of the ath reaction, see equation (A.70)	$[\mathsf{CM}^{-1}\mathsf{T}^{-1}]$
$\mathbf{k}$	Modified entropy flux, see equation (A.15)	$[\mathsf{MT}^{-3}\Theta^{-1}]$
v	Flame speed, see equation (2.4)	$[\mathsf{LT}^{-1}]$
$\widehat{\mathbf{m}}_{\mathfrak{a}}$	Momentum supply, see equation (A.8)	$[\mathsf{ML}^{-2}\mathsf{T}^{-2}]$
$n_{\mathfrak{a}}$	Molar concentration of the $\mathfrak{a}$th constituent, see equation (A.71)	$[\mathsf{CL}^{-3}]$
$\mathbf{q}$	Heat flux of the mixture, see equation (1.6)	$[\mathsf{MT}^{-3}]$
q_θ	Thermal conductivity of the mixture, see equation (1.10)	$[\mathsf{MLT}^{-3}\Theta^{-1}]$
$\mathbf{v}_{\mathfrak{a}}$	Velocity of the $\mathfrak{a}$th constituent, see equation (A.1)	$[\mathsf{LT}^{-1}]$
$\mathbf{v}_{\mathfrak{a}\mathfrak{N}}$	Velocity differences, see equation (A.3)	$[\mathsf{LT}^{-1}]$
$\mathbf{v}$	Barycentric velocity, see equation (1.3)	$[\mathsf{LT}^{-1}]$
$c_{p,\mathfrak{a}}$	Heat capacity at constant pressure, see equation (1.12)	$[\mathsf{MLT}^{-3}\Theta^{-1}]$
$h_{\mathfrak{a}}$	Specific free enthalpy of the $\mathfrak{a}$th constituent, see equation (1.9)	$[\mathsf{L}^2\mathsf{T}^{-2}]$
k	Element index, see equation (2.16)	$[-]$
k_c, k'_c	Rate constants for the cth reaction, see equation (A.72)	$[\mathsf{T}^{-1}]$
$m_{\mathfrak{a}}$	Equivalent diffusion coefficient of the $\mathfrak{a}$th constituent, see equation (1.7)	$[\mathsf{L}^2\mathsf{T}^{-1}]$
s	Speed of sound, see equation (2.29)	$[\mathsf{LT}^{-1}]$
$x_{\mathfrak{a}}$	Mole fraction of the $\mathfrak{a}$th constituent, see equation (2.14)	$[-]$

Upper-case Greek

$\Delta h^0_{\mathfrak{a}}$	Heat of formation, see equation (1.12)	$[\mathsf{L}^2\mathsf{T}^{-2}]$
Δ_μ	Viscous boundary layer for plane waves, see equation (2.2)	$[\mathsf{L}]$
Δ_θ	Thermal boundary layer for plane waves, see equation (2.2)	$[\mathsf{L}]$
Δ_ξ	Element size, see equation (2.29)	$[\mathsf{L}]$
Δ_t	Numerical time step, see equation (2.22)	$[\mathsf{T}]$
$\mathbf{\Phi}$	Entropy flux, see equation (A.13)	$[\mathsf{MT}^{-3}\Theta^{-1}]$

Lower-case Greek

α_f	Filter parameter, see equation (A.96)	$[-]$
ϵ	Internal energy of the mixture, see equation (1.6)	$[\mathsf{L}^2\mathsf{T}^{-2}]$
η	Entropy density, see equation (A.13)	$[\mathsf{L}^2\mathsf{T}^{-2}\Theta^{-1}]$
$\gamma^\diamond$	Effective heat capacity ratio, see equation (2.26)	$[-]$

λ	Second viscosity of the mixture, see equation (1.8)	$[\mathsf{ML}^{-1}\mathsf{T}^{-1}]$
$m_{\mathfrak{a}}^{\theta}$	Coefficient of thermal diffusion, see equation (A.30)	$[\mathsf{M}\Theta^{-1}\mathsf{L}^{-1}\mathsf{T}^{-2}]$
μ	Mixture viscosity, see equation (1.8)	$[\mathsf{ML}^{-1}\mathsf{T}^{-1}]$
$\mu_{\mathfrak{a}}^{I}$	Chemical potentials, see equation (A.39)	$[\mathsf{L}^2\mathsf{T}^{-2}]$
$m_{\mathfrak{ab}}^{v}$	Binary drag coefficients, see equation (A.30)	$[\mathsf{ML}^{-3}\mathsf{T}^{-1}]$
π	Thermostatic pressure of the mixture, see equation (1.8)	$[\mathsf{ML}^{-1}\mathsf{T}^{-2}]$
$\pi_{\mathfrak{a}}$	Partial pressures, see equation (A.30)	$[\mathsf{ML}^{-1}\mathsf{T}^{-2}]$
ψ	Free energy, see equation (A.14)	$[\mathsf{L}^2\mathsf{T}^{-2}]$
$\psi_{\mathfrak{a}}$	Free energy of the $\mathfrak{a}$th constituent, see equation (A.81)	$[\mathsf{L}^2\mathsf{T}^{-2}]$
ψ_I	Inner part of the free energy, see equation (A.19)	$[\mathsf{L}^2\mathsf{T}^{-2}]$
ψ_i^k	Basis functions, see equation (2.16)	$[-]$
ρ	Mass density of the mixture, see equation (1.1)	$[\mathsf{ML}^{-3}]$
$\rho_{\mathfrak{a}}$	Mass density of the $\mathfrak{a}$th constituent, see equation (1.1)	$[\mathsf{ML}^{-3}]$
θ	Temperature, see equation (1.10)	$[\Theta]$
φ'	Working of the viscous stresses $\frac{1}{2}\mathrm{tr}\mathbf{TD}$, see equation (2.1)	$[\mathsf{ML}^{-1}\mathsf{T}^{-3}]$
ξ	Characteristic variable, see equation (2.5)	$[\mathsf{L}]$
$\xi_{\mathfrak{ab}}$	Second cross viscosities, see equation (A.30)	$[\mathsf{ML}^{-1}\mathsf{T}^{-1}]$
$\zeta_{\mathfrak{ab}}$	Cross viscosities, see equation (A.30)	$[\mathsf{ML}^{-1}\mathsf{T}^{-1}]$

Symbols

$(\cdot)''$	Fluctuation of $(\cdot)$ about the time average
$(\cdot)'$	Fluctuation of $(\cdot)$ about the phase average
$\mathrm{div}(\cdot)$	Divergence operator in the spatial description, see equation (1.4)
$\dot{\overline{(\cdot)}}$	Time derivative $\partial(\cdot)/\partial t$, see equation (1.4)
$\mathrm{grad}\,(\cdot)$	Gradient operator in the spatial description, see equation (1.3)
$\langle\cdot\rangle_{\gamma}$	Phase average of $(\cdot)$
$\langle\cdot\rangle_{t}$	Time average of $(\cdot)$
$\langle\cdot\rangle_{x}$	Spatial average of $(\cdot)$
$(\cdot)^{\bullet}$	Value of $(\cdot)$ in strong equilibrium, see equation (A.54)
$(\cdot)^{\circ}$	Value of $(\cdot)$ in weak equilibrium, see equation (A.38)
$\mathrm{skw}\,\{\cdot\}$	Skew-symmetric part of a second-order tensor, see equation (A.23)
$\mathrm{sym}\,\{\cdot\}$	Symmetric part of a second-order tensor, see equation (1.3)

Abbreviations

CFD	Compact Finite-Difference
CRZ	Central Recirculation Zone
CVC	Central Vortex Core
DG	Discontinuous Galerkin
FTF	Flame Transfer Function
LES	Large Eddy Simulation
ORZ	Outer Recirculation Zone
OT	Ordinary Thermodynamics
PDF	Probability Density Function
RT	Rational Thermodynamics

1. Flame Characteristics and Field Equations

1.1. General Remarks

Plane flames are similar in kind to shock waves because changes of the thermodynamic fields are confined to a narrow layer. Their structure, however, largely differs. Flames possess a much richer structure than shock waves since not only heat conduction and viscosity play an important role inside this layer, but also mechanical diffusion and chemical reaction. This interplay of different thermodynamic processes makes flames an important and also challenging subject for study.

Flames are distinguished into premixed and non-premixed flames depending on how fuel and oxidiser are brought into contact. If fuel and oxidiser are brought into contact sufficiently far upstream of the flame to allow for complete mixing of the constituents, the flame is called *premixed*. The mixture upstream of a premixed flame is in a state of weak equilibrium because chemical reactions are inhibited through low temperatures. Ignition of the mixture is only possible if heat is supplied to the mixture in order to surpass a critical composition-dependent energy barrier. The flame propagates against the onrushing unburnt mixture after passing the ignition phase and continuously heats up the mixture ahead of the flame to the ignition temperature through heat conduction and diffusion. The fuel is burnt inside the flame layer which sets free the heat of reaction. Hence, flames are not adiabatic. In *non-premixed* flames, fuel and oxidiser are initially separated and only mixing in the flame layer through mechanical diffusion. Chemical reactions proceed only in the immediate neighborhood of the contact zone between fuel and oxidiser and sustain the diffusion of fuel and oxidiser into the flame layer. The products of the chemical reaction diffuse out of the flame layer and get replaced by the reactants. Non-premixed flames cannot propagate into the fuel alone without oxidiser and vice versa. Thus, they are confined to the contact zone between fuel and oxidiser.

A further distinction of flames can be made according to the regime of the fluid motion in which the flame propagates. If a flame propagates into a fluid at rest or into a fluid in laminar motion the flame is said to be *laminar*. Similarly, if the fluid motion is turbulent the flame is said to be *turbulent*. The study of plane laminar flames has received special attention since they are well suited for studying in detail the structure of the flame layer. In such circumstances theories constructed for describing flames can be much easier compared with experiment. Of particular importance are the constitutive equations for the chemical source terms which represent the rate of mass exchanged amongst the constituents through chemical reactions. Plane laminar flames and their constitution also play an important role in the study of flame front instabilities triggered off by the combined effects of reaction and diffusion. Turbulent flames, on the other hand, have wrinkled flame fronts which makes it inherently difficult to analyse them thoroughly. Some tools for establishing a comparison between model and experiment may be borrowed from statistics. A turbulent flame propagates effectively at a higher speed with respect to the

onrushing fluid than a laminar flame if the mixture composition is the same in the two regimes. This is due to the increased surface area of a turbulent flame and enhanced diffusion in the flame layer.

The brief introduction to flames given in this section shall be sufficient to impress upon the reader the necessity to consider a great number of physical processes occurring inside the flame layer when describing the dynamical behaviour of flames. This must be taken into account when addressing the phenomenon of oscillating flames, which is the subject of the next section. A few basic facts about the structure of typical hydrocarbon flame layers are given in section 1.3 to furnish a basis for their phenomenological description in section 1.4.

1.2. Flame Oscillation

The term *flame oscillation* may be applied in two circumstances, which are observed in a number of experiments [58, 87, 108]: the oscillation of cellular structures distributed laterally along the flame layer, and the oscillation of the flame structure as a whole in the longitudinal direction against the flow ahead of the flame. The latter phenomenon is observed in both laminar and turbulent flames. In the context of turbulent flames it is to be understood that longitudinal flame oscillation, and its associated variation of the field variables, exceed identifiably the effective variation of the field variables induced by turbulent fluid motion.

Yang *et al.* [108] demonstrated in an experiment with propane flames propagating in open tubes that lateral and longitudinal flame oscillation may even occur simultaneously. The experiment was carried out by filling the tube with a premixed mixture of propane and air at equivalence ratios in the interval $[1.1, 1.4]$. After the mixture has attained an equilibrium state it is ignited at one end of the tube which generates a flame propagating steadily into the unburnt mixture. When the flame approaches approximately the half length of the tube the flame becomes unstable and departs from the state of steady flame propagation. What follows is a longitudinal flame oscillation which again becomes unstable after a few cycles and evolves quickly into a new regime, a secondary instability, characterised by coexistence of the two forms of flame oscillation. This complex instability is maintained only for a brief period of time and then disappears in favor of steady flame propagation until the flame reaches the opposite end of the tube. The instability likely attenuates because of lack of energy feedback with the environment external to the localised instability, *i.e.* feedback originating from the presence of a wall at the upstream end of the tube. Such an instability may be what Prigogine and Nicolis [80] call a *dissipative structure*; a regime characterised by organised space-time structures, which appear far from equilibrium.

Early experiments by Kaskan [58] show that propane flames propagating in vertical tubes towards the closed bottom end also develop to an oscillating regime after becoming unstable at the half length of the tube. The precise nature of this phenomenon was not fully revealed. Kaskan suggested that the observed longitudinal flame oscillation is the result of an interaction of the flame with the tube wall and proposed a mechanism which relates the flame oscillation to variations of the flame surface area, which are caused by the fluctuating velocity gradient in the boundary layer. Interestingly, in some experiments Kaskan observed what appears to be lateral flame oscillation superimposed to longitudinal flame oscillation just as in the experiment of Yang *et al.*. The phenomenon persists again only for a brief period of time and is then replaced by a flat oscillating flame.

The present work is mainly concerned with the phenomenon of longitudinal flame oscillation. What remains poorly understood to date is the initiation of this process and whether or not the flame oscillation can be understood in purely mechanical terms or necessitates consideration of the intrinsic flame response. For clarification, the term *mechanical response* associates the flame oscillation with the sole existence of strong gradients of temperature, density and mass fractions across the flame layer. In this idealization the flame is conceived of as a singular surface with no internal structure separating two distinct fluid states which depart in different amounts from their respective steady state when being perturbed. Thus the flame speed remains unaltered when the flame is perturbed. The term *intrinsic response* associates the flame oscillation with a change of the flame structure and thus flame thickness and flame speed. In this concept the flame itself functions as a transfer element and may amplify or attenuate perturbations incident to the flame. In the literature longitudinal flame oscillation is primarily associated with the interplay of the heat liberated by chemical reaction and pressure, *c.f.* [31, 63, 74]. Using rather general terms, longitudinal flame oscillation may be described as follows. Pressure waves incident upon the flame interact with the flame layer in such a way that the amplitude of the incident wave is amplified. At the same time the heat liberated by chemical reaction experiences a spontaneous increase. In a closed space this may provide for an energy feedback loop, in which the amplitude of the pressure wave increases asymptotically to an upper limit. This behaviour was indeed observed in an experiment by Searby [86] and bears resemblance of a limit cycle of the pressure. The frequency of oscillation is usually identified as the natural frequency of the structure in which the flame is contained. Dowling [32] adopted the hypothesis that longitudinal flame oscillation is the mechanical response of the flame to pressure waves to develop an analytical model with the result that the flame is excited at all equivalence ratios within the ignition limits. Any perturbation of a steadily propagating flame develops into a limit cycle. This, however, is not confirmed by results of experiment. A similar failure was identified in the Darrieus-Landau theory, which was developed to understand the wrinkling of plane flames. By ignoring exchange processes inside the flame layer it was found that any perturbation leads to an irreversible deformation of an initially plane flame. It thus seems appropriate that any theory which is developed to shed light on the initiation of longitudinal flame oscillation be constructed in such a way as to take into account the exchange processes (*i.e.* chemical reaction and diffusion) inside the flame layer.

When adopting the hypothesis that longitudinal flame oscillation originates from an intrinsic flame response it may be useful to identify parallels with chemical instabilities in homogeneous media and instabilities of the steady states in well-stirred reactors. This brings to the foreground that non-linear differential equations describing reaction-diffusion systems possess rich properties, even in the absence of any two- or three-dimensional effects. Prigogine and Nicolis [80] studied the stability of a simple model reaction-diffusion system far from chemical equilibrium and identified a great variety of structures with space and time organisation. By omitting the diffusion terms the authors showed that the system evolves to an undamped periodic regime which resembles a limit cycle of the mass fractions beyond instability. This regime is attained independently of the initial conditions and therefore constitutes an intrinsic property of the system. When diffusion was included it was demonstrated that the system can attain a regime characterised by concentration waves which are periodic in space and time after the steady state becomes unstable. In the same line of works falls the investigation of Vilyunov and Ryabinin [103] who analysed the existence of oscillatory oxidation of molecular hydrogen, H_2, in a

gas-phase stirred reactor at low pressures near the first and second ignition limits. The authors found that the concentration of molecular oxygen, O_2, plays a decisive role in the initiation of the oscillatory oxidation and accounts for the unique features of the oscillation. In their experimental and numerical studies on oscillatory oxidation of H_2 in well stirred vessels Baulch *et al.* [9] identified the origin of the oscillation in the kinetic interactions. The authors observed oscillatory ignition at and near the second ignition limit as a result of the kinetic competition between the chain branching and chain termination reactions. The oxyhydrogen reaction, H_2-O_2, forms an important part of any detailed reaction mechanism for hydrocarbon flames.

On these grounds it seems reasonable to not exclude *a priori* the intrinsic flame response to pressure waves when analysing the initiation of longitudinal flame oscillation. This implies that the structure of the flame layer must be taken into account when constructing a theory for analysing longitudinal flame oscillation. In order to do so a number of basic facts about the flame layer shall be addressed, which is done in the following section.

1.3. Flame Structure

A typical flame layer is characterised by strong gradients of the mass fractions, velocities and temperature which in turn induce large fluxes of mass, linear momentum and energy. These fluxes vary from constituent to constituent. The term *constituent* or *constituent of the mixture* is used synonymously with atomic or molecular species of the mixture. To illustrate the complex structure of a typical premixed hydrocarbon flame layer Figure 1.1 shows the profiles of the mass fractions and chemical source terms of a few major constituents of the mixture as well as profiles of temperature and the rate at which the heat of reaction is liberated, the *heat release rate*.

The flame layer can be conceived of as being composed of three characteristic zones: a *transport* or *pre-flame zone* (I), a *primary reaction zone* (II), and a *radical recombination* or *secondary reaction zone* (III). In the transport zone the mixture ahead of the flame is heated up to the ignition temperature through the conduction of heat which evolves as the result of the progress of chemical reactions in the primary and secondary reaction zone. Mole fraction differences and energy transfer are induced by diffusion in the absence of chemical reactions. The narrow primary reaction zone is characterised by the creation of radicals which subsequently attack the fuel and initiate the fuel oxidation. In lean and moderately rich hydrocarbon flames the fuel is exclusively attacked by atomic oxygen, O, atomic hydrogen, H, and the hydroxyl radical, OH. These radicals are formed by the chain-branching steps of the oxyhydrogen reaction. This is followed by the oxidation of carbon monoxide, CO, to water, H_2O, and carbon dioxide, CO_2, in the secondary reaction zone. The oxidation of CO may proceed on two ways depending on the concentration of atomic hydrogen or water: by OH radicals (if H, O concentrations larger than 1%), or recombination with atomic oxygen (if H, O concentrations less than 0.01%), *c.f.* Warnatz [105]. The heat release rate attains its maximum in the secondary reaction zone along the major pathway of the CO oxidation.

A plane flame traverses a mixture at rest or steady flow with a constant speed of propagation which depends on the composition, temperature and pressure of the mixture ahead of the flame. The speed of propagation of the flame is simply referred to as *flame speed* in the remainder of this work. If one assumes that the flame thickness is that of the primary reaction zone, which controls the concentration gradients in the flame layer, one may expect that a linear relationship holds between the flame thickness and the flame

speed. This was indeed observed in the analysis of Brown *et al.* [18]. The exchange of linear momentum amongst the constituents through mechanical and thermal diffusion also plays a crucial role in the flame layer. Steep gradients of the mass fractions and temperature sustained by chemical reaction can lead to diffusion velocities which exceed the barycentric velocity by orders of magnitude, see for example the experimental results of Fristrom [38]. From kinetic theory it is known that chemical reactions and transport processes induced by viscosity, diffusion, and heat conduction are dominated by collision of the particles. This implies that these processes correlate with the mean free path and inversely with the total pressure. The combined thickness of the transport and primary reaction zone thus scales linearly with the inverse pressure. This is in contrast to the recombination zone whose thickness was found to vary with the three halves power of the inverse pressure [38]. At sub-atmospheric pressures, the coupling between the primary and secondary reaction zone is not very strong and the secondary reaction zone is only marginally affected by the bimolecular reactions and induced gradients which occur in the primary reaction zone [39]. In fact, the thickness of the secondary reaction zone becomes so large that primarily bimolecular reactions occur because of lack of particle collisions. In contrast, at high pressures (> 10 bar) it becomes increasingly difficult to distinguish between the two reaction zones as they tend to approach one another. This implies that one cannot distinguish between bimolecular and three-body reactions occurring in the primary and secondary reaction zone, respectively.

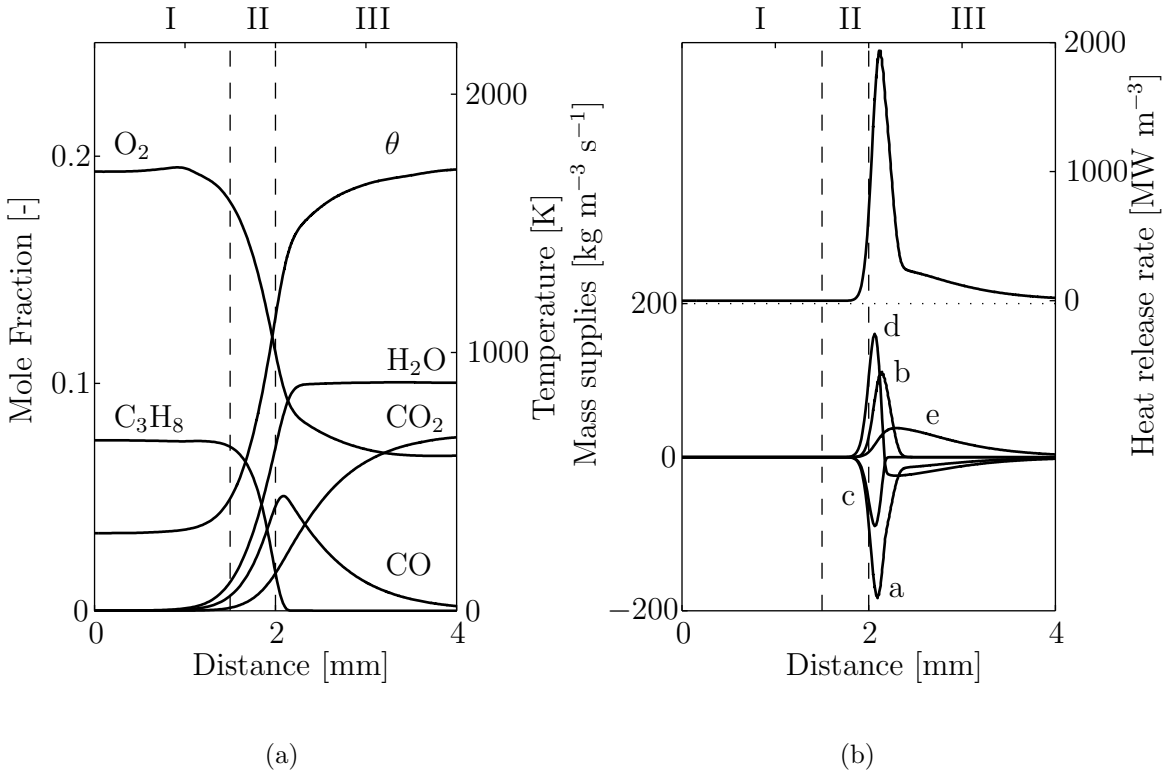

Figure 1.1.: Structure of a premixed propane-air flame layer: (a) mole fraction and temperature profiles; (b) heat release rate and chemical source terms for O_2, H_2O, C_3H_8, CO, and CO_2 (a-e).

1.4. Phenomenological Description

The present section establishes elements of a classical field theory for flames. From the considerations of the preceding section such a theory must account for diffusion, chemical reaction, viscosity and heat conduction. Each constituent of the mixture has its own mass and consequently its own mass density $\rho_{\mathfrak{a}} = \rho_{\mathfrak{a}}(\mathbf{x}, t)$. All constituents are assumed to move at a common speed, the barycentric velocity $\mathbf{v} = \mathbf{v}(\mathbf{x}, t)$. Based on these variables, a few definitions are made:

$$\text{total mass density of the mixture} \qquad \rho \equiv \sum_{\mathfrak{a}=1}^{\mathfrak{N}} \rho_{\mathfrak{a}} \ , \tag{1.1}$$

$$\text{mass fraction of the } \mathfrak{a}\text{th constituent} \qquad c_{\mathfrak{a}} \equiv \frac{\rho_{\mathfrak{a}}}{\rho} \ , \tag{1.2}$$

$$\text{rate of deformation tensor} \qquad \mathbf{D} \equiv \operatorname{sym}\{\operatorname{grad}\mathbf{v}\} \ . \tag{1.3}$$

$\operatorname{sym}\{\cdot\}$ and $\operatorname{grad}(\cdot)$ denote the symmetric part of a second-order tensor $\{\cdot\}$ and the gradient operator in the spatial description. In addition, all constituents are assumed to have the same temperature $\theta = \theta(\mathbf{x}, t)$. The $\mathfrak{N} + 4$ fields $\{\rho_{\mathfrak{a}}, \mathbf{v}, \theta\}$ are governed by the equations of balance of masses for the $\mathfrak{N}$ constituents, and the balance of linear momentum and energy of the mixture. Table 1.1 lists the differential form of these balance equations.

Table 1.1.: List of thermomechanical equations of balance.

Equation	Differential form	Ref.	Number
Balance of mass for the $\mathfrak{a}$th constituent	$\dot{\rho}_{\mathfrak{a}} + \operatorname{div}(\rho_{\mathfrak{a}}\mathbf{v} + \mathbf{J}_{\mathfrak{a}}) = \widehat{c}_{\mathfrak{a}}$	(1.4)	$\mathfrak{N}$
Balance of momentum for the mixture	$\overset{\bullet}{(\rho\mathbf{v})} + \operatorname{div}(\rho\mathbf{v} \otimes \mathbf{v} - \mathbf{T}) = \mathbf{0}$	(1.5)	3
Energy balance for the mixture	$\overset{\bullet}{(\rho\epsilon)} + \operatorname{div}(\rho\epsilon\mathbf{v} + \mathbf{q}) = \operatorname{tr}(\mathbf{TD})$	(1.6)	1
		Sum	$\mathfrak{N} + 4$

Both body force and external heat supply density are neglected in the above set of differential equations. The additional fields $\{\widehat{c}_{\mathfrak{a}}, \mathbf{J}_{\mathfrak{a}}, \mathbf{T}, \epsilon, \mathbf{q}\}$ in (1.4)-(1.6) represent the chemical source terms, diffusion fluxes, total stress, internal energy and heat flux, respectively, for which supplementary relations must be provided. These relations are known as constitutive functionals and take account of the specific material considered.

The chemical source terms for a particular fuel oxidation are modelled using a reaction mechanism which involves a complex chemical analysis to determine the number of independent chemical reactions. Constitutive functionals for the diffusion fluxes, total stress, internal energy and heat flux commonly employed in combustion processes are

Table 1.2.: List of constitutive functionals.

Field	Differential form	Ref.	Number
Diffusion fluxes	$\mathbf{J}_{\mathfrak{a}} = -\rho m_{\mathfrak{a}} \operatorname{grad} c_{\mathfrak{a}}$	(1.7)	$3\mathfrak{N}$
Total stress	$\mathbf{T} = -\pi\mathbf{I} + \lambda\,(\operatorname{tr}\mathbf{D})\,\mathbf{I} + 2\mu\mathbf{D}$	(1.8)	6
Internal energy	$\epsilon = \sum_{\mathfrak{a}=1}^{\mathfrak{N}} (c_{\mathfrak{a}} h_{\mathfrak{a}}) - \frac{\pi}{\rho}$	(1.9)	1
Heat flux	$\mathbf{q} = -q_\theta \operatorname{grad}\theta$	(1.10)	3
		Sum	$3\mathfrak{N} + 10$

Equation (1.7) is FICK's law which leads to the paradox of diffusion, *i.e.* disturbances in concentrations are propagated at infinite velocity. An alternative phenomenological description avoiding this paradox is outlined in section A.1 of appendix A. The coefficients $m_{\mathfrak{a}}$, π, λ, μ and κ in (1.7), (1.8) and (1.9) denote the diffusion coefficient of the $\mathfrak{a}$th constituent into the mixture, the thermostatic pressure of the mixture, bulk viscosity, dynamic viscosity and heat conductivity of the mixture, respectively. λ and μ must satisfy the classical inequalities of DUHEM and STOKES to be consistent with the second axiom of thermodynamics [97]:

$$\mu \geq 0 \;, \qquad\qquad 3\lambda + 2\mu \geq 0 \;. \tag{1.11}$$

$h_{\mathfrak{a}}$, $(\mathfrak{a} = 1, 2, \ldots, \mathfrak{N})$ represents the specific enthalpy of the $\mathfrak{a}$th constituent and can be expressed as the sum of the sensible enthalpy and the enthalpy of formation

$$h_{\mathfrak{a}} = \int_{\theta_0}^{\theta} c_{p,\mathfrak{a}}(\widetilde{\theta}) d\widetilde{\theta} + \Delta h_{\mathfrak{a}}^0 \;, \tag{1.12}$$

where $c_{p,\mathfrak{a}}$ and $\Delta h_{\mathfrak{a}}^0$ are the heat capacity at constant pressure and the enthalpy of formation of the $\mathfrak{a}$th constituent.

2. Interaction of a Flame with a Pressure Wave

2.1. Introductory Remarks

The present chapter describes a numerical set-up to investigate the response of plane premixed flames to pressure waves. The obtained results are analysed to shed light on the possible initiation of flame oscillation by pressure waves. This mechanism has become popular since the early work of RAYLEIGH [81] on sound propagation. In particular, RAYLEIGH [81, §332g]'s paragraph on vibrations maintained by heat became an often cited reference in the field of flame oscillation because for the first time a criterion was stated, which explains how sound emission is maintained by periodic heat transfer from a heat source. RAYLEIGH's criterion was first only formulated verbally and then put into mathematical form by CHU [21]. In the present notation CHU's formulation of RAYLEIGH's criterion may be written as follows

$$\int_v \theta' Q' dv \geq \theta_0 \int_v \varphi' dv + q_\theta^0 \int_v \operatorname{grad}\theta' \cdot \operatorname{grad}\theta' dv \ , \tag{2.1}$$

where θ', Q', and φ' represent 'small' deviations from a uniform temperature, θ_0, and heat release rate per unit volume, Q_0, and the working of the viscous stresses in the disturbance, respectively. The quantity q_θ^0 denotes the uniform thermal conductivity. The sign "=" in (2.1) only holds when the energy in the disturbance does not grow in time. For all other processes the inequality states that the energy in the disturbance must overcome the sum of the working of the viscous stresses and the thermal dissipation so as to grow in time. Except for some special solutions the criterion cannot be used to determine *a priori* whether or not the flame will oscillate. Solutions to the field equations must be sought first or experiments conducted before one can test *a posteriori* whether or not the inequality holds. Moreover, the criterion applies only to the integration domain as a whole, not its individual parts. The boundaries of the integration domain usually coincide with some part of the investigated burner geometry where the conditions are known. Since flame oscillation results from the local interaction of the flame with the fluid motion in the neighborhood of the flame, the criterion is not very helpful to shed light on the mechanisms leading to the initiation of flame oscillation.

The methodology outlined in the subsequent section strongly idealises the interaction of a pressure wave with the flame by assuming the wave and the flame to remain plane for all times. This allows one to properly focus on the intrinsic response of the flame as a result of the perturbed reaction and diffusion processes in the flame layer. The next section gives details on the physical model. Section 2.3 describes the numerical solution method and the results are presented and discussed in section 2.4. Section 2.5 provides the conclusions.

2.2. Statement of the Problem

The basis upon which the following remarks rest is formed by the experiments of KASKAN [58] and YANG *et al.* [108] briefly mentioned in section 1.2. Both experiments have a simple geometry: the flame is propagating freely in a tube with circular cross-section. In KASKAN's experiment, the tube is oriented upright with the close end at the bottom, while in YANG *et al.*'s experiment, the tube is oriented horizontally and has both ends open to the atmosphere. Before conducting the experiment the tube was evacuated to remove any remaining burnt gas from the previous experiment and then filled up with flammable mixture. In YANG *et al.*'s experiment the ends were temporarily shut by a valve until the tube was filled up. After that, the mixture was ignited at one end generating a flame which propagated into the unburnt mixture. For certain mixture compositions the flame begins to show oscillations at the half length of the tube. In private communication,WOOLLEY [107] stressed that the ignition had a strong effect on the subsequent propagation characteristics of the flame. Spark ignition was found to enhance the onset of flame oscillation and thus abandoned in favor of ignition with a pilot flame. In the first phase of the spark ignition process, a strong pressure wave is formed which expands radially from the flame kernel [106]. Although some fraction of the wave energy dissipates during the propagation, the wave reaches the tube ends and may get reflected due to the open ends. The reflected wave could potentially form, by interacting with the flame or other pressure waves, a complex wave pattern in the tube initiating the primary instability characterised by longitudinal flame oscillation. The ignition of the mixture with a pilot flame also generates a pressure wave, yet weaker than in the case of spark ignition. WOOLLEY [107] also mentioned that pressure dampers mounted at both ends of the tube could suppress the flame oscillation entirely. All these observations provide indicators for that pressure waves play an important part in the initiation of flame oscillation. Once the flame was set into oscillatory motion the actual flame properties were found to have negligible influence on the frequency of oscillation. All flames in fuel-rich mixtures with equivalence ratios in the range $[1.1, 1.3]$ were oscillating at the same frequency 227 Hz. It may be speculated that this frequency is fixed by the geometry, *i.e.* the tube length, rather than being an intrinsic property of the flame itself. In fact, KASKAN [58] determined composition limits extending from the fuel-lean to the fuel-rich side for various tube lengths within which the flame oscillated at the same frequency. Two phenomena must be clearly distinguished. First, the actual value of the equivalence ratio determines whether or not the flame oscillates. Second, the frequency and dynamics of an oscillating flame are approximately independent of the equivalence ratio.

In the modelling it is assumed that the flame remains plane for all times. YANG *et al.* [108] observed a sudden transition from a bell-shaped flame to an approximately plane flame at the onset of the secondary instability. KASKAN [58] reported saucer-shaped flames: plane in the centre region with upturned edges. Approximately $80 - 90$ % of the inner tube diameter occupied by the flame remained plane during the cycle. These observations lend some justification for there is a region in the centre, which may be reasonably well approximated with a one-dimensional flame model. A time- and length-scale analysis may be useful to support this argument. For acoustic plane waves the viscous and thermal boundary layer thicknesses are given by

$$\Delta_\mu = \sqrt{\frac{2\mu}{\omega\rho_0}}\,, \quad \text{and} \quad \Delta_\theta = \sqrt{\frac{2q_\theta}{\omega\rho_0 c_p}}\,, \tag{2.2}$$

respectively, where ω, μ, q_θ, and c_p are the angular frequency of oscillation ($\omega = 2\pi f$), dynamic viscosity, thermal conductivity, and heat capacity of the mixture at constant pressure. ρ_0 is the density of the mixture on the unburnt side. Using the experimentally determined frequency of oscillation, f, together with estimates for the material coefficients at the flame yields $\Delta_\mu \approx 0.7$ mm and $\Delta_\theta \approx 0.8$ mm for the thicknesses. The inner tube diameter, D_t, is 20 mm in both experiments. Hence, viscous and thermal effects originating from the presence of the tube wall are confined to a narrow layer near the boundary and unlikely to exert significant influence on the flame in the centre region. The time scales associated with the heat transfer through conduction across and along the flame layer may be roughly estimated with

$$\Delta_T^{\mathrm{lon}} \approx \frac{\mathrm{d}^2 \rho c_p}{\kappa} \ , \quad \text{and} \quad \Delta_T^{\mathrm{lat}} \approx \frac{\frac{1}{4}\mathrm{D}_t^2 \rho c_p}{\kappa} \ , \tag{2.3}$$

where d is the thickness of the primary reaction zone, which is $\mathrm{d} \approx 1$ mm. Hence, $f\Delta_T^{\mathrm{lon}} \approx 1$, and $\Delta_T^{\mathrm{lat}} \gg \Delta_T^{\mathrm{lon}}$. This implies that heat transfer in the lateral direction proceeds on a time scale too slow to affect significantly the flame response in the centre region during the flame oscillation, and may thus be neglected. The binary diffusion coefficients are of the same order as the thermal diffusivity, $q_\theta/(\rho c_p)$, implying that the effects of mechanical diffusion along the flame layer are of secondary importance, and may thus also be neglected. It must be stressed, however, that the LEWIS numbers are not assumed unity or equal for all constituents in the modelling strategy outlined below.

The field equations (1.4)-(1.6), *cf.* section 1.4, are solved numerically by employing a high-order accurate Discontinuous GALERKIN (DG) method. The numerical studies are conducted in the following way. First the flame is brought into a state of steady propagation, and then subjected to a single pressure wave to study whether or not the flame noticeably departs from the state of steady propagation. The time scale associated with the pressure wave was chosen to be of the same order as the time scales on which chemical reactions in the primary reaction zone typically proceed, namely 10^{-4} s. ZAMBON AND CHELLIAH [110] have demonstrated in a counterflow-flame arrangement that a noticeable flame response to pressure waves requires both time scales to be of the same order.

2.3. Numerical Solution

Transformation

For the purpose of determining the state of steady flame propagation the balance equations (1.4)-(1.6) are transformed by seeking for solutions of the form

$$\left.\begin{aligned} \rho_{\mathfrak{a}} &= \Lambda_{\mathfrak{a}}\left(x - v t, t\right) \ , \\ v &= \mathrm{v}\left(x - v t, t\right) \ , \\ \theta &= \Theta\left(x - v t, t\right) \ , \\ \widehat{c}_{\mathfrak{a}} &= \widehat{\mathrm{c}}_{\mathfrak{a}}\left(x - v t, t\right) \ , \\ J_{\mathfrak{a}} &= \mathrm{J}_{\mathfrak{a}}\left(x - v t, t\right) \ , \\ T &= \mathrm{T}\left(x - v t, t\right) \ , \\ \epsilon &= \Xi\left(x - v t, t\right) \ , \\ q &= \mathrm{q}\left(x - v t, t\right) \ , \end{aligned}\right\} \tag{2.4}$$

where the fixed real number v denotes the flame speed. The above transformation (2.4) has been applied by DUNN AND FOSDICK [35] in the study of steady, structured shock waves in thermoelastic materials. Note that the tensor fields in (1.4)-(1.6) are already reduced to scalar fields in (2.4). Upon inserting (2.4) into (1.4)-(1.6) and computing the derivatives one obtains the following differential equation system

$$\frac{\partial \rho_{\mathfrak{a}}}{\partial t} + \frac{\partial}{\partial \xi}\left[\rho_{\mathfrak{a}}\left(v - v\right) + J_{\mathfrak{a}}\right] = \widehat{c}_{\mathfrak{a}} \ , \qquad (\mathfrak{a} = 1, 2, \ldots, \mathfrak{N}) \tag{2.5}$$

$$\frac{\partial \rho v}{\partial t} + \frac{\partial}{\partial \xi}\left[\rho v\left(v - v\right) - T\right] = 0 \ , \tag{2.6}$$

$$\frac{\partial \rho \epsilon}{\partial t} + \frac{\partial}{\partial \xi}\left[\rho \epsilon\left(v - v\right) + q\right] = T\frac{\partial v}{\partial \xi} \ , \tag{2.7}$$

where $\xi = x - vt$ is the characteristic variable. When dropping the explicit dependence of the response functions $(\Lambda_{\mathfrak{a}}, \mathrm{v}, \Theta, \widehat{\mathrm{c}}_{\mathfrak{a}}, \mathrm{J}_{\mathfrak{a}}, \mathrm{T}, \Xi, \mathrm{q})$ on time, and assuming that the mixture occupies the entire line $(-\infty, +\infty)$, one can derive the *Rankine-Hugoniot* conditions by integrating between the unburnt side, $\xi = -\infty$, and the burnt side, $\xi = +\infty$. The flame speed is evaluated by means of the integral

$$v = \frac{1}{\rho^{-}\left(c_f^{-} - c_f^{+}\right)} \int_{\xi=-\infty}^{\xi=+\infty} \widehat{c}_f \ d\xi \ , \tag{2.8}$$

in which the subscript f refers to the fuel and $\rho^{-} \equiv \sum_{\mathfrak{a}=1}^{\mathfrak{N}} \Lambda_{\mathfrak{a}}(-\infty, t)$, $c_f^{-} \equiv \ \mathrm{c}_f(-\infty, t)$, and $c_f^{+} \equiv \ \mathrm{c}_f(+\infty, t)$. This approach does not fix the flame position in the moving frame explicitly, but ensures that the flame is not propagating out of the computational domain for the time periods investigated here. The above differential equations (2.5)-(2.7) are supplemented by the constitutive functionals for a linear theory of simple mixtures of fluids, see section 1.4. These functionals are

chemical source terms — 4-step reaction mechanism of JONES AND LINDSTEDT [53] , (2.9)

diffusion model
$$\rho_{\mathfrak{a}} u_{\mathfrak{a}} = -\rho m_{\mathfrak{a}} \frac{\partial c_{\mathfrak{a}}}{\partial \xi} \ , \tag{2.10}$$

stress tensor
$$T = -\pi + 2\mu \frac{\partial v}{\partial \xi} \ , \tag{2.11}$$

specific energy
$$\epsilon = \sum_{\mathfrak{a}=1}^{\mathfrak{N}} \left(c_{\mathfrak{a}} h_{\mathfrak{a}}\right) - \frac{\pi}{\rho} \ , \tag{2.12}$$

heat flux
$$q = -q_\theta \frac{\partial \theta}{\partial \xi} \ , \tag{2.13}$$

where the specific free enthalpies $h_{\mathfrak{a}}$ are computed using the polynomial data base [69]. The partial pressures, $\pi_{\mathfrak{a}}$, are given by the equation of state for ideal gases. Both the dynamic viscosity, μ, and thermal conductivity, q_θ of the mixture are evaluated as the mass-fraction weighted sum of the material coefficients of the individual constituents. The viscosities of the individual constituents are computed using the CHAPMAN-ENSKOG method, while the thermal conductivities are calculated by means of the modified EUCKEN model [79]. The modified EUCKEN model tends to be more accurate than the standard

Chapman-Enskog method with Lennard-Jones potentials. The diffusion coefficient of the $\mathfrak{a}$th constituent into the mixture, $m_{\mathfrak{a}}$, is computed by

$$m_{\mathfrak{a}} = \frac{1 - c_{\mathfrak{a}}}{\sum_{\mathfrak{b}\neq\mathfrak{a}}^{\mathfrak{N}} \frac{x_{\mathfrak{a}}}{m_{\mathfrak{a}\mathfrak{b}}}} \ . \tag{2.14}$$

$x_{\mathfrak{a}}$ and $m_{\mathfrak{a}\mathfrak{b}}$ in (2.14) represent the mole fraction of the $\mathfrak{a}$th constituent and the binary diffusion coefficients, respectively. The binary diffusion coefficients are also calculated with the Chapman-Enskog method.

Discontinuous Galerkin Method

The Discontinuous Galerkin (DG) method employed here is in parts based on the numerical framework proposed by Lv and Ihme [65]. Differences between the present scheme and Lv and Ihme's numerical framework are noted in passing. The reader may also consult [48] and [57] for an introduction on the subject. DG methods are highly accurate, exhibit spectral convergence rates for smooth solutions, *hp*-adaptivity, and numerical stability for wave dominated problems due to the weak coupling at the element nodes. Because of these properties DG methods are preferably used to simulate acoustic problems. To begin with, the differential equation system (2.5)-(2.7) together with the constitutive functionals (2.9)-(2.13) are recast into the form

$$\frac{\partial \mathbf{U}}{\partial t} + \frac{\partial \mathbf{F}}{\partial \xi} = \frac{\partial \mathbf{D}}{\partial \xi} + \mathbf{S} \ , \tag{2.15}$$

where $\mathbf{U}$, $\mathbf{F}$, $\mathbf{D}$ and $\mathbf{S}$ represent the set of balanced variables, convective and diffusive fluxes, and supply terms, respectively. The computational domain is discretised by K non-overlapping discrete elements D^k, where $\mathsf{D}^k = [\xi_l^k, \xi_r^k]$. In each discrete element the approximate solution is expressed as

$$\xi \in \mathsf{D}^k : \quad \mathbf{U}_h^k(\xi, t) = \sum_{i=1}^{N_p} \breve{\mathbf{U}}_i^k(t) \psi_i^k(\xi) \ , \tag{2.16}$$

in which N_p, $\breve{\mathbf{U}}_i^k$ and ψ_i^k represent the number of grid points in D^k, the nodal values of the approximate solution $\mathbf{U}_h$, and the basis functions, respectively. The order of the basis functions, $N = N_p - 1$, may vary from element to element. By requiring that the local residual of the approximate solution be orthogonal to all test functions, ϕ_j^k, of the space of test functions, V_h, one can construct a numerical scheme to solve (2.15). Multiplying the numerical approximation of (2.15) with ϕ_j^k and integrating over D^k yields

$$\int_{\mathsf{D}^k} \left(\frac{\partial \mathbf{U}_h^k}{\partial t} + \frac{\partial \mathbf{F}_h^k}{\partial \xi} - \frac{\partial \mathbf{D}_h^k}{\partial \xi} - \mathbf{S}_h^k \right) \phi_j^k(\xi) \ d\xi = 0 \ , \forall \phi_j^k \in \mathsf{V}_h \ , \tag{2.17}$$

where $j = 1, 2, \ldots, N_p$ and $k = 1, 2, \ldots, K$. The Galerkin method is obtained when the test functions are chosen to be the same as the basis functions, such that $\phi_j^k(\xi) = \psi_j^k(\xi)$. Equation (2.17) is yet a strictly local statement from which one cannot obtain the global solution. This can be circumvented by integrating (2.17) by parts. In the present work, the *strong form* is used, which is recovered by integrating (2.17) by parts twice. This

results in

$$\int_{\mathsf{D}^k} \left(\frac{\partial \mathbf{U}_h^k}{\partial t} + \frac{\partial \mathbf{F}_h^k}{\partial \xi} - \frac{\partial \mathbf{D}_h^k}{\partial \xi} - \mathbf{S}_h^k \right) \psi_j^k \; d\xi = \left[\left(\mathbf{F}_h^k - \mathbf{F}^* - \mathbf{D}_h^k + \mathbf{D}^* \right) \psi_j^k \right] \Big|_{\xi^k}^{\xi^{k+1}} \; . \tag{2.18}$$

Quantities with an asterisk denote the numerical fluxes, which couple the elements with each other and also serve to impose the boundary conditions. Then, the global solution may be defined as the direct sum of the approximate solutions on the element level

$$\mathbf{U}_h(\xi, t) \equiv \bigoplus_{k=1}^{K} \mathbf{U}_h^k(\xi, t) \tag{2.19}$$

The numerical fluxes must be chosen appropriately to ensure uniqueness of the solution. When (2.16) is inserted into (2.18) the final semi-discrete scheme is obtained. Using Einstein's notation the semi-discrete form may be written as

$$\left. \begin{aligned} [\mathsf{M}_{ij}]^k \frac{d}{dt} [\breve{\mathbf{U}}_j]_h^k = & - [\mathsf{S}_{ij}]^k \left([\breve{\mathbf{F}}_j]_h^k - [\breve{\mathbf{D}}_j]_h^k \right) + [\mathsf{M}_{ij}]^k \, [\breve{\mathbf{S}}_j]_h^k \\ & + \left(\mathbf{F}_h^k - \mathbf{F}^* - \mathbf{D}_h^k + \mathbf{D}^* \right) \Big|^{\xi^{k+1}} \psi_j^k(\xi^{k+1}) \\ & - \left(\mathbf{F}_h^k - \mathbf{F}^* - \mathbf{D}_h^k + \mathbf{D}^* \right) \Big|^{\xi^k} \psi_j^k(\xi^k) \; . \end{aligned} \right\} \tag{2.20}$$

The entries of the matrices $[\mathsf{M}_{ij}]^k$ and $[\mathsf{S}_{ij}]^k$ in (2.20) are given by

$$\mathsf{M}_{ij}^k = \int_{\mathsf{D}^k} \psi_i^k(\xi) \psi_j^k(\xi) \; d\xi \; , \qquad \mathsf{S}_{ij}^k = \int_{\mathsf{D}^k} \psi_i^k(\xi) \frac{d\psi_j^k(\xi)}{d\xi} \; d\xi \tag{2.21}$$

The former matrix is usually referred to as *element mass-matrix*, while the latter is called *element stiffness-matrix*. In comparison to standard Finite-Element Methods with a globally defined mass- and stiffness-matrix the element mass-matrix in DG methods can be inverted at comparatively little cost. Lv and Ihme have employed the *weak form* of (2.17), which is obtained by integrating (2.17) by parts once. The weak form is preferably used in combination with orthogonal Legendre polynomials, while in the present study interpolating Lagrange polynomials are employed. To avoid ill-conditioning of $[\mathsf{M}_{ij}]^k$ when increasing the polynomial order, N, the Legendre-Gauss-Lobatto quadrature points are used to evaluate the integrals in (2.21). The convective part of the numerical flux $\mathbf{F}^*$ is computed with the Harten-Lax-van Leer approximate Riemann solver, see [94]. Note that the minimum and maximum eigenvalues of the Jacobian of $\mathbf{F}$ are here $v - v - s$ and $v - v + s$, respectively, where s denotes the speed of sound. A central flux with an additional term to penalise the jump at the connecting nodes of adjacent elements is employed to compute the diffusive part of the numerical flux $\mathbf{D}^*$. In the practical application, a penalty parameter with a value of 10 was found to yield stable solutions. Lv and Ihme use the more sophisticated method of Bassi and Rebay [8], but this is not needed here.

Time scale disparities in the reaction mechanism often lead to stiff equations for the chemical source terms requiring specific numerical integration schemes which are different from those needed to integrate the convective and diffusive fluxes. So as to separate the numerically stiff source terms from the convective and diffusive fluxes in the time integration of (2.20) the Strang splitting scheme is used, which may be written as

1.) $[\breve{\mathbf{U}}_j]_h^k(t^n) \rightarrow [\widetilde{\mathbf{U}}_j]_k^{n+\frac{1}{2}}$, $t \in \left(t^n, t^n + \frac{1}{2}\Delta_t\right]$,

$$\frac{d}{dt}[\breve{\mathbf{U}}_j]_h^k = [\mathcal{F}_j]_h^k + [\mathcal{D}_j]_h^k \,, \tag{2.22}$$

2.) $[\breve{\mathbf{U}}_j]_h^k(t^n) = [\widetilde{\mathbf{U}}_j]_k^{n+\frac{1}{2}} \rightarrow [\breve{\mathbf{U}}_j]_h^k(t^{n+\frac{1}{2}})$, $t \in (t^n, t^n + \Delta_t]$,

$$\frac{d}{dt}[\breve{\mathbf{U}}_j]_h^k = [\mathcal{S}_j]_h^k \,, \tag{2.23}$$

3.) $[\breve{\mathbf{U}}_j]_h^k(t^{n+\frac{1}{2}}) \rightarrow [\breve{\mathbf{U}}_j]_h^k(t^{n+1})$, $t \in \left(t^n + \frac{1}{2}\Delta_t, t^n + \Delta_t\right]$,

$$\frac{d}{dt}[\breve{\mathbf{U}}_j]_h^k = [\mathcal{F}_j]_h^k + [\mathcal{D}_j]_h^k \,, \tag{2.24}$$

where $[\mathcal{F}_j]_h^k$, $[\mathcal{D}_j]_h^k$, and $[\mathcal{S}_j]_h^k$ denote symbolically the spatial discretisation of the convective, and diffusive fluxes, and the source terms, respectively. The quantity Δ_t in (2.22)-(2.24) represents the numerical time step. The Strang splitting scheme is second-order accurate. As a result of the splitting scheme ODE systems for the chemical source terms are obtained, which are here integrated with the fifth-order accurate implicit Runge-Kutta method Radau5 of Hairer and Wanner [46]. For the Radau5 integration the absolute and relative tolerance were set to 10^{-10} and 10^{-8}, respectively. One major advantage of such splitting schemes is that the obtained ODE systems for the chemical source terms can be solved for each node independently, which offers potential for parallelisation. The convective and diffusive fluxes, on the other hand, are integrated in time using the optimal three-step third-order accurate stability-preserving explicit Runge-Kutta scheme, which is

$$\left.\begin{aligned}
[\widetilde{\mathbf{U}}_j]_k^1 &= [\breve{\mathbf{U}}_j]_h^k(t^n) + \Delta_t \left\{[\mathcal{F}_j]_k^n + [\mathcal{D}_j]_k^n\right\} \\
[\widetilde{\mathbf{U}}_j]_k^2 &= \frac{1}{4}\left\{3[\breve{\mathbf{U}}_j]_h^k(t^n) + [\widetilde{\mathbf{U}}_j]_k^1 + \Delta_t\left([\mathcal{F}_j]_k^1 + [\mathcal{D}_j]_k^1\right)\right\} \\
[\widetilde{\mathbf{U}}_j]_k^3 &= [\breve{\mathbf{U}}_j]_h^k(t^{n+1}) = \frac{1}{3}\left\{[\breve{\mathbf{U}}_j]_h^k(t^n) + 2[\widetilde{\mathbf{U}}_j]_k^2 + 2\Delta_t\left([\mathcal{F}_j]_k^2 + [\mathcal{D}_j]_k^2\right)\right\}
\end{aligned}\right\} \tag{2.25}$$

Following Lv and Ihme a different form of the energy balance of the mixture (1.6) (*c.f.* section 1.4) is discretised. This is necessary since the specific heat capacity of the mixture is a function of the partial densities and temperature. It was demonstrated by Abgrall and Karni [1] that differences in the specific heat capacity ratio across the interface of adjacent elements may induce spurious oscillations of the pressure when employing strictly conservative spatial discretisation schemes. As was shown by Lv and Ihme, this undesired phenomenon can be circumvented by first rewriting the energy balance upon introducing an effective heat capacity ratio, which is yet to be defined. Using the present notation, the definition proposed by Lv and Ihme is

$$\gamma^\diamond \equiv \sum_{\mathfrak{a}=1}^{\mathfrak{N}} c_\mathfrak{a}\left(\frac{c_{p,\mathfrak{a}}^\diamond}{c_{p,\mathfrak{a}}^\diamond - \frac{R}{M_\mathfrak{a}}}\right) \text{ , where } \qquad c_{p,\mathfrak{a}}^\diamond = \frac{1}{\theta - \theta_0}\int_{\widetilde{\theta}=\theta_0}^{\widetilde{\theta}=\theta} c_{p,\mathfrak{a}}(\widetilde{\theta})d\widetilde{\theta} \,. \tag{2.26}$$

Such a definition of $\gamma^\diamond$ appears only meaningful if the reference temperature, θ_0, is chosen to lie outside the temperature range expected in the investigated flow configuration. In this way singularities in $\gamma^\diamond$ are avoided. Lv and Ihme chose $\theta_0 = 0$ K, which also

necessitates an evaluation of the enthalpies of formation, $\Delta h^0_{\mathfrak{a}}$, at 0 K. These are usually given with respect to the reference state $\theta_0 = 298.15$ K, but the shift to 0 K can be incorporated by using the data base [69]. With $\gamma^\diamond$, the energy balance becomes

$$\frac{\partial \rho e}{\partial t} + \frac{\partial}{\partial \xi}\left[\rho e\,(v - v) + q\right] = T\frac{\partial v}{\partial \xi} + \sum_{\mathfrak{a}=1}^{\mathfrak{N}} \left(\widehat{c}_{\mathfrak{a}} \Delta h^0_{\mathfrak{a}}\right) \ , \tag{2.27}$$

where e is given by

$$e = \frac{1}{\gamma^\diamond - 1}\frac{\pi}{\rho} \ . \tag{2.28}$$

Equation (2.28) has the same form as the energy of a compressible EULER fluid for which many reliable DG methods have been developed in the past, *cf.* [57] and [48]. The heat release rate, $Q \equiv \sum_{\mathfrak{a}=1}^{\mathfrak{N}} (\widehat{c}_{\mathfrak{a}} \Delta h^0_{\mathfrak{a}})$, on the right-hand side of (2.27) is also integrated with Radau5 using the above-stated tolerance values. In the DG discretisation of LV AND IHME the function $\gamma^\diamond$ is assumed homogeneous in each element D^k and computed from the mean of the mass fractions and temperature. The value of $\gamma^\diamond$ varies from element to element. During the time stepping $\gamma^\diamond$ is held constant, and updated only at the end of each time step using the computed solution at the new time level. In this way, an energy conservation error is introduced, which is proportional to the difference of $\gamma^\diamond$ between adjacent elements. However, artificial oscillations in the pressure field are reduced to a minimum with this approach. The conservation error can be maintained stable by using polynomials which are second order or above. LV AND IHME also reconstruct the value of e at the connecting element nodes using $\gamma^\diamond$ of both elements, but this made no discernible difference in the computed results and was thus omitted.

Strong pressure and velocity waves were encountered in the initial transition period after ignition of the mixture. This led to stability problems of the simulations and required limiting of the computed solution. The hierarchical slope-limiter of BISWAS *et al.* [12] was used here, and applied to the balanced variables $\mathbf{U}_h$ in a post-processing manner in each RUNGE-KUTTA sub-step. This limiter, although detecting element solutions which are non-smooth, leads to excessive numerical induced diffusion. Hence, the limiter was only used in the critical transition period and then 'switched off'. Better accuracy with limiting can be achieved by applying the limiter to the characteristic variables obtainable by transforming the balanced variables with the left eigenvector of the JACOBIAN of the convective fluxes. After limiting the characteristic variables, the transformation back to the balanced variables by means of the right eigenvector of the JACOBIAN of the convective fluxes must be performed. Still another way to improve the accuracy in the limiting procedure is to combine the forward- and backward transformation with a WENO-based limiter, such as proposed by ZHONG AND SHU [111]. Such a sophisticated limiting was not needed here, since the computed fields remain smooth beyond the critical transition period. The time step was computed using the CFL criterion of HESTHAVEN AND WARBURTON [48], namely

$$\Delta_t = \frac{0.5\Delta_\xi}{N^2\left(|v - v| + s + \frac{N^2\zeta}{\Delta_\xi}\right)} \ , \tag{2.29}$$

where $\Delta_\xi = \xi^k_r - \xi^k_l$ is the element size. A high-order discretisation scheme for the field equations of Rational Thermodynamics (*c.f.* appendix A.1) is presented in A.2.

Initial and Boundary Conditions

The balanced variables $\mathbf{U}$ are initialised as follows. The flame is positioned in the middle of the computational domain. Shape functions in the form of the hyperbolic tangent are used to smoothly transition the mass fractions and temperature from the unburnt to the burnt side. The composition of the mixture in strong equilibrium is obtained by minimising the GIBBS free energy at an estimated value of the temperature in strong equilibrium and standard pressure. On the unburnt side the mixture composition is evaluated using the given equivalence ratio. The initial pressure is set to standard pressure everywhere in the domain, while the initial velocity field is set to zero in the whole domain.

To reduce artificial wave reflections at the boundaries of the computational domain to a minimum, the non-reflecting outflow boundary conditions of YOO AND IM [109] are imposed. In the present notation, these may be expressed as

$$\frac{\partial v}{\partial t} + \frac{\mathrm{L}_3 - \mathrm{L}_1}{\rho s} = 0 \ , \tag{2.30}$$

$$\frac{\partial \rho}{\partial t} + \mathrm{L}_2 + \frac{\mathrm{L}_3 + \mathrm{L}_1}{s^2} \ , \tag{2.31}$$

$$\frac{\partial \pi}{\partial t} + \mathrm{L}_1 + \mathrm{L}_3 = 0 \ , \tag{2.32}$$

$$\frac{\partial c_{\mathfrak{a}}}{\partial t} + \mathrm{L}_{\mathfrak{a}} = 0 \ . \tag{2.33}$$

The variables L_1–L_3, and $\mathrm{L}_{\mathfrak{a}}$ ($\mathfrak{a} = 1, 2, \ldots, \mathfrak{N}$) in (2.30)-(2.33) represent the amplitudes of the characteristic waves, and are given by

$$\mathrm{L}_1 = \frac{(v - v - s)}{2} \left(\frac{\partial \pi}{\partial \xi} - \rho s \frac{\partial v}{\partial \xi} \right) \ , \tag{2.34}$$

$$\mathrm{L}_2 = (v - v) \left(\frac{\partial \rho}{\partial \xi} - \frac{1}{s^2} \frac{\partial \pi}{\partial \xi} \right) \ , \tag{2.35}$$

$$\mathrm{L}_3 = \frac{(v - v + s)}{2} \left(\frac{\partial \pi}{\partial \xi} + \rho s \frac{\partial v}{\partial \xi} \right) \ , \tag{2.36}$$

$$\mathrm{L}_{\mathfrak{a}} = (v - v) \frac{\partial c_{\mathfrak{a}}}{\partial \xi} \ . \tag{2.37}$$

The incoming characteristic waves require additional physical information from the environment external to the computational domain. YOO AND IM use the conditions listed in Table 2.1, which are based on the work of RUDY AND STRIKWERDA [83, 84]. The boundary differential equations are integrated synchronously with the RUNGE-KUTTA scheme for the interior nodes. When the flame has approached the state of steady propagation, a pressure wave with *beta*-PDF shape is superimposed onto the pressure computed with the non-reflecting conditions at the boundary on the unburnt side of the flame. The *beta*-PDF shape was chosen to mimic the asymmetry of the transmitted pressure wave originating from the ignition event [66], and has the following parameters $\alpha = 0.2$ and $\beta = 5.0$. At the same time v is fixed at the converged value to study the spatial oscillations of the flame when the observer frame is moving at the mean flame speed.

Table 2.1.: Wave amplitudes of the characteristic waves. π_∞ is the target pressure and $\beta \equiv \sigma s[1-(v/s)^2]/(2l_\xi)$ the pressure relaxation coefficient, where σ represents the relaxation factor. σ was set to 0.25. Source [109].

Outflow at the left boundary		Outflow at the right boundary	
Wave speed	*Wave amplitude*	*Wave speed*	*Wave amplitude*
$v - v - s < 0$	L_1 computed	$v - v - s < 0$	$L_1 = \beta(\pi - \pi_\infty)$
$v - v < 0$	L_2 computed	$v - v > 0$	L_2 computed
$v - v + s > 0$	$L_3 = \beta(\pi - \pi_\infty)$	$v - v + s > 0$	L_3 computed
$v - v < 0$	L_4 computed	$v - v > 0$	L_4 computed

Computational Domain

The computational domain has a length of 20 cm, which equals approximately 100 d upstream and downstream of the flame position. The computational domain is discretised with $1,400$ quadratic elements which are clustered towards the middle of the domain.

2.4. Results and Discussion

A few remarks upon general observations in connection with the just outlined numerical scheme shall be put first. The stability requirements on the numerical time step lead to time steps of the order of 10^{-9} s. Such small time steps are prohibitive for investigating the long-term behaviour following the initial impact of the pressure wave. The current investigations are limited to the moment the wave is in contact with the flame and a time period of a few milliseconds beyond. It may be more practical in future investigations to fix *a priori* the range of physical time scales to be resolved within the simulation and achieve numerical stability by employing an implicit time integration scheme. In this way the time step is not strictly tied to the maximum eigenvalue of the JACOBIAN of the convective fluxes, and can be increased. An implicit scheme is likely to increase the cost per time step, but fewer time steps are required to resolve a given time interval, which reduces the total computing time. The flame speed converged after a time period of 10 ms. To attain the state of steady flame propagation takes approximately two weeks of computing time on a single core of a 2.5 GHz Quad core Intel Xeon processor.

A typical steady flame structure obtained by means of the DG method is shown in Figure 2.1 together with corresponding experimental data. All the predicted major species mole fractions are in good agreement with the experimental data, except for H_2, which is slightly overpredicted in the secondary reaction zone. The predicted mass flux through the flame is shown in Figure 2.1 (c). The mass flux is expected to remain uniform across the flame, but the numerical simulation predicts a small variation. This implies numerical errors in the mass conservation. The cause for this mass conservation error could not be identified, but may be connected with the order of the polynomial approximation. A third-order approximation is more accurate than the second-order approximation for the same number of grid nodes. The pressure profile across the flame presented in Figure 2.1 (d) shows the typical pressure drop due to the fluid acceleration across the flame layer. It can also be concluded that the special treatment of the energy balance, *cf.* (2.27), does not suppress the artificial pressure fluctuations across the flame entirely.

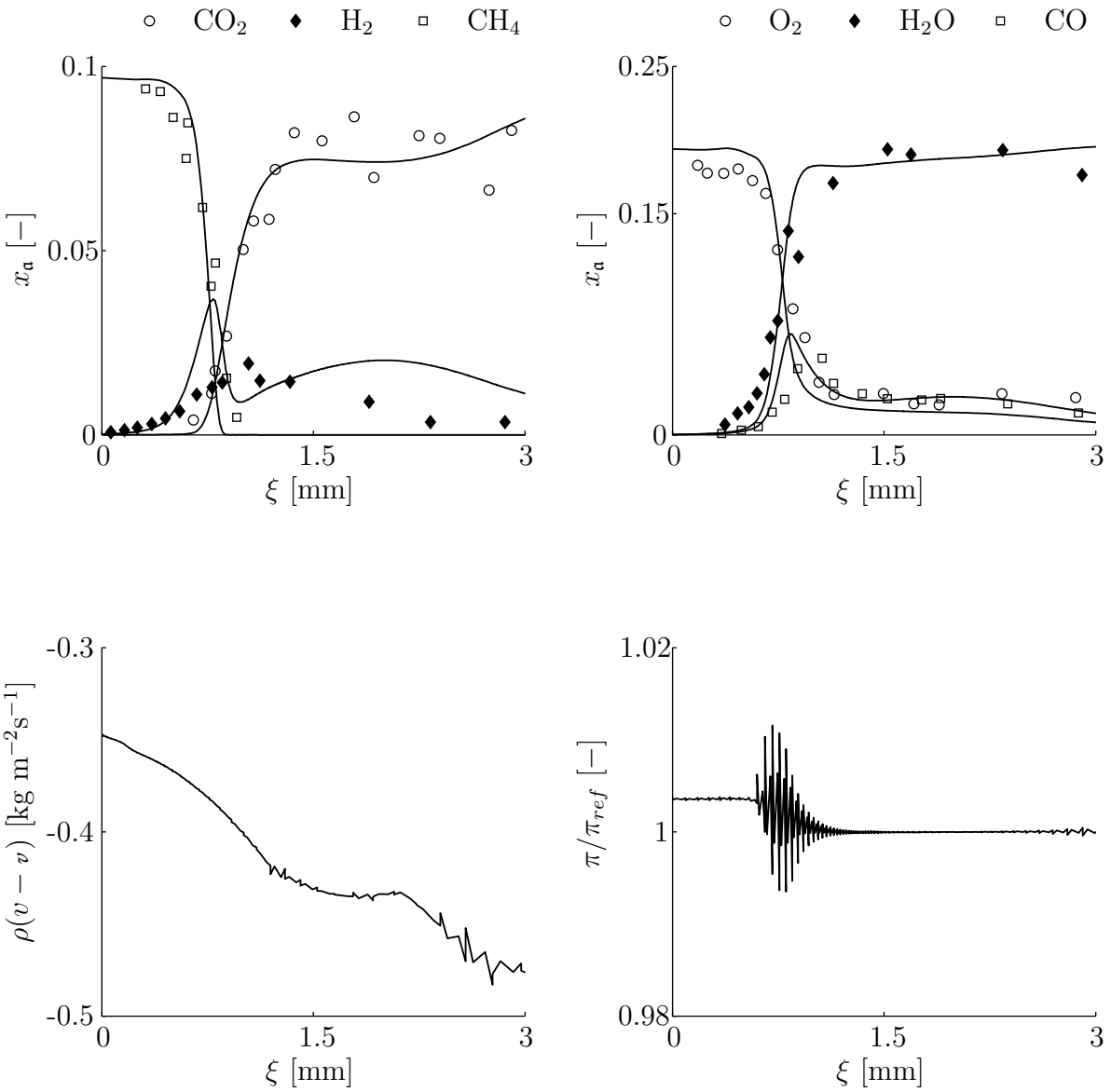

Figure 2.1.: Structure of a stoichiometric methane-air flame computed with the DG method using quadratic elements. Symbols represent the experimental data of Bechtel *et al.* [10]. π_{ref} has a value of $1.01 \cdot 10^5$ Pa.

Figure 2.2 (a) compares the computed flame speed of the above-discussed stoichiometric methane-air flame with the measurements. The predicted flame speed is overestimated with respect to the measurements by approximately 15 %. Similarly, the computed flame speeds for other compositions are also overpredicted. At present, it is not entirely clear why the computed flame speeds differ in such amounts from the measurements, since the global four-step reaction mechanism of Jones and Lindstedt [53] is known to reproduce the flame speeds with good accuracy. However, Jones and Lindstedt computed the steady flame structure by treating the fluid as incompressible, and using second-order spatial discretisation schemes. Lv and Ihme [65] employed a DG method for compressible fluids to simulate plane flames in hydrogen-oxygen mixtures diluted with argon and ob-

tained flame speeds which lie above those predicted with a flow solver for incompressible fluids. Lv and Ihme attribute these discrepancies to the low Mach number approximation. In the present simulations, another source of uncertainty comes from the mass conservation error observed in Figure 2.1 (d).

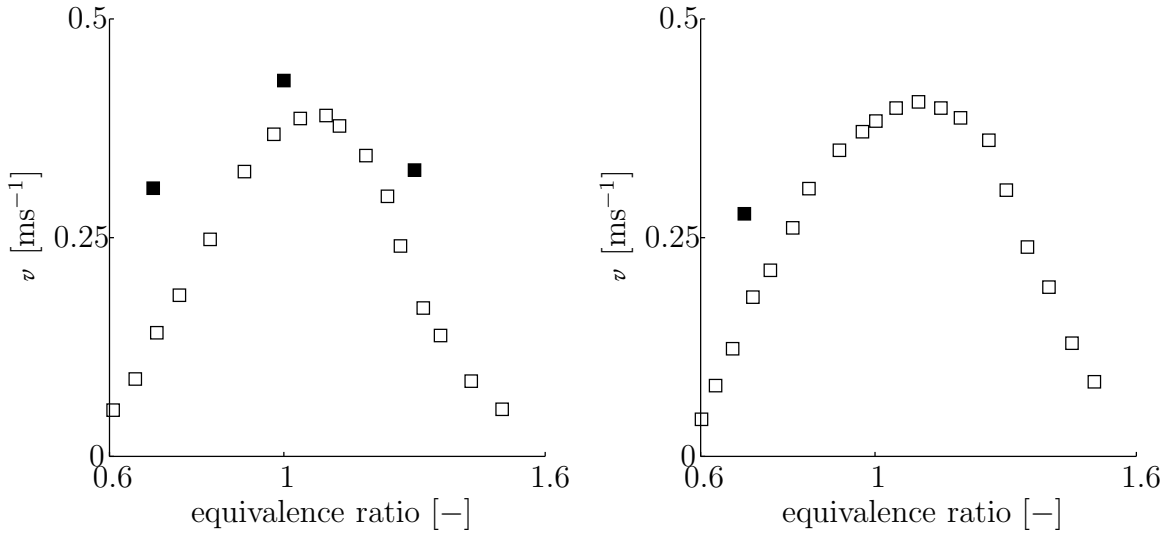

(a) CH_4-air, $\theta^- = 300$ K, $\pi = 1$ bar

(b) C_3H_8-air, $\theta^- = 300$ K, $\pi = 1$ bar

Figure 2.2.: Experimentally determined (open symbols) and predicted (closed symbols) flame speeds.

In the following, the discussion focuses on the analysis of the pressure wave-flame interaction. The computed steady flame structures, such as the one shown exemplarily in Figure 2.1, are perturbed by a single pressure wave in the shape of a *beta*-PDF. Three flame simulations are presented in the following, which differ in the initial mixture composition. A fuel-lean and fuel-rich methane-air mixture, as well as a fuel-lean propane-air mixture are considered. The equivalence ratio for each of the simulations is adjusted to give rise to the same flame speed of 25 cm/s, which allows for comparison amongst the different fuels. This value of the flame speed lies at the upper end of flame speeds known from Searby [86]'s experiment to produce the primary instability (longitudinal flame oscillation). Figure 2.3 shows the pressure and velocity field in the vicinity of the fuel-lean methane-air flame upon impact of the pressure wave. The grey-shaded area indicates the length of the primary reaction zone evaluated from the steady state solution. Some minor artificial oscillations of the pressure field exist inside the primary reaction zone, which are not entirely suppressed by the energy-relaxation methodology employed here.

The obtained results show a partial reflection of the incident pressure wave at the flame, while the remaining wave energy is transmitted through the flame. As a result of the fluid acceleration across the flame layer, the amplitude of the transmitted wave is 44 % lower than that of the incident wave, while the reflected pressure wave has an amplitude of 34 % of the incident wave. Due to the higher speed of sound on the burnt side the transmitted pressure wave propagates faster than the reflected wave. It can also be seen that the transmitted wave has a larger wave length than the incident wave. The velocity field, on the other hand, shows an increase of the wave strength when the wave travels across the flame layer. This time the amplitude of the transmitted wave is approximately

44 % higher than that of the incident wave. At the same time, some fraction of the wave energy is reflected at the flame. The decrease in the pressure amplitude is approximately the same as the increase of the flame speed, *cf.* Figure 2.5. The fact that the flame speed increases upon impact of the pressure wave suggests an intrinsic response of the flame through perturbation of the chemical source terms, which is expected on wave lengths that are of the same order as the length of the primary reaction zone, *cf.* Figure 2.5. However, the impulse appears too short to significantly displace the flame from its current position, *cf.* Figure 2.4 (d). The flame position, ξ_f, deviates much slower over time from its converged value than the flame speed. The flame appears to be shifted faster downstream when the pressure wave is in contact with the flame. This may be simply due to the pressure force exerted on the flame. Note that the frame velocity associated with the moving observer is fixed in time. A larger time period must be resolved to identify low frequency components in the movement of the flame. For comparison, one cycle at the experimentally determined frequency of oscillation takes 4.4 ms to complete, while the simulations resolve a time period of 3 ms owing to the large computational demand.

The history of the global maximum temperature in Figure 2.4 (c) shows a peak at around the same time the flame speed is at its maximum. Other spikes in the time history of the global maximum pressure and velocity beyond the initial contact between the wave and the flame originate from undesired oscillations when the transmitted wave reaches the right end of the domain. It is interesting to observe that the pressure amplitude decreases noticeably between the moment of the wave imposition at the inlet boundary and the contact with the flame. This implies a pronounced dissipative mechanism which is likely connected with the imposed wave shape, *i.e.* large gradients in the velocity wave enhance the working of the viscous forces. The results for the fuel-lean methane-air flame suggest that the incident pressure wave is partially reflected at the flame, while the associated velocity wave is amplified when travelling across the flame layer. In this way, the initial pressure wave originating from the ignition phase may develop into a complex wave pattern covering a range of wave lengths, and amplitudes. The reflected and transmitted pressure waves may not only be reflected at the boundaries of the tube and the flame, but may also interact with each other. Moreover, the waves propagate at different speeds due to the variation of the fluid properties across the flame layer. This can create strong pressure fluctuations on the unburnt side which the flame has to traverse when propagating towards the open end of the tube. Yang *et al.* [108] have already speculated upon such a mechanism.

The resolved time period does not provide evidence for a sustained spatial oscillation of the flame when being excited on the time scale of the chemical reactions in the primary reaction zone. However, the results indicate that two time scales should be properly distinguished. The global maxima for temperature, velocity, and flame speed respond all at the time scale associated with the imposed pressure wave, while changes in the flame position proceed on a larger time scale.

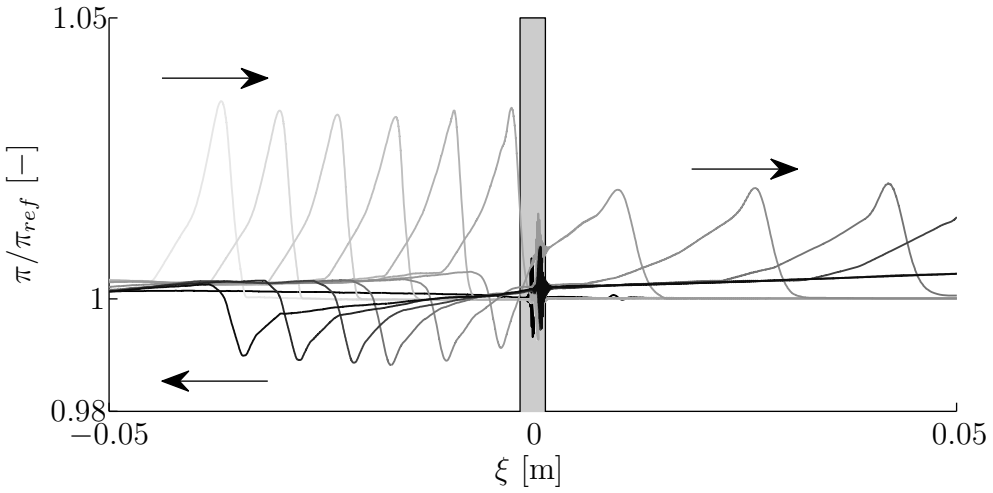

(a)

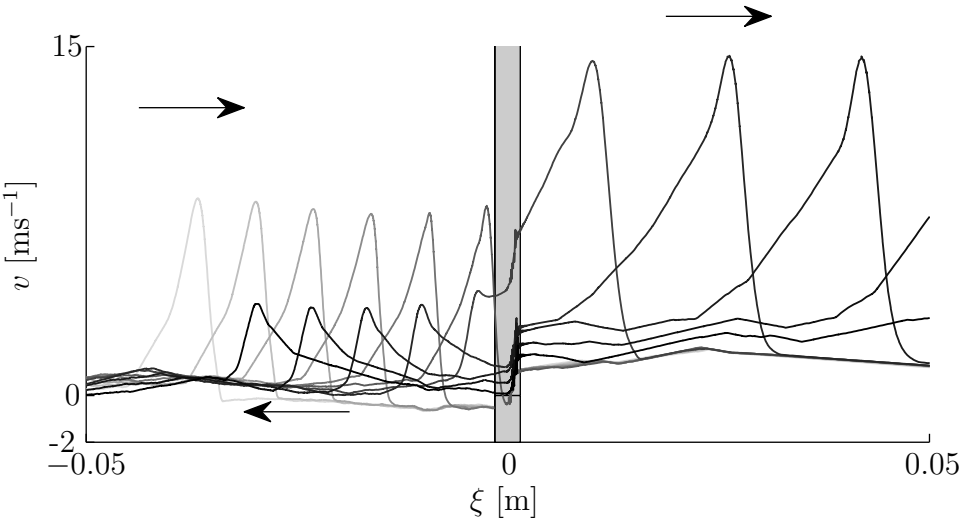

(b)

Figure 2.3.: Pressure wave-flame interaction in a fuel-lean methane-air mixture at an equivalence ratio of 0.75; (a) non-dimensional pressure field, (b) barycentric velocity. The incident pressure wave travels from the left to the right. The grey-shaded area indicates the length of the primary reaction zone. π_{ref} has a value of $1.01 \cdot 10^5$ Pa.

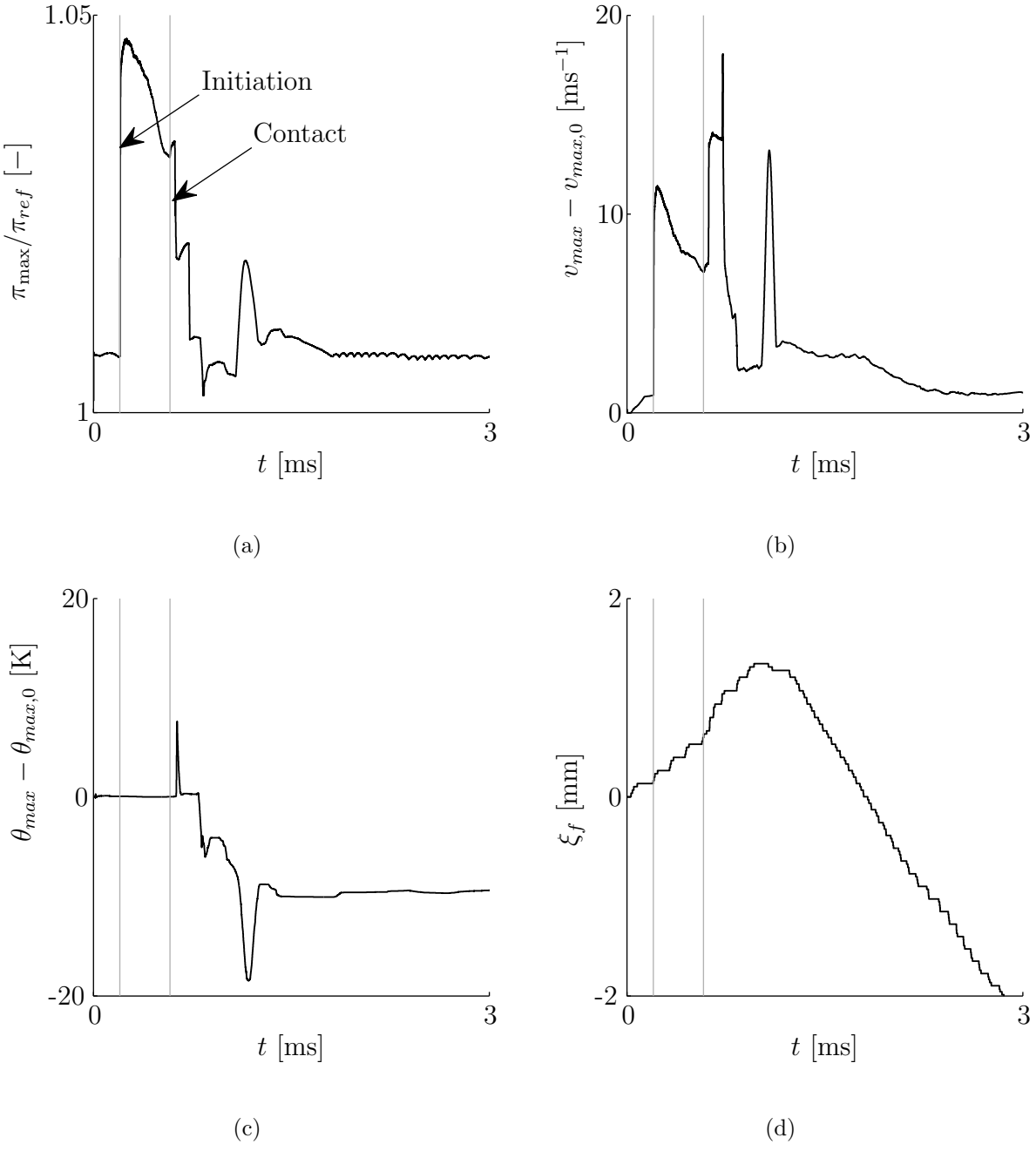

Figure 2.4.: Time history of global quantities for the fuel-lean mixture of methane and air at an equivalence ratio of 0.75; (a) maximum pressure, (b) maximum velocity, (c) maximum temperature, (d) flame position. The index 0 refers to the value at the time of the imposition of the pressure wave. π_{ref} has a value of $1.01 \cdot 10^5$ Pa.

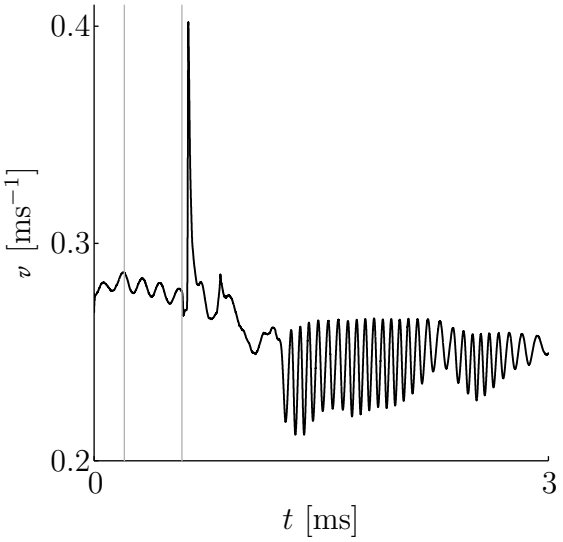

Figure 2.5.: Time history of the flame speed for the fuel-lean mixture of methane and air at an equivalence ratio of 0.75.

Qualitatively different results are obtained for the fuel-rich methane-air and fuel-lean propane-air flames. These are shown in Figure 2.6 and Figure 2.8, respectively. The amplitudes of the initial pressure waves are significantly damped before reaching the flame. This is also evident in the time history of the global maximum velocities, see Figure 2.7 (a) and 2.9 (a), respectively. Note that the chosen wave parameters are the same for all simulations. In the fuel-rich methane-air mixture [see Figure 2.6 (a)] the pressure difference between the point just ahead of and just in the back of the pressure wave increases when the wave approaches the flame. This suggests that the incident wave is essentially expansive in nature. When reaching the flame the pressure wave is damped out entirely, and so is the associated velocity wave. There is no indication of a reflected wave or wave amplification which could provide for a mechanism to initiate flame oscillation. Consistent with these observations, Figure 2.7 (d) shows a weak displacement of the flame with respect to the converged value.

In the case of the fuel-lean propane-air flame the wave flattens out rapidly after being imposed at the inlet boundary, *cf.* Figure 2.8. Hence, increasing the wave length. It is therefore possible to investigate the flame response to a wave with larger wave length than was originally intended. No reflection of the incident pressure wave occurs. Instead, the pressure wave is strongly damped. A more pronounced response is observed in the velocity field, which exposes a weaker link between pressure and velocity than was found previously in the fuel-rich methane-air flame. The incident wave becomes steeper when approaching the flame, and is then slightly amplified when travelling across the flame. This is also confirmed in the time history of the global maximum velocity shown in Figure 2.7 (b). In the course of the interaction the barycentric velocity just in front of the flame position changes in sign from negative to positive. However, across the flame layer the change of the barycentric velocity remains approximately constant during the flame-wave interaction. For this mixture composition it seems reasonable to assume that the pressure remains approximately constant across the flame layer. The flame position appears again to vary on a longer time scale than the pressure and velocity field, *cf.* Figure 2.9 (d).

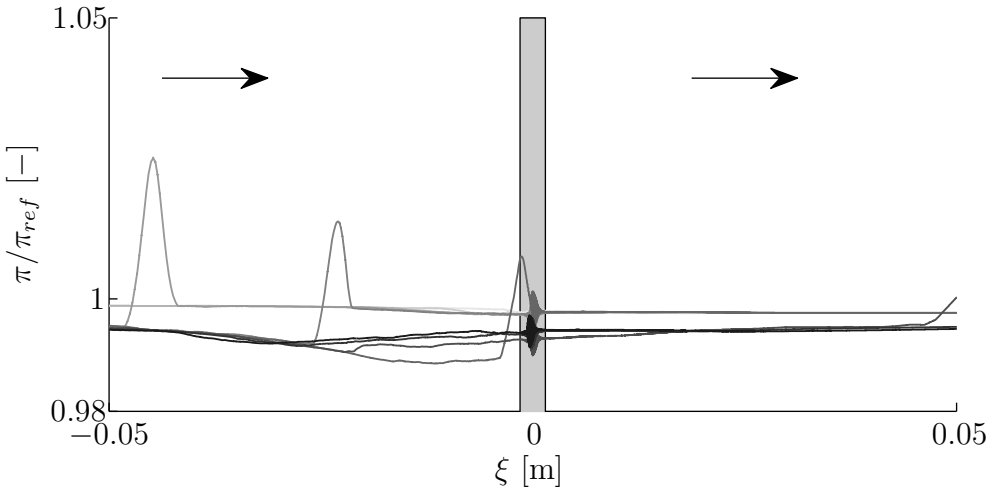

(a)

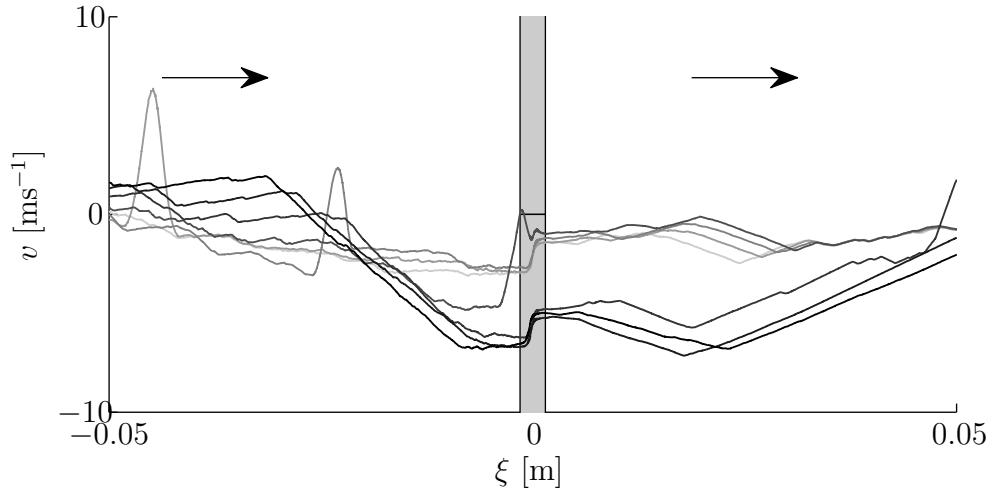

(b)

Figure 2.6.: Pressure wave-flame interaction in a fuel-rich methane-air mixture at an equivalence ratio of 1.3; (a) non-dimensional pressure field, (b) barycentric velocity. The incident pressure wave travels from the left to the right. The grey-shaded area indicates the length of the primary reaction zone. π_{ref} has a value of $1.01 \cdot 10^5$ Pa.

The results show that the flame-wave interaction in the case of the fuel-lean propane-air mixture is much weaker than in the fuel-lean methane-air mixture, which confirms that the time scale associated with the incident wave is of crucial importance. A noticeable response of the flame to pressure waves is expected only when the time scale associated with the pressure wave is of the same order as the time scales of the chemical reactions in the primary reaction zone [110]. Following this line of argument implies also that flame oscillation is unlikely initiated on wave lengths associated with the structure in which the

flame is propagating, as these are usually an order of magnitude larger.

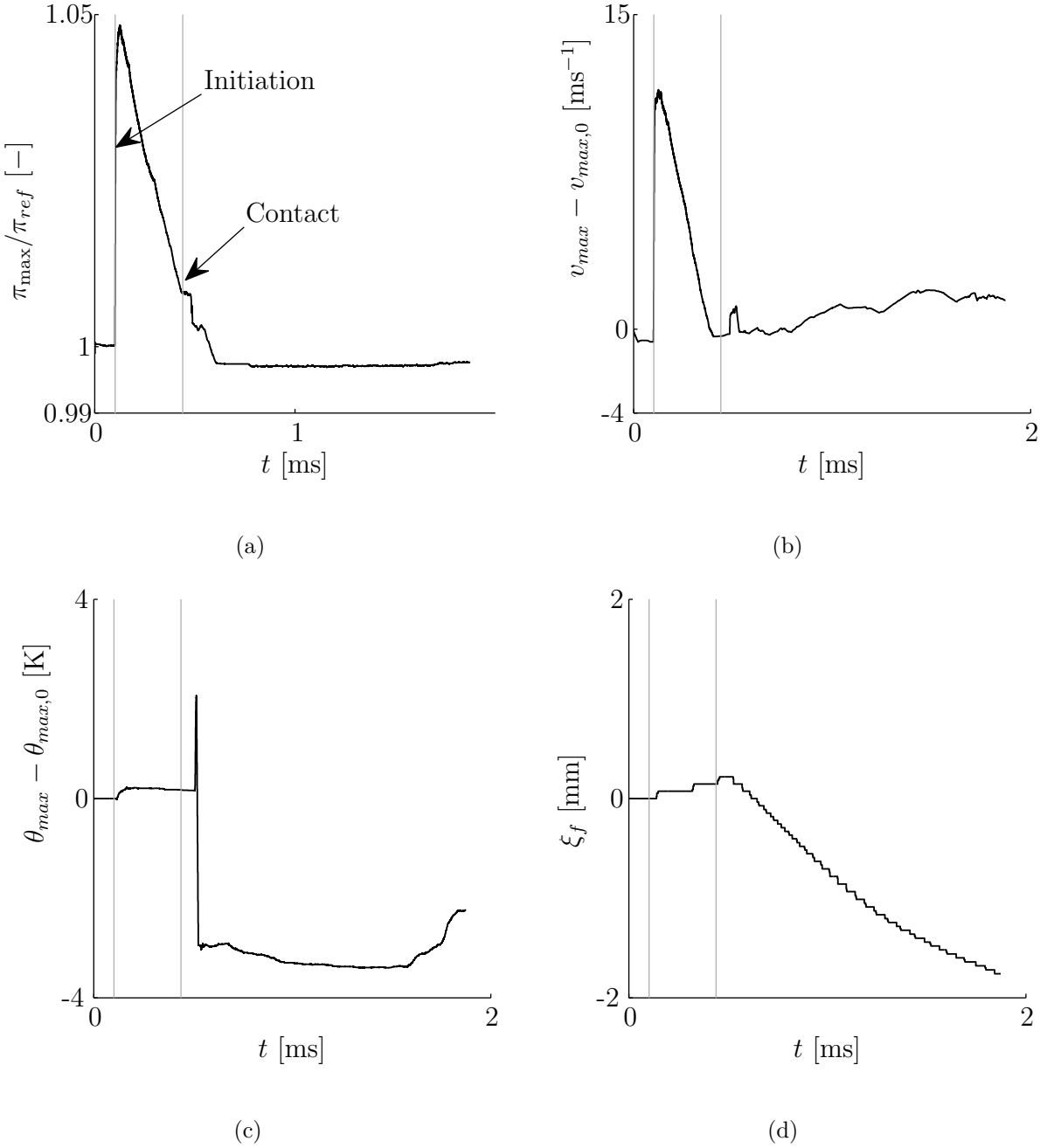

Figure 2.7.: Time history of global quantities for the fuel-rich mixture of methane and air at an equivalence ratio of 1.3; (a) maximum pressure, (b) maximum velocity, (c) maximum temperature, (d) flame position. The index 0 refers to the value at the time of the imposition of the pressure wave. π_{ref} has a value of $1.01 \cdot 10^5$ Pa.

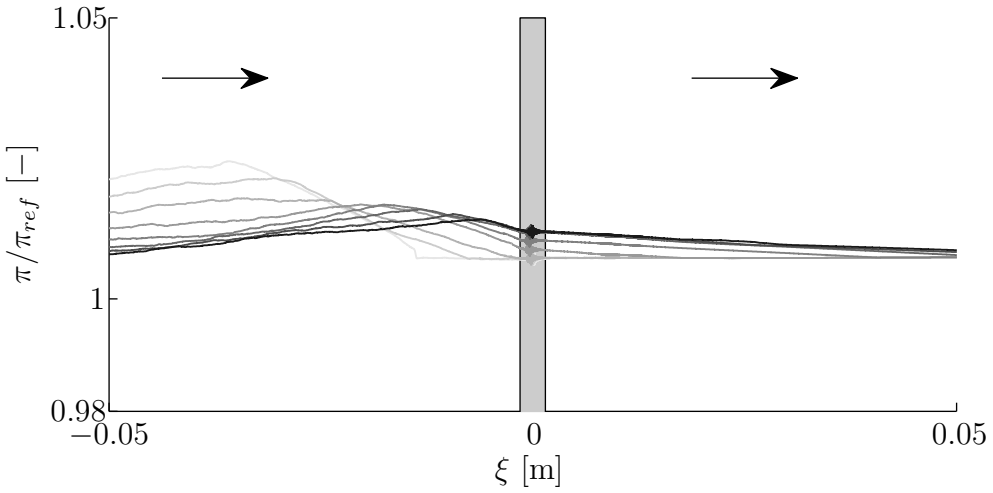

(a)

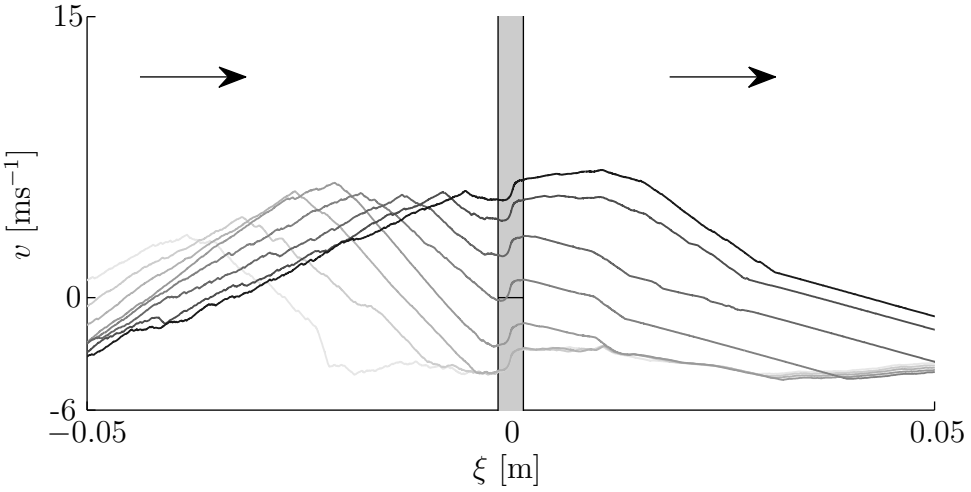

(b)

Figure 2.8.: Pressure wave-flame interaction in a fuel-lean propane-air mixture at an equivalence ratio of 0.7; (a) non-dimensional pressure field, (b) barycentric velocity. The incident pressure wave travels from the left to the right. The grey-shaded area indicates the length of the primary reaction zone. π_{ref} has a value of $1.01 \cdot 10^5$ Pa.

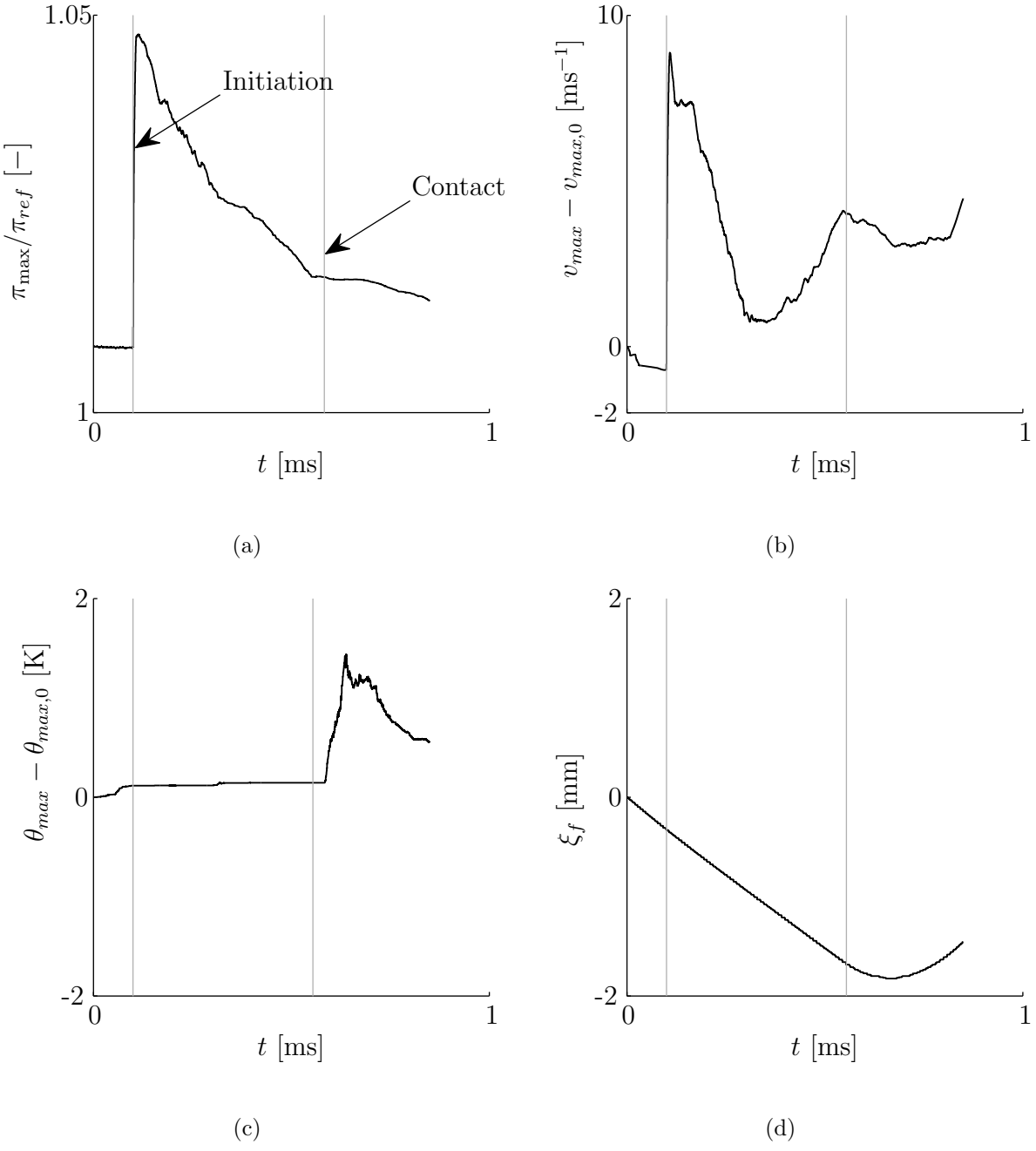

Figure 2.9.: Time history of global quantities for the fuel-lean mixture of propane and air at an equivalence ratio of 0.7; (a) maximum pressure, (b) maximum velocity, (c) maximum temperature, (d) flame position. The index 0 refers to the value at the time of the imposition of the pressure wave. π_{ref} has a value of $1.01 \cdot 10^5$ Pa.

2.5. Conclusions

The computed steady flame structures as well as flame speeds are in reasonable agreement with the measurements. The discovered mass conservation error may be minimised by employing a third-order polynomial representation. It is demonstrated that the transformation of the field equation produces numerically stable solutions of the steady flame

structure. In the study of the flame-wave interaction the following observations are made.

1.) For a fuel-lean methane-air flame at an equivalence ratio of 0.75, the imposed pressure wave is partially reflected at the flame. The amplitude of the transmitted wave is smaller than that of the incident wave. The associated velocity wave is amplified across the flame.

2.) In a fuel-rich methane-air flame at an equivalence ratio of 1.3, the incident pressure and associated velocity wave are entirely damped out.

3.) The incident pressure wave in a fuel-lean propane-air flame at an equivalence ratio of 0.7 is strongly damped, but the associated velocity wave is transmitted through the flame and slightly amplified.

The first observation suggests that the velocity wave associated with the imposed pressure wave is amplified due to the fluid acceleration across the flame layer when the wave length is of the order of the thickness of the primary reaction zone. In this way, a complex wave pattern may form through wave reflection and velocity amplification at the flame, wave reflection at the boundaries of the structure and wave-wave interaction. Hence, generating a range of wave lengths and amplitudes in the flow. The results of the fuel-rich methane-air and the fuel-lean propane-air mixture show that the equivalence ratio and the type of fuel both affect the pressure wave propagation on the unburnt side and the response of the flame to the imposed pressure wave. Systematic studies should be conducted to properly assess the effect of the wave parameters and unburnt mixture composition on the flame-wave interaction.

3. Forced Flame Oscillation

3.1. Introductory Remarks

The primary goal of the present chapter is to demonstrate a modelling framework for the simulation of oscillating turbulent flames in practical flow configurations. The ability to predict flame oscillation in the design stage of contemporary combustion chambers is of high relevance to manufacturers of gas turbine combustors, since it may reduce the development cost and number of design iterations to obtain stable operation of the combustor. The numerical model used in the present study is based on the Large Eddy Simulation (LES) technique and employs a transported Probability Density Function (PDF) approach to account for the unresolved turbulence-chemistry interaction.

The test case chosen for study is an experiment by Balachandran [7] on a forced oscillating flame stabilised in the wake of a conical bluff body. Balachandran designed the experiment to investigate the response of the flame to harmonic excitation of the mass flow rate entering the combustion chamber. The excitation of the flame is achieved acoustically by loudspeakers located far upstream of the mean flame position. In this way, the species concentrations are determined under unsteady conditions within a controlled range of wave parameters associated with the mass flow rate excitation. Balachandran demonstrates in this same configuration that the forced flame oscillation retains the characteristics of the self-excited flame oscillation in the 'limit-cycle' regime [7]. The experiment was conducted to determine the spatial distribution of the flame as a function of the phase angle with respect to the excitation signal and to investigate the dependence of the total heat release rate on the imposed wave parameters. A number of previous numerical studies on the flow in this same combustor have focused on the response of the inert air flow to acoustic flow rate excitation [5], the prediction of the Flame Transfer Function (FTF) [4], and the ignition characteristics [95].

The PDF approach used to represent the unresolved turbulence-chemistry interaction in the present simulations permits the use of detailed but reduced reaction mechanisms for the fuel oxidation. This is exploited here to identify 'chemical markers', *e.g.* chemical species, which correlate well with the total heat release rate. Such markers play an important role in experiments on reacting mixtures since the heat release rate cannot be measured directly. Instead the heat release rate is quantified experimentally by measuring a number of chemical species which are known to take part in chemical reactions with high contribution to the overall heat release rate. The chemical markers identified to properly represent the variation of the total heat release rate in the present flow configuration may help improve experimental techniques. The numerical study presented in this chapter is conducted in the following way. First, the non-oscillating cold flow is simulated to assess the resolution of the numerical grid. The harmonically excited cold flow is then simulated to validate the boundary conditions, in particular the harmonic mass flow rate excitation at the inlet boundary. This is then followed by simulating the oscillating flame and identifying suitable chemical markers for the heat release rate. The structure of the present chapter is as follows. The next section chiefly describes the experiment.

Section 3.3 details the modelling approach and section 3.4 presents the simulation results and compares them with measurements. The concluding remarks are given in section 3.5. A large part of the results presented in the following are also published in Jones *et al.* [52].

3.2. Experiment

A simple diagram of the experimental apparatus is displayed in Figure 3.1. The working fluid is a lean mixture of ethylene, C_2H_4, and air, which is premixed to an equivalence ratio of 0.55 and supplied through an injection unit in the bottom section of the apparatus. Two diametrically opposed loudspeakers used for the harmonic mass flow rate excitation are located downstream of the injection unit. The combustion chamber is open to the atmosphere at the downstream end. The mean mass flow rate is adjusted to yield a bulk-averaged axial velocity, v_b, of 10 m/s at the inlet of the combustion chamber. Together with the base diameter of the conical bluff body, $D_b = 25$ mm, this gives a cold flow Reynolds number of approximately 19,000. The current flame is in the regime of thin reaction zones on a Borghi diagram. Both bulk-averaged axial velocity v_b and bluff body diameter D_b are employed in the following as reference values for non-dimensionalising the predicted fields.

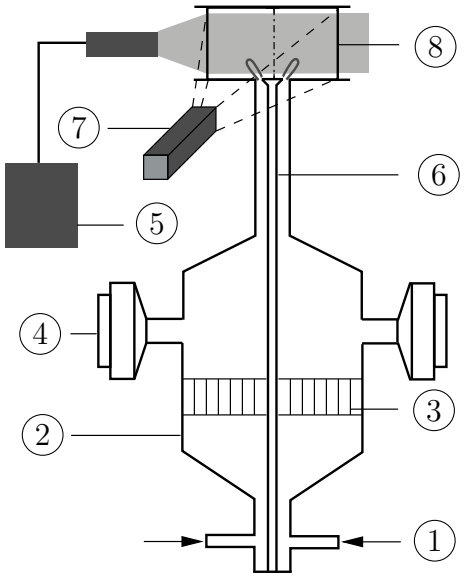

Figure 3.1.: Diagram of Balachandran [7]'s apparatus for planar laser-induced fluorescence imaging in an oscillating flame (not to scale); 1: *ethylene-air injection*, 2: *plenum chamber*, 3: *flow straightener*, 4: *loudspeaker*, 5: *laser*, 6: *bluff body with holder*, 7: *camera*, 8: *quartz tube*.

The heat release rate is quantified by chemiluminescence measurements of the chemically excited hydroxyl radical, OH^*, and planar laser-induced fluorescence of OH and formaldehyde CH_2O. Chemiluminescence of OH^* is frequently employed as an integral chemical marker since the emission intensity, I, is found to scale linearly with the consumption rate of the fuel. The OH and CH_2O fluorescence signals are recorded simultaneously in the median plane of the combustion chamber and multiplied with each other to yield an estimate of the formation rate of the formyl radical HCO. This technique is

known as Heat Release Rate Imaging (HRRI). Chemical reactions in hydrocarbon flames involving HCO take place in the secondary reaction zone along the path of the CO formation and often have a dominating influence on the overall heat release rate. HRRI is predominantly used to determine the spatial distribution of the heat release rate. The Flame Surface Density (FSD) technique falls into a similar category and is based on the post-processing of the measured OH fluorescence signal. It is important to note that the intensity scale of both the chemiluminescence and fluorescence signals is arbitrary. The measurements are thus scaled by means of the time and spatial average of the emission intensity. To investigate the evolution of the field variables in the simulation and allow for comparison with the measurements the predicted fields are phase-averaged with respect to the excitation signal at every point in the computational domain. The notation $\langle\cdot\rangle_t$, $\langle\cdot\rangle_x$ and $\langle\cdot\rangle_\gamma$ is introduced in order to distinguish between time, spatial and phase averages, respectively. $\gamma \in [0, 1]$ represents the normalised phase. Fluctuations about the phase and time average are denoted by a single and double prime, respectively.

3.3. Simulation Details

Physical Model

The motion of the mixture is modelled using the field equations (1.4)-(1.6) together with the constitutive functionals (1.7)-(1.10) presented in section 1.4. It is assumed that the material coefficients yield Schmidt numbers, $\mathrm{Sc} = \mu/(\rho m_\mathfrak{a})$, which are constant, equal for all constituents of the mixture and equal to the Prandtl number, $\mathrm{Pr} = \mu c_p/\kappa$. This greatly simplifies the numerical solution of the resulting set of differential equations. The fact that the flame oscillation is not self-excited but initiated by harmonic excitation of the mass flow rate makes it possible to treat the fluid as incompressible. The ethylene oxidation is represented by the detailed but reduced reaction mechanism of Luo *et al.* [64]. This mechanism involves 22 molecular species and 18 global reactions and was obtained by systematic reduction of a detailed mechanism comprising 75 species and 529 elementary reactions, [104]. The Large Eddy Simulation (LES) equations together with the Probability Density Function (PDF) approach to treat the unresolved turbulence-chemistry interaction are addressed in sections B.1-B.4 in appendix B. The simulations are carried out using the flow solver BOFFIN, *c.f.* section B.5.

Computational domain

The geometry of the computational domain along with the locations of the boundary conditions is presented in Figure 3.2. The computational domain includes part of the annular duct upstream of the combustion chamber, the combustion chamber, and the surrounding environment downstream of the combustion chamber. Sections of the computational grid are shown in Figure 3.3. Previous simulations of this same experiment by Ayache *et al.* [5] have guided the grid generation resulting in a computational domain which is discretised by approximately two million grid cells in 81 blocks. The grid is stretched along the axial and radial directions to allow for higher concentration of grid nodes around the bluff body and the inlet of the combustion chamber. Everywhere in the domain the grid stretching factor is maintained below 5% in order to limit errors resulting from the commutation of filtering and differentiating. The minimum axial and radial grid spacings are located in proximity to the inlet of the combustion chamber and have a value of 0.004 D_b

and 0.007 D_b, respectively.

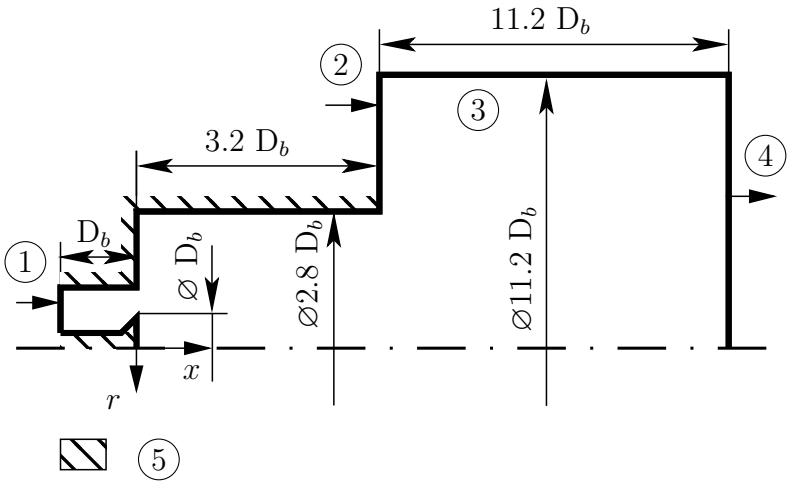

Figure 3.2.: Sketch of the computational domain and boundary conditions for the simulation (not to scale). The boundary conditions are as follows: 1: *ethylene-air inlet*, 2: *air co-flow*, 3: *free slip boundary*, 4: *zero-gradient outlet*, 5: *no-slip walls*.

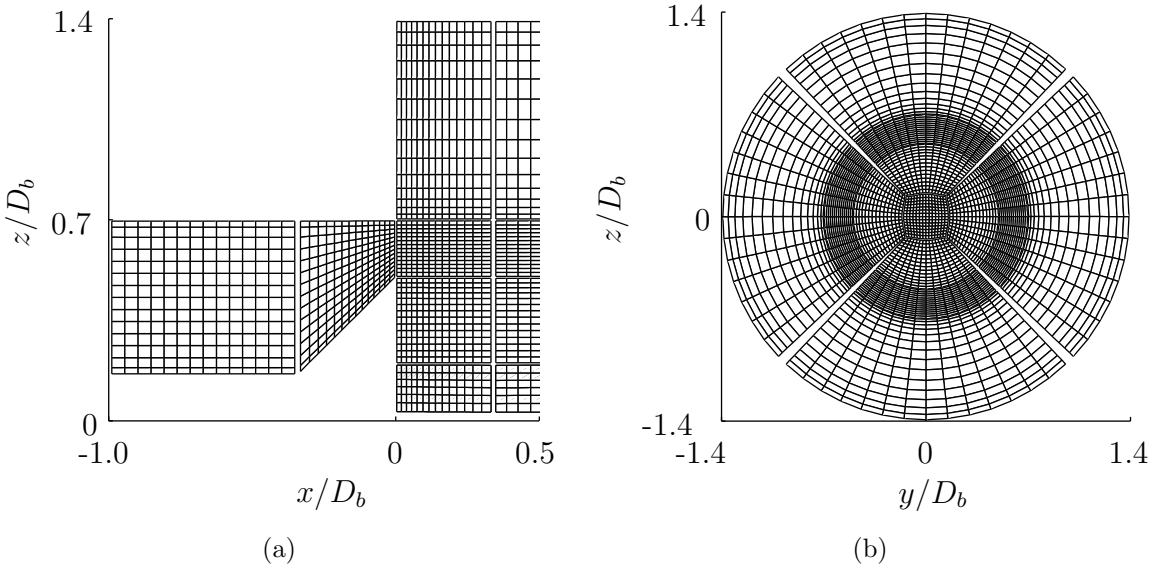

Figure 3.3.: Computational grid used in the simulations; only every second grid line is shown for clarity.

Boundary conditions

LES requires turbulent velocity inlet conditions which are here generated by using the method of Klein *et al.* [59],[27]. This method necessitates input values in the form of the components of the time-averaged velocity vector and the Reynolds stress tensor to produce realistic inlet conditions for the flow upstream of the bluff body. These quantities

are determined in a separate auxiliary simulation using the Reynolds-Averaged Navier-Stokes (RANS) solver and the Reynolds Stress Model available in the commercial software package STAR-CCM+. The computational domain of the auxiliary simulation comprises the two concentric ducts upstream of the bluff body and has a length of 10 D_b. The turbulent flow in the annular gap between the two ducts is presumed to be fully developed and therefore periodic conditions are applied at the streamwise boundaries. The length of the computational domain was chosen to ensure that the two-point correlations of the velocity field attain zero at the midpoint between the two streamwise boundaries. A forcing term is applied everywhere in the domain to maintain the given mass flow rate consistent with the experiment. The method of Klein *et al.* also requires case-specific length scales for each coordinate direction in the inlet plane, L_y and L_z, and an associated time scale, t_s, with the following values $L_y = L_z = 0.15$ D_b and $t_s = 0.0008$ D_b/v_b being selected. L_y and L_z are estimates of the integral length scale and t_s is assumed to be ten times the estimated integral time scale. Reference parameters were taken from an experimental study of Zhou [112] on the flow field of the non-reacting mixture in the Cambridge stratified swirl burner. Figure 3.4 presents the spatial distribution of the instantaneous turbulent kinetic energy in the inlet section and the computed power spectral density of the turbulent kinetic energy at $x = 0$ and $r = 0.6$ D_b. Turbulent structures, resulting from the prescribed inlet conditions, readily develop in the inlet duct, which is consistent with the observed inertial subrange in the energy spectrum, see Figure 3.4.

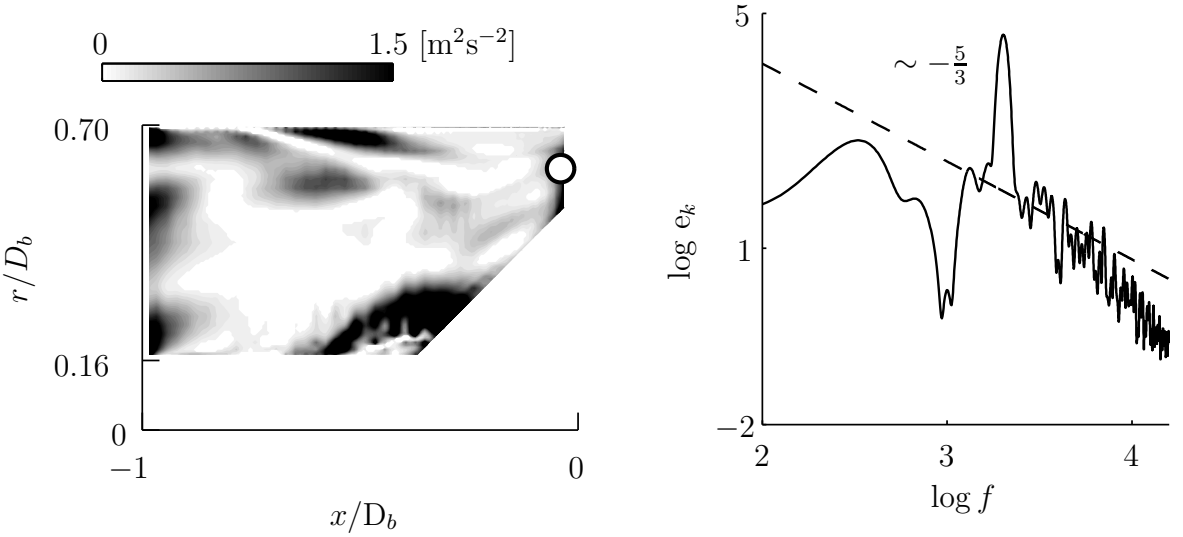

(a) (b)

Figure 3.4.: Predicted flow field in the inlet section; (a) instantaneous turbulent kinetic energy in the median plane, (b) power spectral density of the turbulent kinetic energy at $x = 0$, $r = 0.6$ D_b. The power spectral density has been obtained by subdividing the time signal into eight windows with 50% overlap. Each segment is windowed with the Hamming window function. The white point in (a) marks the monitor position at which the time history of the kinetic energy was recorded.

A sinusoid was superimposed onto the turbulent velocity signal in accordance with the

experimental conditions to simulate the oscillating flows. The fuel and oxidiser streams are premixed far upstream of the combustion chamber (~ 80 D_b) and therefore the mass fractions of the unburnt mixture are assumed to be homogeneous across the inlet plane. The temperature at the inlet is given by 293 K. Since the heat transfer at the walls is generally small compared to the heat release rate it is assumed that the walls of the combustion chamber are adiabatic. In the initial runs with the computational domain extending only to the downstream end of the combustion chamber artificial reflection in the predicted velocity field were encountered and it was therefore decided to incorporate part of the surroundings into the computational domain. The fluid being entrained by the jet at the outlet of the combustion chamber is represented by an air co-flow at a temperature of 293 K. This co-flowing stream was not present in the experiment but was included to avoid large unphysical recirculation zones in the outer region, as is common practice in the simulation of jet flows, see daSilva *et al.* [25]. The axial co-flow velocity was chosen such that the time-averaged mass flow rate is 10 % of the mass flow rate at the outlet of the combustion chamber. Decreasing the mass flow rate of the co-flow to 5 % of the mass flow rate at the outlet of the combustion chamber did not alter the flow response in the combustion chamber.

Averaging procedure

All the simulations are carried out on eleven computing nodes, where each node comprises two 2.5 GHz Quad core Intel Xeon processors. Table 3.1 summarises the respective performance characteristics for a sample simulation time of 500 time steps.

Table 3.1.: Performance characteristics

	Non-oscillating cold flow	Oscillating cold flow	Oscillating flame
# MPI processes	81	81	81
# Stochastic fields	–	–	4
Time step size [s]	$5 \cdot 10^{-6}$	$5 \cdot 10^{-6}$	$5 \cdot 10^{-6}$
Running time [s]	$7.3 \cdot 10^3$	$6.3 \cdot 10^3$	$7.6 \cdot 10^4$

The running time associated with the simulation of the oscillating flame is an order of magnitude longer than those associated with the simulation of the cold flows. This can be explained by the costly integration of the numerically stiff chemical source terms, which consumes approximately 70% of the total running time despite the parallelisation effort. The additional solution of the stochastic field equations also contributes to an increased running time. In order to let the flow attain a fully developed stage before computing the statistics each simulation was run for sixty characteristic time periods, $t_b = D_b/v_b$. In the simulation of the cold flows, statistics were gathered over a period of 450 t_b. Such a long integration time is required to obtain sufficiently smooth results for the second moments, especially in the recirculation zones where the velocities are low. Due to the increased computational demand in the case of the oscillating flame, phase-averaged statistics for this case were collected over a reduced period of 125 t_b, which corresponds to 'only' 50 cycles associated with the frequency of the forcing signal. This integration time is somewhat shorter than the integration time in the simulation of the cold flows, but yields sufficiently smooth statistics, see Figure 3.5. It should be also remarked that

the phase-averaged statistics converge faster in the simulation of the oscillating flame due to the decreased turbulence intensity. Spatial averaging in the circumferential direction is additionally performed to reduce noise in the statistical results.

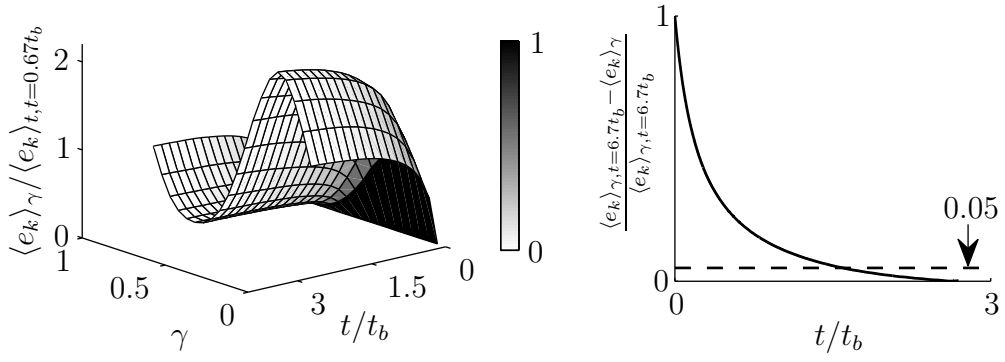

(a) (b)

Figure 3.5.: Convergence of the phase-averaged statistics for the kinetic energy at the point $x = 0$, $r = 0.6\ D_b$; (a) non-dimensional kinetic energy as a function of γ and t/t_b. The grey scale indicates the deviation of the phase-averaged kinetic energy from its profile at the final time $t = 6.7\ t_b$, (b) deviation of the kinetic energy from its value at the final time $t = 6.7\ t_b$ as a function of t/t_b for $\gamma = 0.25$.

3.4. Results and Discussion

Non-oscillating cold flow

Figure 3.6 presents contour plots of the instantaneous and time-averaged axial and radial components of the velocity vector. For later reference, Figure 3.6 (a) displays five axial stations and six probe positions at which experimental data of the time-averaged and phase-averaged flow field are available. These axial stations and probe positions are also listed in Table 3.2 and Table 3.3, respectively.

A large zone of recirculating fluid, in the remainder referred to as Central Recirculation Zone (CRZ), is formed downstream of the conical bluff body. The dimensions of the CRZ in the axial and radial directions are 1.1 D_b and 0.9 D_b, respectively. The time-averaged mean axial velocity has a minimum in the CRZ with a value of $-0.5\ v_b$ and a maximum in the annular jet with a value of approximately $+1.2\ v_b$. The dimensions of the CRZ agree closely with those determined experimentally by means of smoke visualisation, see Balachandran [7]. Shear layers develop on the inner and outer edge of the annular jet which can be concluded from the occurrence of sharp gradients of the time-averaged mean axial and radial velocity near the inlet of the combustion chamber.

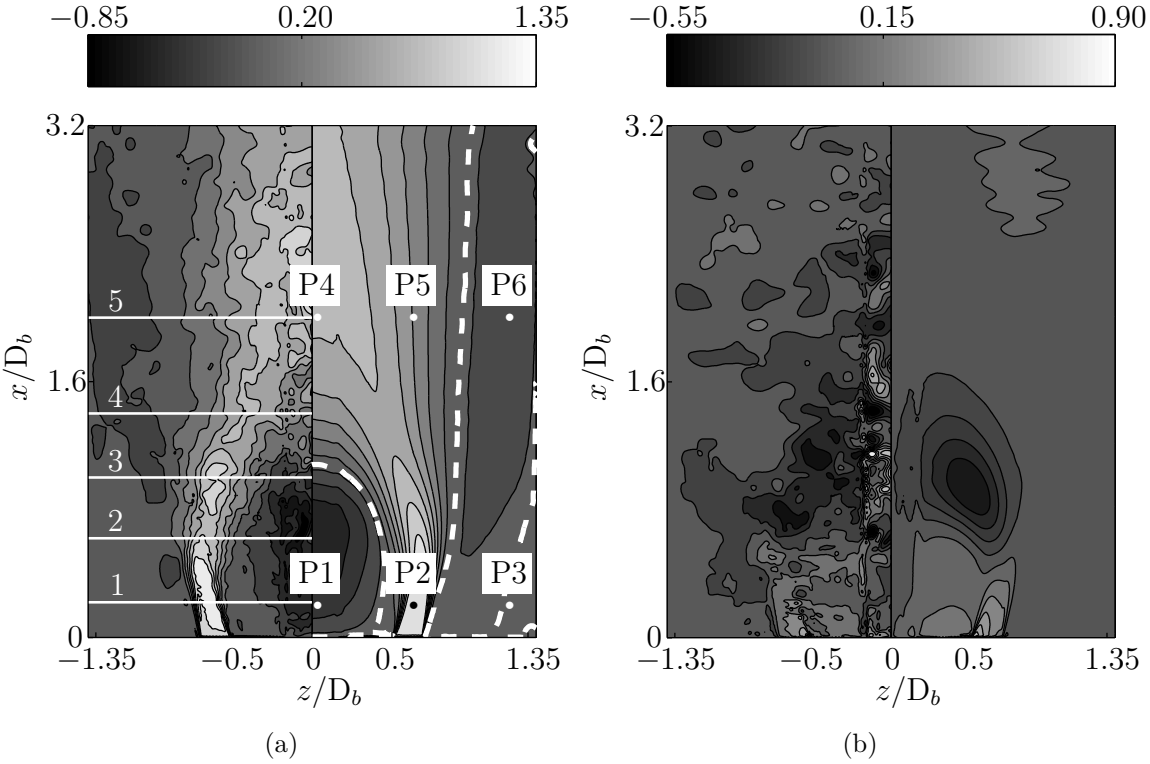

Figure 3.6.: Contour plots of the computed velocity field; *left half*: instantaneous field, *right half*: time-averaged mean field; (a) axial velocity v_x/v_b, (b) radial velocity v_r/v_b. The white dashed line represents the contour with zero axial velocity.

Table 3.2.: List of the axial stations in the experiment of Ahmed *et al.* [2].

Name	X_1	X_2	X_3	X_4	X_5
x/D_b	0.22	0.62	1.00	1.40	2.00

Table 3.3.: List of the probe positions in the experiment of Ayache et. al [5].

Name	P1	P2	P3	P4	P5	P6
x/D_b	0.2	0.2	0.2	2.0	2.0	2.0
r/D_b	0.0	0.6	1.2	0.0	0.6	1.2

The time-averaged mean radial velocity has its minimum in the expanding annular jet at the rear of the recirculation zone with $-0.4\ v_b$ and a maximum, with a value of $0.5\ v_b$, in the annular jet in proximity to the inlet of the combustion chamber. It is important to note that the outer shear layer does not re-attach at the wall of the combustion chamber. Instead, a large annular recirculation zone, subsequently referred to as Outer Recirculation Zone (ORZ), occupies the region between the wall and the outer shear layer. The ORZ extends to the exit of the combustion chamber which exerts significant influence on the required dimensions of the computational domain, as was remarked upon earlier. This

prohibits the imposition of boundary conditions directly at the exit of the combustion chamber. Consequently, parts of the surrounding environment were incorporated into the computational domain.

Radial profiles of the predicted time-averaged mean and root-mean-square of the axial velocity at the five axial stations listed in Table 3.2 are compared with measurements in Figure 3.7. The predictions compare well with the experimental data at all axial stations. Especially the dimensions of the recirculation zone are in excellent agreement with the measurements. Both the spreading of the annular jet and the decaying turbulence levels in the shear layers are well captured.

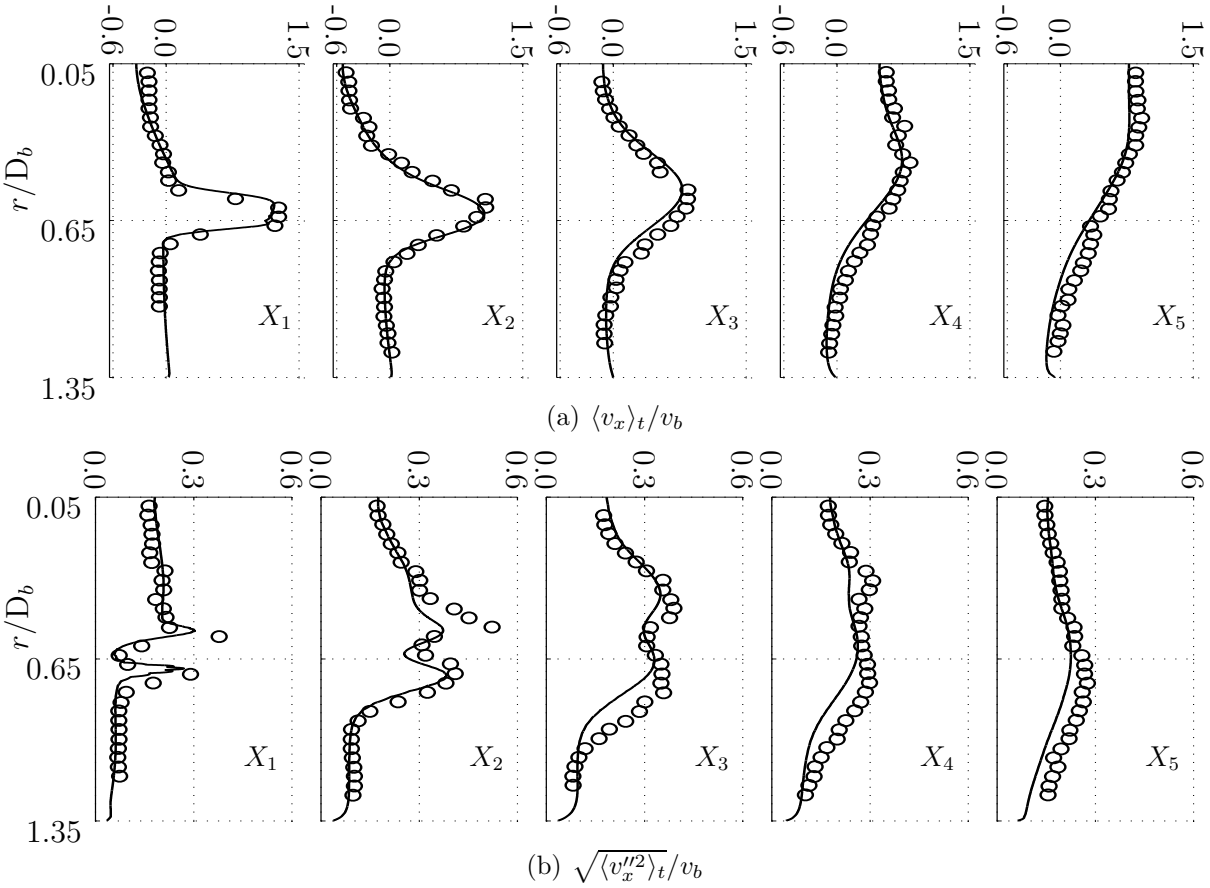

Figure 3.7.: Statistical profiles for the axial velocity; *symbols*: experiment [2], *solid lines*: simulation; (a) time-averaged mean, (b) root-mean-square.

Radial profiles of the time-averaged mean and root-mean-square of the radial velocity at the same axial stations are shown in Figure 3.8. The predicted results compare well with the measurements. The shape of the widening annular jet is yet again well captured. However, the turbulence levels in the outer shear layer near the combustor inlet are underpredicted by approximately 70 %. This discrepancy may be attributed to the intermittent nature of the flow in this region, which could potentially lead to an excess of sub-filter diffusion caused by large values of the computed sub-filter viscosity. In spite of this, the levels of the fluctuations recover further downstream and better agreement with the measurements is obtained. Although the length of the annular duct upstream of the combustion chamber is relatively short, the agreement between the predictions and the measurements near the inlet of the combustion chamber is satisfactory. This leads to the

conclusion that the approach taken here to generate turbulent inflow conditions is appropriate. Moreover, the obtained results suggest that the resolution of the computational grid is sufficient.

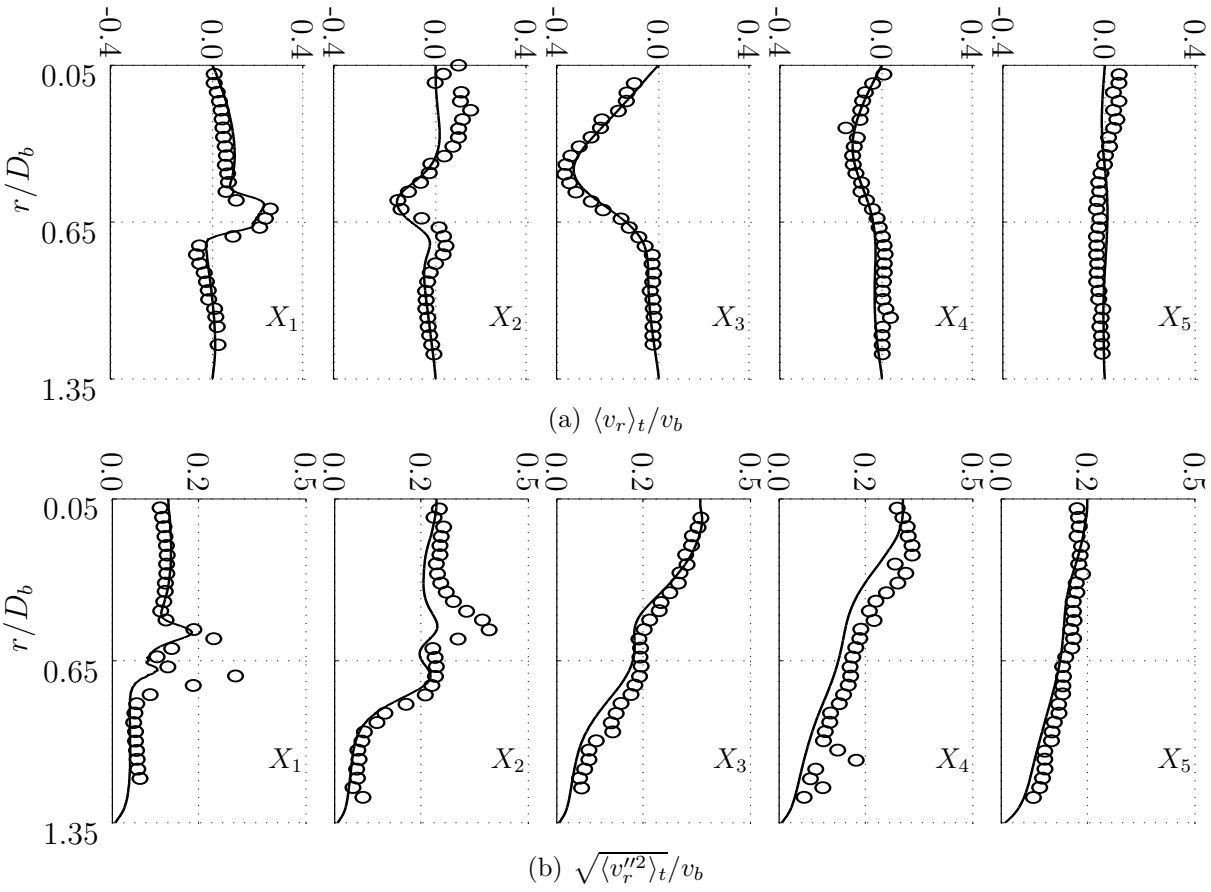

Figure 3.8.: Statistical profiles for the radial velocity, *symbols*: experiment [2], *solid lines*: simulation; (a) time-averaged mean, (b) root-mean-square.

Oscillating cold flow

The phase-averaged statistics of the measurements are computed by taking the input signal to the loudspeakers located in the plenum chamber as a reference. The simulations, however, do not resolve the flow in the plenum chamber, but only part of the annular duct upstream of the bluff body with the obvious reference signal being the imposed excitation at the inlet of the computational domain. Hence there is a phase shift between the phase-averaged statistics of the measurements and the predictions. It was therefore decided to adjust the phase of the experimental results manually to allow for comparison with the predictions. The same is done in the case of the oscillating flame.

Three different parameter sets for amplitude and frequency of the excitation signal are investigated here: $(0.89\ v_b, 0.1\ v_b/\mathrm{D}_b)$, $(0.60\ v_b, 0.4\ v_b/\mathrm{D}_b)$ and $(0.70\ v_b, 0.8\ v_b/\mathrm{D}_b)$. For $(0.89\ v_b, 0.1\ v_b/\mathrm{D}_b)$, Figure 3.9 compares the predicted phase-averaged axial velocity with the measurements at the six probe positions listed in Table 3.3. The predictions are in close agreement with the measurements at the positions P1-P3. The profiles at P2 have a sinusoidal shape following the excitation with a sinusoidal signal. Only a minor phase shift between the reference signal and the predicted profile is observed. Internal

dissipation and lateral momentum transfer lead to an attenuation of the amplitude of the oscillating velocity along the downstream direction. Thus, the amplitude at P5 decreases to approximately 30% of its value at P2. The phase shift between the maxima at P2 and P5 is 0.2, which corresponds to a time period of 2.0 D_b/v_b or phase velocity of 0.9 v_b. This finding suggests that the imposed velocity oscillation propagates in the annular jet with approximately the reference velocity v_b. An interesting observation is the apparent frequency doubling occurring inside the CRZ, as concluded from P1. When assuming the profile P1 to be representative of the bulk behaviour of the CRZ this implies an inherently different natural frequency of the CRZ in comparison to the annular jet. This is further substantiated by the fact that the frequency doubling is absent at the downstream position P4, which lies just outside the CRZ. Although driven at the frequency of the annular jet the ORZ shows a weak response near the upstream panel of the combustion chamber, see P3. Yet again the situation is reversed at the downstream position. The profiles at P6 exhibit a discernible oscillation of the axial velocity indicating that the ORZ is excited at the frequency of the annular jet. Moreover, the velocity oscillation at P6 is in phase with the excitation signal. There is a clear phase shift between the profiles at P6 and those at P4 and P5, which suggests that the ORZ responds with a different time-lag than the annular jet and the CRZ to the imposed excitation.

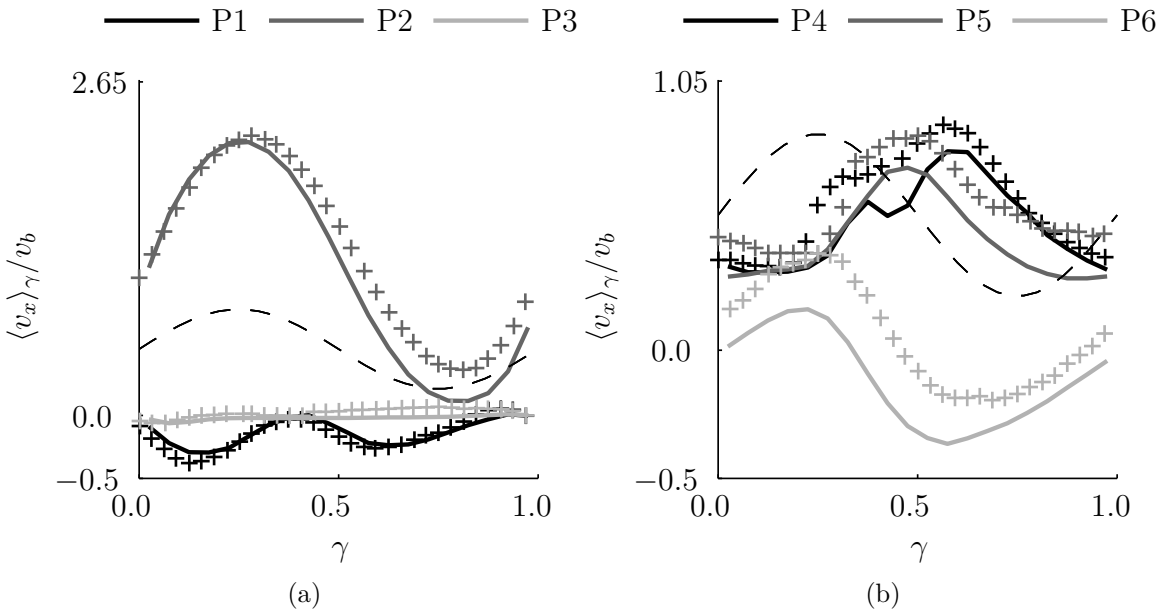

Figure 3.9.: Phase-averaged axial velocity non-dimensionalised by v_b as a function of phase angle at the six probe positions listed in Table 3.3. The imposed excitation parameters are $(0.89\ v_b, 0.1\ v_b/D_b)$; *symbols*: experiment, *solid lines*: simulation, *dashed line*: reference signal imposed at the inlet.

The predicted root mean square of the fluctuations of the axial velocity are compared with measurements in Figure 3.10. Large deviations between the predictions and measurements are evident at the upstream positions P1 and P2. The simulation overpredicts the turbulence levels in the annular jet by approximately 50 % at the normalised phase angle $\gamma = 0.5$. The cause of this discrepancy could not be identified. Although the velocities in this region are low resulting in a slow convergence rate of the phase-averaged statistics, the integration time was sufficient to produce reliable statistical results in this region.

At the downstream positions P4-P6 the predicted results are in much better agreement with the measurements. All the profiles exhibit a peak at a phase angle of $\gamma = 0.35$. The level of the fluctuations at these downstream positions is higher than those in the non-oscillating flow.

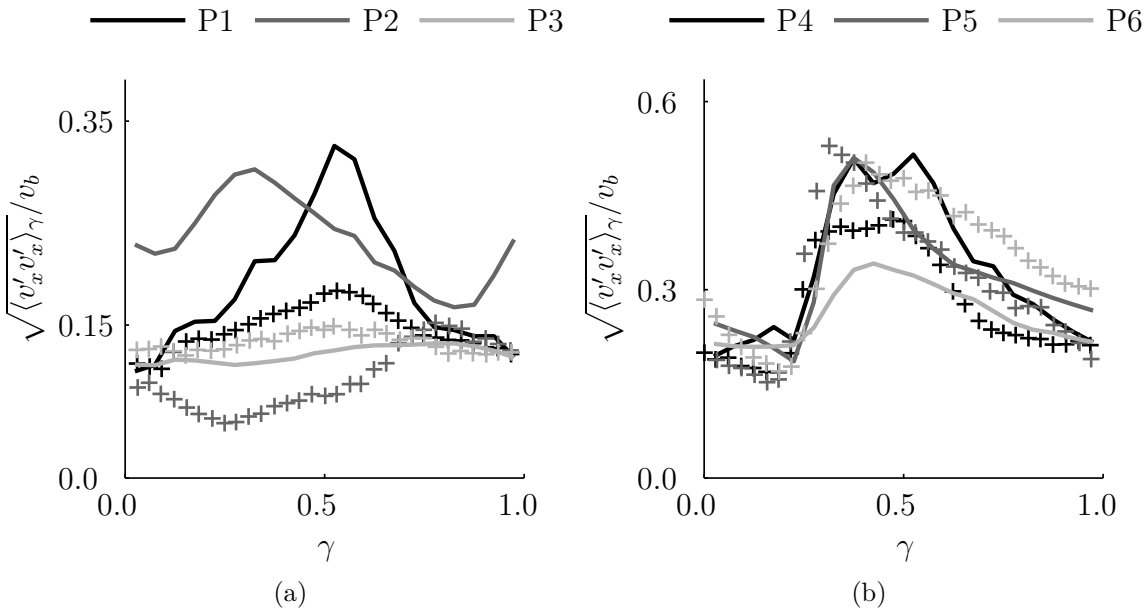

Figure 3.10.: Root mean square of the fluctuations of the axial velocity about the phase average non-dimensionalised by v_b as a function of phase angle at the six probe positions listed in Table 3.3. The imposed excitation parameters are $(0.89\ v_b, 0.1\ v_b/\mathrm{D}_b)$; *symbols*: experiment, *solid lines*: simulation.

A very similar trend emerges in the results for the next flow condition $(0.60\ v_b, 0.4\ v_b/\mathrm{D}_b)$. These same excitation parameters are also chosen in the simulation of the oscillating flame discussed below. The predicted phase-averaged axial velocity for this case is shown together with the measurements in Figure 3.11. Generally, good agreement is found between the predictions and the measurements at all probe positions. Especially the profile shapes are well reproduced. At P2 in the annular jet the profiles take again the shape of a sinusoid, but the simulation underpredicts the velocity values in the range $\gamma \leq 0.25$ and $\gamma \geq 0.75$ by approximately 30 %. This leads to an underprediction of the time-averaged mean which is also observed in the non-oscillating flow, see Figure 3.7. That this discrepancy occurs so close to the inlet of the combustion chamber may be an indicator of a slight difference in the incoming mass flow rate between experiment and simulation. In contrast to the preceding case, the profiles at P1 do not exhibit the characteristic frequency doubling. The results at P1 and P3, however, suggest that both the CRZ and ORZ are marginally excited at the frequency of the imposed signal. Since there is no observable phase shift between the excitation signal and the flow field response at the downstream positions P4 to P6 implies that the time scale associated with the convection of the imposed velocity oscillation is approximately the same as the time period associated with the frequency of the excitation signal. The velocity values at P6, although showing clearly an oscillatory behaviour, are negative. One may conclude from this finding that the ORZ extends too far downstream, which again may be connected with the speculated difference in the mass flow rate between experiment and simulation.

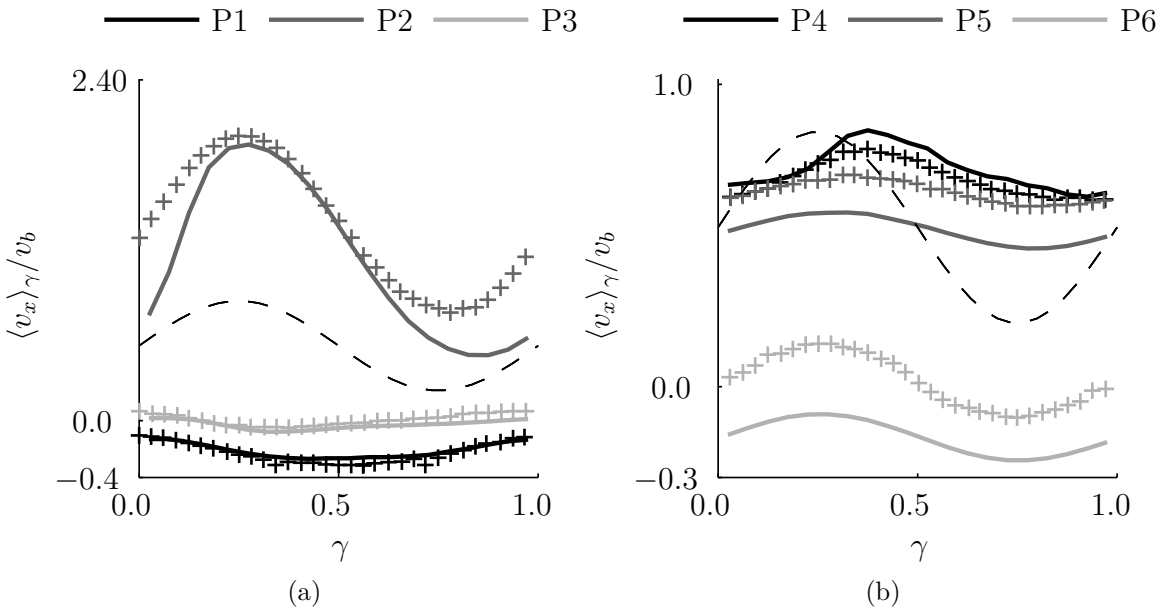

Figure 3.11.: Phase-averaged axial velocity non-dimensionalised by v_b as a function of phase angle at the six probe positions listed in Table 3.3. The imposed excitation parameters are $(0.60\ v_b, 0.4\ v_b/\mathrm{D}_b)$; *symbols*: experiment, *solid lines*: simulation, *dashed line*: reference signal imposed at the inlet.

Less satisfactory agreement is achieved with respect to the root mean square of the fluctuations of the axial velocity, see Figure 3.12.

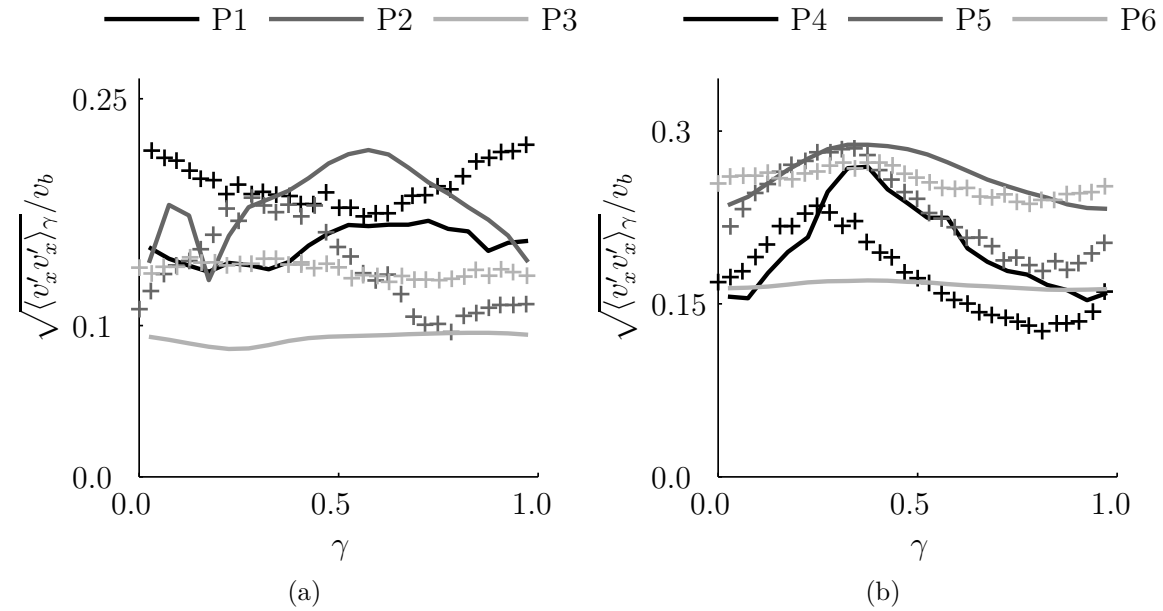

Figure 3.12.: Root mean square of the fluctuations of the axial velocity about the phase average non-dimensionalised by v_b as a function of phase angle at the six probe positions listed in Table 3.3. The imposed excitation parameters are $(0.60\ v_b, 0.4\ v_b/\mathrm{D}_b)$; *symbols*: experiment, *solid lines*: simulation.

Noticeable discrepancies between the predicted and experimentally determined profiles are

found at the upstream positions P1 to P3. The agreement at the downstream positions P4-P6 is overall better. From the streamline pattern in Figure 3.13 one can conclude that the shear layers between the radially widened annular jet and the recirculation zones pass periodically through the probe positions P2 and P3. Hence, the flow is intermittent in this region. The turbulence model, as was remarked upon in the above discussion of the results of the non-oscillating cold flow, can produce some inaccuracies in these regions.

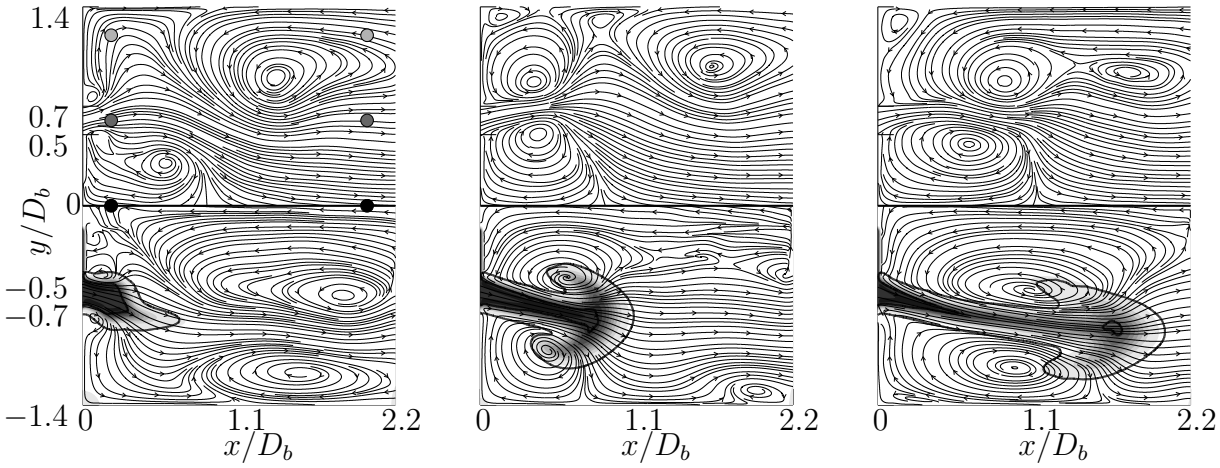

(a) $\gamma = 0.0$ (b) $\gamma = 0.3$ (c) $\gamma = 0.6$

Figure 3.13.: Streamline pattern for the oscillating cold flow (*upper half*) and the reacting mixture (*lower half*). The thick black line in the lower half represents the flame contour. The temperature field is coloured with greyscale. Dark and bright levels represent low and high temperatures, respectively. The six greyscale points in (a) mark the probe positions listed in Table 3.3

Best agreement between simulation and experiment is obtained in the remaining case ($0.70\ v_b, 0.8\ v_b/\mathrm{D}_b$). The phase-averaged mean axial velocity is at all probe positions in excellent agreement with the measurements, see Figure 3.14. Although the amplitude of the excitation signal is high, the velocity shows a weak response at the downstream positions P4-P6. When taking the results of the previous flow conditions into account it appears that the bulk of the fluid motion behaves like a low-pass filter. In comparison to the other two flow conditions, the profile at P2 departs noticeably from the sinusoidal shape which is primarily an effect of the higher frequency of the excitation signal. In addition, the flow response at this position lags behind the excitation by a phase difference of approximately 0.11. The maximum value of the velocity oscillation at P5 has attenuated to 24 % of its value at P2. The crossings about the time-averaged mean value at P5 and P6 almost coincide with those of the reference signal, implying a phase lag of 1.0.

Good agreement between simulation and experiment is also obtained for the root mean square of the fluctuations about the phase average displayed in Figure 3.15. The trends are reproduced satisfactorily at all probe positions. However, the simulation overpredicts the measurements at P1 and P2 by approximately 20 % and 50 %, respectively.

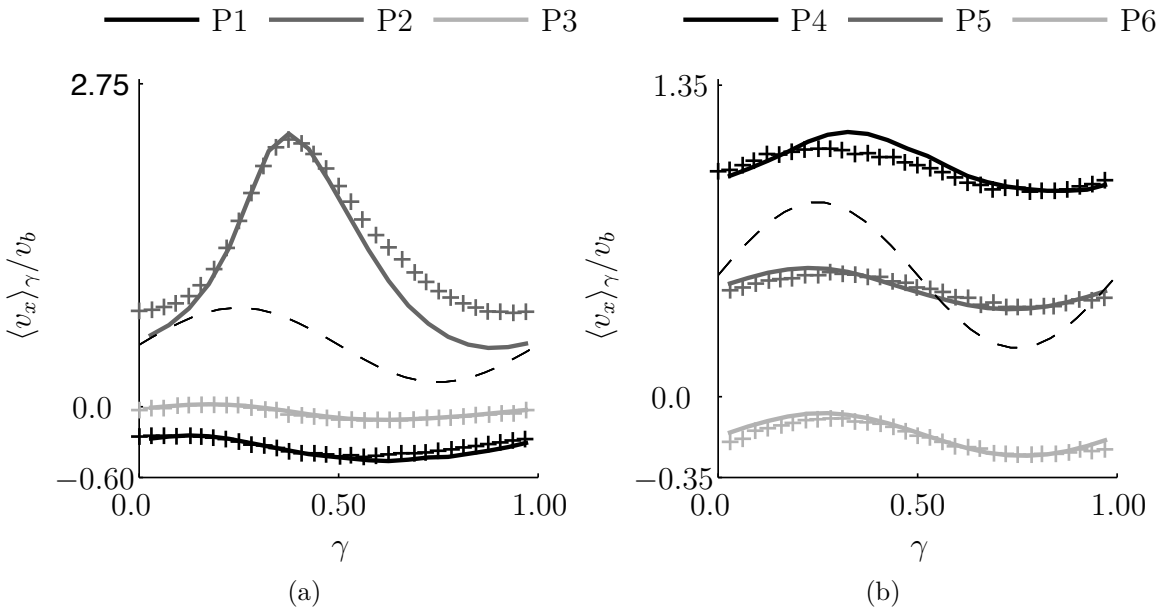

Figure 3.14.: Phase-averaged axial velocity non-dimensionalised by v_b as a function of phase angle at the six probe positions listed in Table 3.3. The imposed excitation parameters are $(0.70\ v_b, 0.8\ v_b/\mathrm{D}_b)$; *symbols*: experiment, *solid lines*: simulation, *dashed line*: reference signal imposed at the inlet.

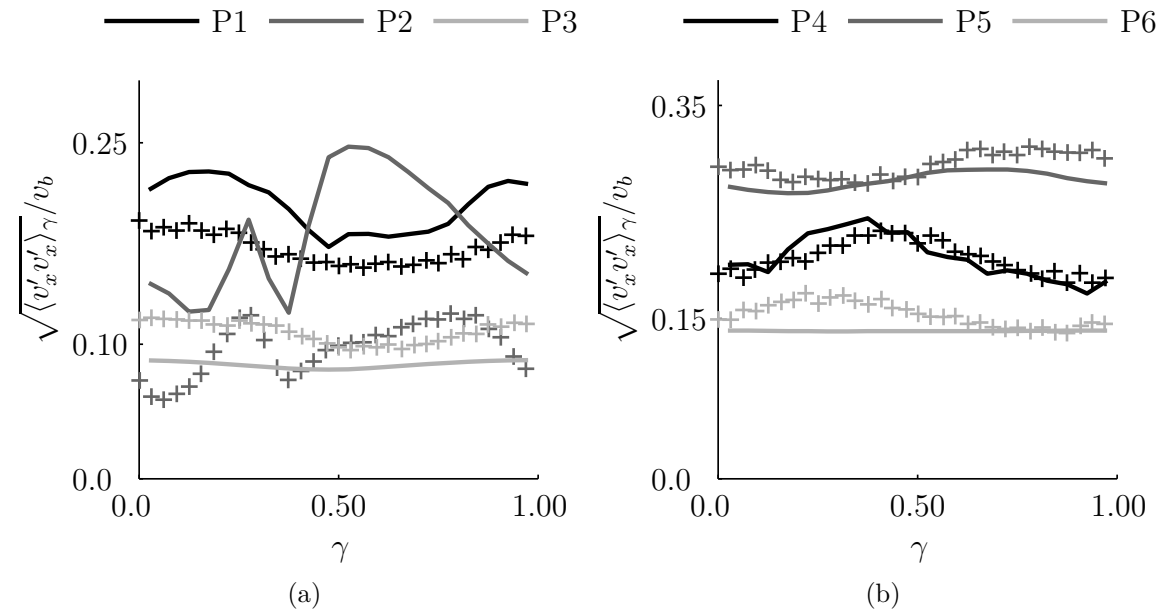

Figure 3.15.: Root mean square of the fluctuations of the axial velocity about the phase average non-dimensionalised by v_b as a function of phase angle at the six probe positions listed in Table 3.3. The imposed excitation parameters are $(0.70\ v_b, 0.8\ v_b/\mathrm{D}_b)$; *symbols*: experiment, *solid lines*: simulation.

The approach taken here to superimpose a sinusoid onto the turbulent velocity signal generated with Klein's method is in light of the obtained results justified. On this basis it was decided to use the same approach for generating inflow conditions in the simulation of

the oscillating flame. The phase-averaged mean and root mean square of the fluctuations of the axial velocity predicted by the simulation are in reasonable agreement with the measurements throughout. In general, better agreement is found for the phase-averaged mean velocity, especially in the annular jet at P2. Discrepancies in the root mean square of the fluctuations are mostly limited to the upstream positions P1-P3, where the velocities are low.

Oscillating Flame

Figure 3.13 shows the temporal evolution of the spatial extent of the flame together with the streamline pattern of the velocity field. The spatial extent of the flame is visualised by means of the contour of the heat release rate at a value of 15 % of its global maximum. It should be acknowledged, however, that the variation of the contour level affects slightly the resulting shape of the flame at its downstream end. This is due to the gradient of the predicted heat release rate being lower at the downstream end of the flame than in the shear layers between the annular jet and the surrounding recirculation zones. Similar to the results of the oscillating cold flow, both the CRZ and ORZ are formed, albeit with different axial extents and shifted with respect to the phase angle. It is further observed that, in the case of the reacting mixture, the axial extents of the CRZ and ORZ vary more significantly during the cycle. At the same time the flame elongates in the axial direction by a factor of four and becomes thinner in the cross direction. The CRZ and ORZ deform the flame in the radial direction which results in the distinct 'mushroom'-like structure at $\gamma = 0.3$.

The shape of the predicted flame is compared with measurements in Figure 3.16. In comparison to the prediction the experimental data is more scattered and this is due to two reasons. First, the projected pixel size of the camera is $50 - 70$ μm and thus smaller than the smallest dimension of the grid cell, namely 100 μm. On average, the grid cells along the combustion chamber are $10 - 20$ times larger than the minimum grid cell dimension. Hence, turbulent structures in the simulation cannot be resolved to the same level as in the experiment. Second, the phase-averaged statistics of the experimental data are computed using 'only' $75 - 100$ images per phase bin [7]. Whereas in the simulation, 3300 data samples are collected per phase bin, which results in a better statistical reliability than in the experiment. Despite the scatter in the experimental data the comparison identifies potential deviations between experiment and simulation. The results of the simulation are in good agreement with the experimental data for $0 \leq \gamma \leq 0.5$. The closest agreement is at $\gamma = 0.3$, when the flame is at a distance to the surrounding structure. Both the angle of the flame with respect to the centre axis and the characteristic 'mushroom' shape are well reproduced. A rather significant deviation between experiment and simulation occurs at $\gamma = 0.6$. The results of the simulation suggest a deflection of the flame towards the centre axis, whereas both HRRI and FSD indicate that the flame interacts with the wall. This appears to be a direct consequence of the assumption that the wall boundaries do not admit heat transfer. Such an assumption is clearly violated when the flame approaches the wall and hence must be reviewed in future investigations. As a result of the incorrect boundary treatment the stagnation point at the combustor wall as well as the ORZ are shifted further downstream. The ORZ functions then as a hydrodynamic 'cushion' between the flame and the wall and directs the flame away from the wall. That this is indeed the case implies the observation that the tail of the flame in the later stages of the cycle remains approximately parallel to the wall. Another anomaly observed in the simulation is the local extinction of the flame at $\gamma = 0.85$. It is verified that this is not an

artifact of the flame visualisation by reconstructing the contour of the flame at different levels of the heat release rate. The predicted results show unequivocally that the tail of the flame extinguishes inside the annular jet at approximately $x/\mathrm{D}_b = 1.9$ and $r/\mathrm{D}_b = 0.9$, dividing the flame into two parts.

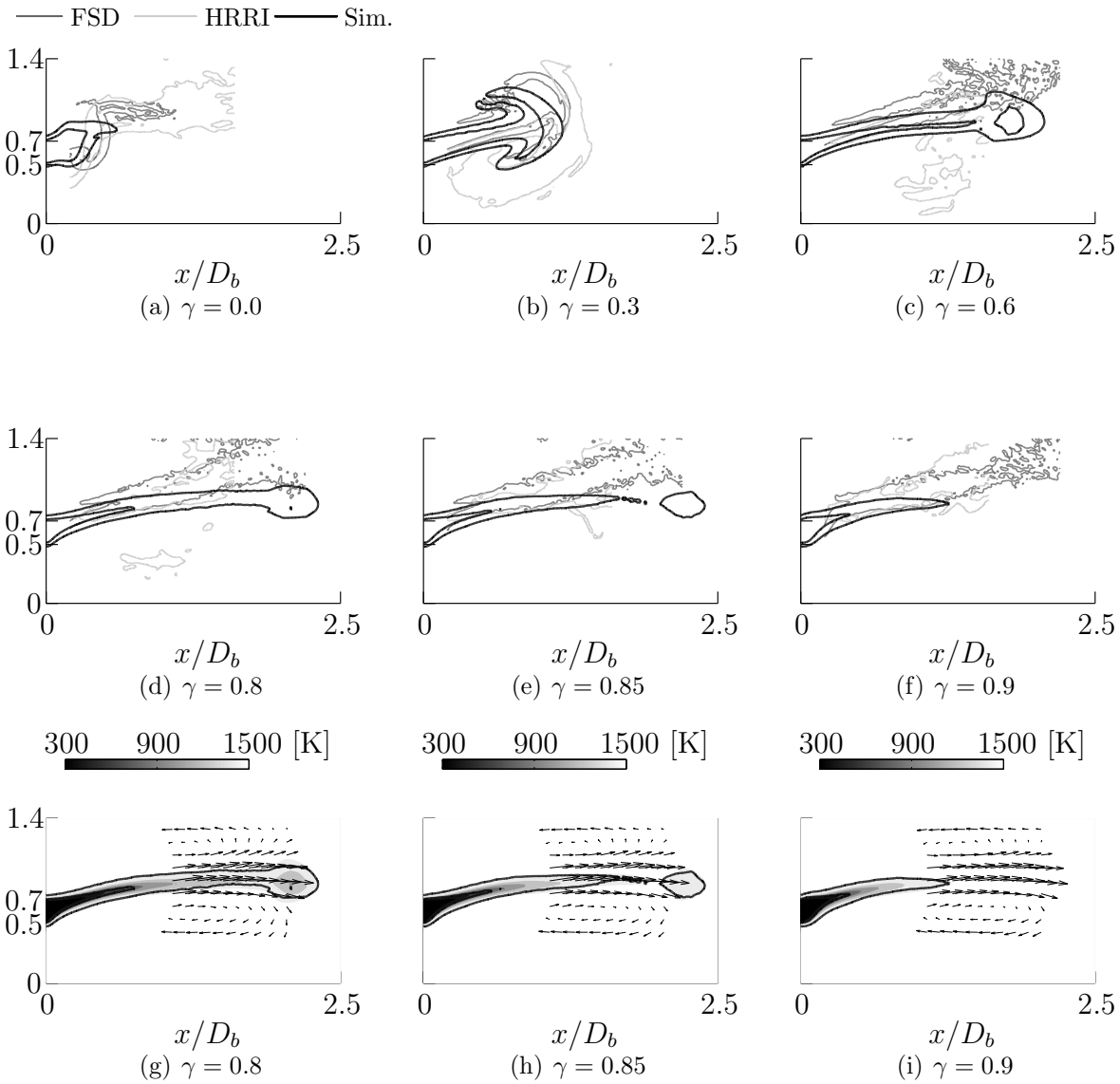

Figure 3.16.: Spatial extent of the reaction zone; (a)-(f) contour of the heat release rate, *dark grey line*: FSD data of Balachandran [7], *light grey line*: HRRI data of Ayoola [6], *black line*: simulation, (g)-(i) filled grey contours represent the predicted temperature field, the black solid line is the contour of the heat release rate at a value of 15 % of the global maximum, and arrows represent the velocity field.

The fluid temperature at the extinction point is close to the temperature on the burnt side and the radical mass fractions become insignificantly small, which suggests that the mixture approaches a fully burnt state. Beyond the extinction event the upstream part of the flame propagates back upstream towards the inlet of the combustion chamber while the downstream part swiftly extinguishes. Figure 3.11 shows that the axial velocity in

the annular jet close to the combustor inlet (P2) is at its minimum at $\gamma = 0.8$. With a time delay this minimum is experienced further along the annular jet and assumes a value which is less than the flame speed at the downstream end of the flame. As a result, the flame propagates upstream relative to the fluid motion and an annular 'necking' region forms at the intersection between the elongated and the radially-widened part of the flame ($x/\mathrm{D}_b = 1.9$ and $r/\mathrm{D}_b = 0.9$), *c.f.* Figure 3.16 (g)-(i). The flame then gradually propagates into opposite directions in the necking region which eventually detaches the elongated from the radially widened part of the flame. Any influence exerted by the stretching rates on the flame extinction is small, since the flame extinction takes place well within the annular jet.

Figure 3.17 (a) compares the measured OH* chemiluminescence with the predicted total heat release rate, Q_{tot}. The time-averaged mean value of Q_{tot} is 6.1 kW.

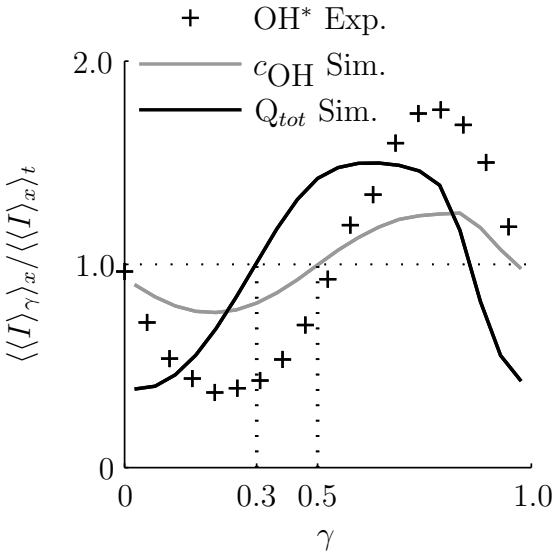

Figure 3.17.: Heat release rate as a function of phase; *symbols*: experimentally determined intensity scale of Balachandran [7], *solid lines*: simulation.

Figure 3.17 (a) shows a rather significant phase shift of (0.2 ± 0.056) between the OH* chemiluminescence and Q_{tot}. This requires further investigation. Due to the fact that the mass fraction of the chemically excited hydroxyl radical, c_{OH^*}, cannot be estimated within the present framework, the ground state OH mass fraction is used to examine the observed phase shift. Justification for the use of c_{OH} is based upon the findings of Hall *et al.* [47]. The authors demonstrate that the ratio $c_{\mathrm{OH,max}}/c^*_{\mathrm{OH,max}}$ remains approximately constant over a wide range of temperatures in a stoichiometric ethane-oxygen flame. Hall *et al.* also found that both OH and OH* tend to exhibit initial rapid formation around the same time for some of the investigated flames (fuel-rich and fuel-lean acetylene-oxygen and ethane-oxygen flames), leading to approximately the same ignition onset times. Their findings provide some basis for an in-phase transient behaviour of OH and OH*, although their absolute concentrations may differ by large amounts. This could be, in principle, also accounted for by calibration using a mechanism for the formation of OH* and its subsequent return to the ground state, but this is not required here. To allow for proper comparison with the OH* chemiluminescence, the line-of-sight integration method of Ruder *et al.* [82] is applied to the predicted ground-state OH mass fraction.

The resulting variation of the integral value is shown in Figure 3.17 (a). The predicted c_{OH} has approximately the same phase shift with respect to Q_{tot} as the measured OH^* chemiluminescence. Although OH^* chemiluminescence is appropriate to determine the maximum and minimum values of the Q_{tot} variation it is not properly representing the phase with respect to the excitation signal. The maximum value of the OH^* variation is approximately 15 % higher than the corresponding value of Q_{tot}. This is due to the different flame dynamics, *i.e.* the absence of the flame-wall interaction in the simulation. However, the shape of the non-linear evolution of Q_{tot} compares well with the integral value of the OH^* chemiluminescence. Figure 3.18 reveals that large fractions of the predicted OH and the measured OH^* chemiluminescence are found in the secondary reaction zone. This implies a time delay or phase shift between Q_{tot} and OH^*. It also suggests that only small amounts of the OH are consumed in the initiation of the fuel oxidation and slowly recombine to form the combustion products.

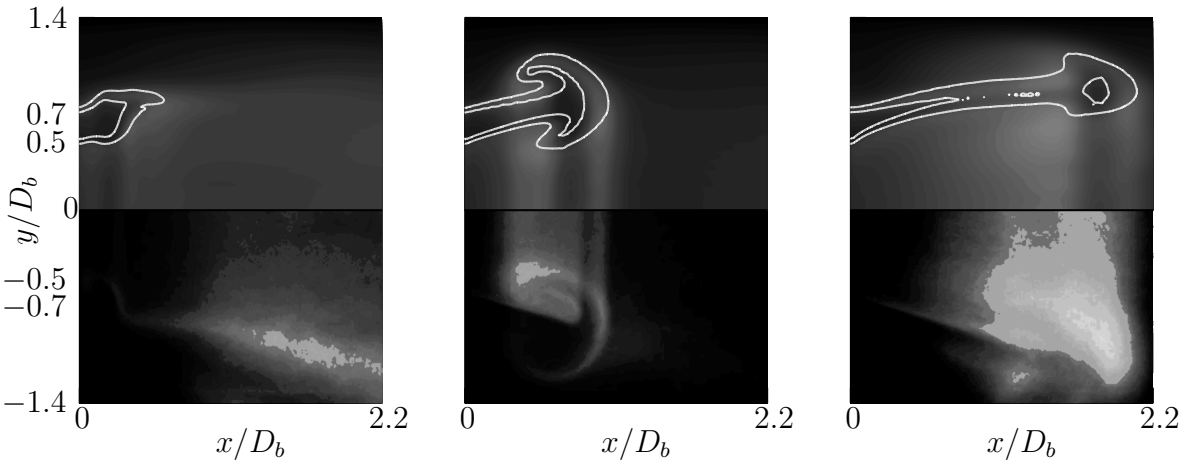

(a) $\gamma = 0.0$ (b) $\gamma = 0.3$ (c) $\gamma = 0.6$

Figure 3.18.: Line-of-sight integration of the predicted OH mass fraction field (*upper half*) and the OH^* chemiluminescence measurements of Balachandran [7] (*lower half*) in the median plane of the combustion chamber. The white contour represents the extent of the flame layer.

Improved estimates for the heat release rate were recently proposed by Nikolaou and Swaminathan [73]. The authors simulated flames in mixtures of methane, $\mathrm{CH_4}$, and air and found that for lean to stoichiometric conditions the rates of the reactions

$$\mathrm{H} + \mathrm{CH_2O} \rightleftharpoons \mathrm{HCO} + \mathrm{H_2} \ , \tag{3.1}$$

$$\mathrm{O} + \mathrm{CH_4} \rightleftharpoons \mathrm{OH} + \mathrm{CH_3} \ , \tag{3.2}$$

correlate better with the heat release rate than the frequently employed product of c_{OH} and $c_{\mathrm{CH_2O}}$. The reactions (3.1) and (3.2) also apply when the fluid motion is turbulent. For laminar flow, the rates of

$$\mathrm{H} + \mathrm{HO_2} \rightleftharpoons \mathrm{O_2} + \mathrm{H_2} \ , \tag{3.3}$$

$$\mathrm{H} + \mathrm{HO_2} \rightleftharpoons \mathrm{O} + \mathrm{H_2O} \ , \tag{3.4}$$

$$\mathrm{H} + \mathrm{HO_2} \rightleftharpoons 2\mathrm{OH} \ . \tag{3.5}$$

are found to correlate strongly with the heat release rate. Chemical markers for the heat release rate can then be obtained by estimating the forward rates of (3.1)-(3.5), which are proportional to the products of c_{H} and $c_{\mathrm{CH_2O}}$, c_{O} and $c_{\mathrm{CH_4}}$, and c_{H} and $c_{\mathrm{HO_2}}$, respectively. Gazi *et al.* [43] suggested that CH_2O based markers are valid only when the major pathway of the fuel oxidation proceeds along reactions which involve the methyl radical, CH_3. The authors also identified the product of the mass fractions of molecular oxygen, $c_{\mathrm{O_2}}$, and the ketenyl radical, c_{HCCO}, as an adequate marker for the heat release rate in fuel-rich ethylene-air flames. All these markers are plotted in Figure 3.19 as integral values of the planar mass fraction profiles. It appears that the product of $c_{\mathrm{O_2}}$ and c_{HCCO} correlates best with Q_{tot} in the flow configuration investigated here. Both the amplitude and phase of Q_{tot} are well reproduced. On the other hand, the markers $c_{\mathrm{OH}}c_{\mathrm{CH_2O}}$, $c_{\mathrm{H}}c_{\mathrm{CH_2O}}$, and $c_{\mathrm{O}}c_{\mathrm{CH_4}}$ all have a maximum value at $\gamma \approx 0.7$ which is approximately 30 % higher than that of the predicted Q_{tot}. Although the phase angle is better predicted by the product of c_{H} and $c_{\mathrm{HO_2}}$, the overprediction of Q_{tot} at $\gamma \approx 0.7$ remains.

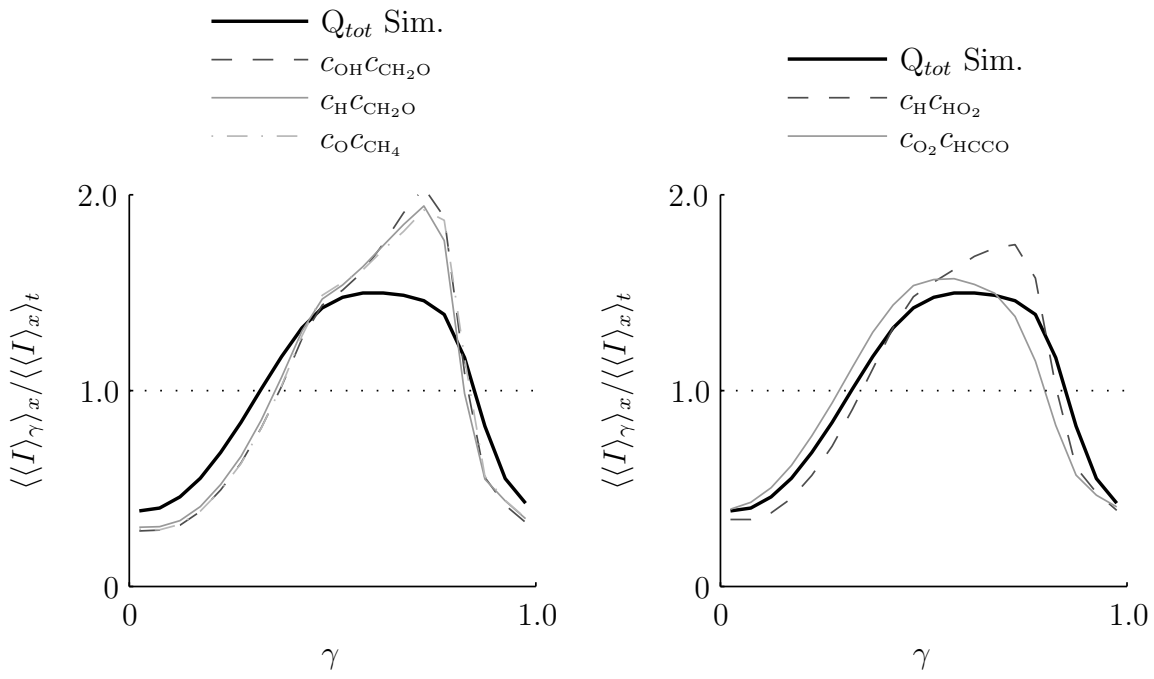

Figure 3.19.: Chemical markers to quantify the variation of Q_{tot}. The markers are integral values of the mass fraction profiles in the median plane of the combustion chamber.

Reliable fluorescence imaging techniques already exist for the determination of the mole fraction of molecular oxygen, see [28, 44]. Brock *et al.* [17] have developed laser-induced fluorescence spectroscopy of the ketenyl radical. This enables the experimentalist to determine the product of $c_{\mathrm{O_2}}$ and c_{HCCO} and test its application in similar flame configurations. It has to be acknowledged that the present findings may not apply to other flame configurations since the major chemical pathway for the fuel oxidation and hence the chemical reactions correlating well with the total heat release rate depend on many parameters, including the type of fuel and the equivalence ratio.

3.5. Conclusions

The modelling approach outlined in the present chapter is able to reproduce the measured first and second moments of the non-oscillating and oscillating cold flow velocity field with reasonable accuracy. In the reacting case, the flame position and non-linear evolution of the total heat release rate as a function of phase angle are well predicted. However, the flame-wall interaction could not be resolved in the simulation, which is likely the result of the boundary treatment neglecting the heat transfer at the wall. The predicted results suggest a time lag of approximately 20 % of the time period associated with the frequency of the excitation signal between the measured OH^* chemiluminescence and the predicted total heat release rate. Large amounts of the predicted OH mass fraction as well as the measured OH^* chemiluminescence are found in the secondary reaction zone. A possible explanation is that the OH slowly recombines to the combustion products, resulting in a large extent of the secondary reaction zone. The majority of the heat of reaction is released further upstream in the primary reaction zone implying a time lag between the bulk formation of OH and the total heat release rate. A chemical marker for the total heat release rate with better phase correlation than the usual formaldehyde based markers is the product of the mass fractions of molecular oxygen and the ketenyl radical. These findings apply first and foremost in the investigated experiment but may also prove useful in similar flame configurations. Reliable experimental techniques already exist to determine the mass fractions of molecular oxygen and the ketenyl radical to verify the findings of the present work.

4. Self-Excited Flame Oscillation

4.1. Introductory Remarks

The results presented in the preceding chapter have shown that the Large Eddy Simulation (LES) technique in conjunction with the Probability Density Function (PDF) approach to account for the unresolved turbulence-chemistry interaction is capable of capturing the main characteristics of the oscillating flame. While the previous chapter describes the modelling approach taken to simulate forced flame oscillation, the present chapter reports the simulation of a weakly self-excited flame oscillation in an industrial combustion chamber with complex geometry. The specific objective is to investigate whether or not the LES-PDF method is able to predict the weak longitudinal flame oscillation observed in the experiment.

The test case chosen for study is an experiment by Stopper *et al.* [92] investigating the mixture kinematics in the Siemens SGT-100 combustion chamber. Stopper *et al.* carried out extensive measurements of the flow field, species concentrations, and temperature for two operating pressures, namely 3 bar and 6 bar. The measurements provide a reliable and comprehensive reference data base for comparison with the simulation results.

Both at 3 bar and 6 bar operating pressure a weak flame oscillation is observed, yet appears more pronounced at the 6 bar condition. The investigation presented in the following focuses solely on the 6 bar condition. Bulat [19] has simulated and thoroughly investigated the flow field at the 3 bar operating pressure using the LES-PDF method and found excellent agreement between the measurements and the simulation results. This lays an encouraging basis for using the LES-PDF method in the simulation of the flow at the 6 bar condition.

The present chapter is organised as follows. Details of the experiment are presented in the next section. Section 4.3 describes the modelling approach taken to simulate the flow. The results obtained from the simulation are presented and discussed in section 4.4. Section 4.5 provides the conclusions.

4.2. Experiment

The experiment described in the following was carried out by Stopper [91]. A diagram of the combustion chamber together with its dimensions is presented in Figure 4.1. Fuel and oxidiser streams are injected separately into the swirler device upstream of the combustion chamber and allowed to mix in the pre-chamber before entering the combustion chamber. The swirler has 12 rectangular channels and three small holes per channel for the fuel injection with German natural gas. The composition of the fuel is given in Table 4.1. The combustion chamber has an octagonal cross section with four small corner and four 4 wide faces which are made of quartz glass to enable optical access for the laser diagnostics. The four large windows, in fact, consist of two thick parallel quartz glass plates with a small gap between them to allow for cooling. In this way stable temperature conditions

are maintained at the windows. After passing the gap between the quartz glass plates the cooling air is diverted into the swirler. A conical transition duct connects the combustion chamber with the exhaust pipe to cool down the hot exhaust gases. The exhaust cooling pipe has a length of 20 D_e and a diameter of 2 D_e, where $D_e = 50$ mm is the diameter of the combustor outlet. D_e is here employed as a reference length for non-dimensionalising the results in the remainder of this chapter. The operating pressure is controlled by an orifice plate positioned at the downstream end of the exhaust cooling pipe.

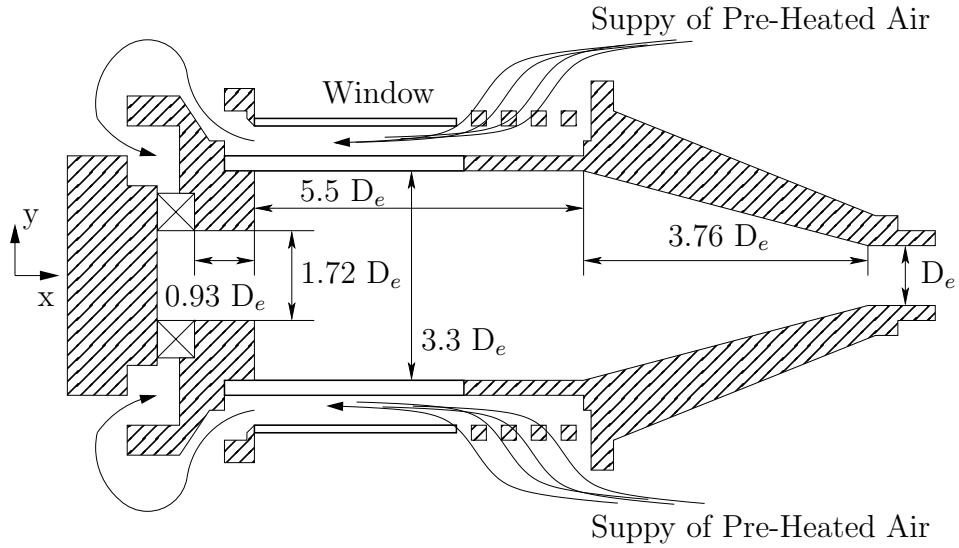

Figure 4.1.: Combustion chamber in the experiment of Stopper [91] (not to scale). The reference dimension is $D_e = 50$ mm.

The flow conditions for the case investigated here are listed in Table 4.2. The bulk inflow velocity, $v_{in} = 40.4$ m/s, is used as a reference in the remainder of this chapter to non-dimensionalise the predicted results. The velocity vector components in the median plane of the combustion chamber are determined by Particle Image Velocimetry. Temperature and species mass fractions are measured at a number of discrete points with one-dimensional laser Raman scattering. OH planar laser-induced fluorescence is employed to visualise the position and the spatial extent of the flame. Chemiluminescence of OH^* is additionally measured to determine the flame lift-off height. To obtain information on the dynamic response of the pressure an acoustic microphone is mounted at one end of a steel pipe which is connected with a pressure tab at the combustor wall. The effect of the pipe acoustics on the pressure measurements is not considered in the calibration of the microphone. Hence, the pressure measurements must be regarded with caution [91].

Table 4.1.: German natural gas fuel composition. Source Stopper *et al.* [92].

Molecular species	Mole fraction [-]
Carbon Dioxide (CO_2)	0.0041
Nitrogen (N_2)	0.0133
Ethane (C_2H_6)	0.0166
Methane (CH_4)	0.9660

Stopper [91] has reported about mass flow leakage effects along the path of the air

supply to the swirler inlet, especially at the connection between the side wall quartz glass panels and the metal wall. As a result, the mass flow rate in the gap between the two quartz glass panels was reduced by 8.6 %. Leakage into the combustion chamber was also identified at the corner connection between the front panel and the windows, which reduced the remaining mass flow rate into the swirler by approximately 8.8 %. No measurements of the velocity field were taken at the exit of the combustion chamber. However, STOPPER *et al.* reported about leakage along the exhaust cooling pipe which lowered the mass flow rate entering the exhaust cooling pipe by approximately 12 %.

Table 4.2.: Investigated experimental conditions. The Reynolds number is based on the distance between the inner wall of the pre-chamber and the inner shear layer of the averaged flow field at the exit of the pre-chamber, the bulk inflow velocity and the kinematic viscosity of the inflowing mixture. Source: STOPPER *et al.* [92].

	Unit	Value
Operating pressure	[bar]	6
Reynolds number	[-]	78,000
Geometric swirl number	[-]	1.3
Air temperature	[K]	677
Fuel-air equivalence ratio	[-]	0.6
Total air mass flow rate	[kg/s]	0.352
Total fuel mass flow rate	[kg/s]	0.0125
Bulk inflow velocity, v_{in}	[m/s]	40.4
Total heat release rate	[kW]	685

4.3. Simulation Details

Physical Model

The fluid motion is modelled using the field equations presented in section 1.4. Two treatments of the mixture kinematics are considered. In the first case, referred to as LESi in the remainder, the mixture is assumed incompressible. In the second case, referred to as LESc in the remainder, the mixture is assumed compressible. Both simulations are carried out with the same flow solver BOFFIN, *c.f.* section B.5. It is clear from the outset that LESi is not able to capture the self-excited flame oscillation observed in the experiment. LESi is used as a reference case to compare the time-averaged results with those of LESc.

The heat capacities of the constituents are computed using JANAF polynomials. The mixture viscosity is calculated by employing the empirical formula of WILKE, see [79]. Just as in the previous case, *c.f.* section 3.3, the material coefficients are assumed to yield constant and equal SCHMIDT numbers, which are also equal to the PRANDTL number. Since the major component of the fuel is methane (*c.f.* Table 4.1), the detailed but reduced reaction mechanism for methane oxidation by SUNG *et al.* [93] is employed. This reaction mechanism comprises 15 elementary reactions and 19 chemical species.

Computational Domain

The computational domain, block decomposition and applied boundary conditions are presented in Figure 4.2. The domain comprises the swirler, pre-chamber, combustion chamber, transition duct and the exit of the combustion chamber. All the details of the swirler are represented in the computational domain, including the 12 rectangular channels, and the base holes for the fuel injection. The whole domain is decomposed into 240 blocks.

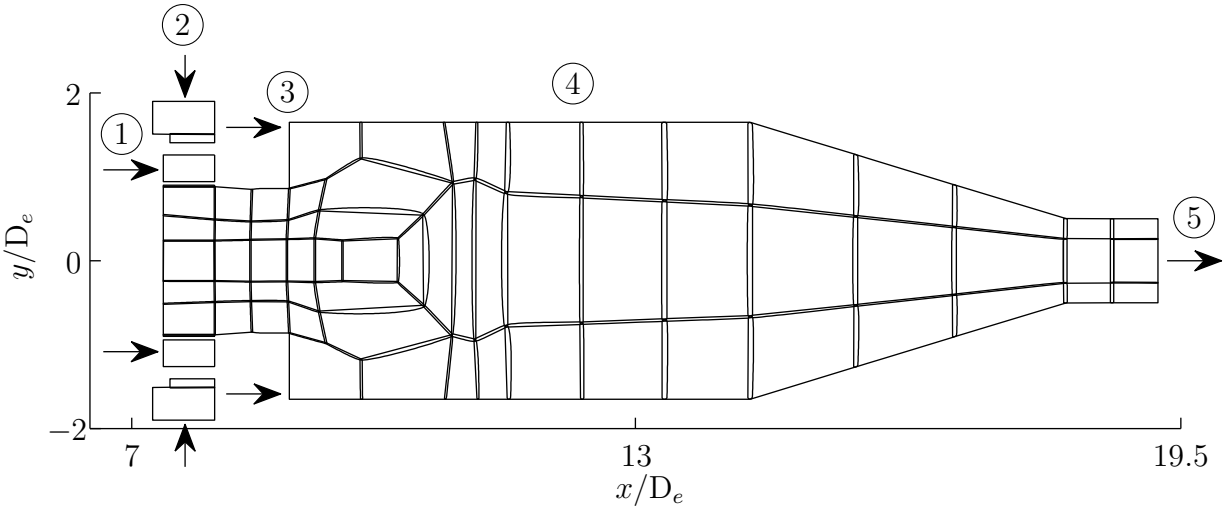

Figure 4.2.: Sketch of the computational domain and boundary conditions (to scale). The boundary conditions are as follows: 1: *base hole fuel injection*, 2: *air inlet*, 3: *panel leakage air inlet*, 4: *combustor wall*, 5: *outlet*.

The exhaust cooling pipe is not considered here. It should be remarked at this point that the omission of the exhaust cooling pipe in the computational domain may have critical effect on the acoustic response of the burner system. The conditions at the axial boundaries imply that the dominant frequency of the acoustic response in the exhaust cooling pipe is the quarter-wave mode, which has an estimated value of 212 Hz. This frequency value is very close to the experimentally determined frequency 216 Hz in the pressure spectrum, suggesting that the acoustics of the exhaust cooling pipe could be responsible for the flame oscillation. Yet even without the exhaust cooling pipe the computational demand for resolving the flow in the combustion chamber is very high. On this basis it was decided to first leave out the exhaust cooling pipe in the computational domain, but this should be reconsidered in future investigations.

The block-structured grid was generated by Bulat [19] with the commercial software package ICEM CFD Hexa and contains approximately 8 million grid cells which are clustered in the swirler, pre-chamber and near the inlet of the combustion chamber. Bulat has refined and improved the grid several times to decrease the aspect ratio of the grid cells, and achieved excellent results in the 3 bar case. Figure 4.3 shows slices of the grid in the x-y and y-z planes. The global minimum and maximum grid spacings in each coordinate direction are listed in Table 4.3. The grid cells with the smallest and largest dimensions are located in the swirler channels and the combustion chamber, respectively. In order to limit commutation errors in the LES the grid cell size varies smoothly in the computational domain.

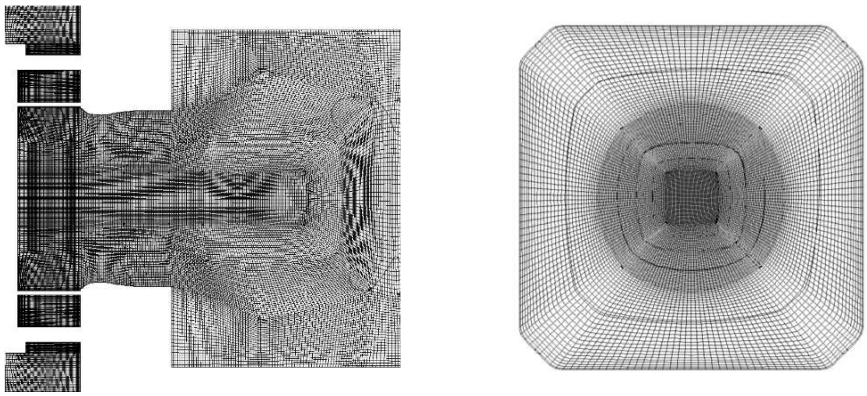

(a) $x - y$ plane (b) $y - z$ plane

Figure 4.3.: Computational grid.

Table 4.3.: Minimum and maximum grid spacing. Source Bulat [19].

	Value [mm]
Δx_{min}	0.281
Δx_{max}	4.160
Δy_{min}	0.086
Δy_{max}	5.240
Δz_{min}	0.083
Δz_{max}	5.330

Boundary Conditions

In both simulations LESi and LESc, boundary-normal uniform velocities are prescribed at all inlet boundaries. The values of the inlet velocities are evaluated using the experimentally determined mass flow rates. The panel leakage air inlet is prescribed as a three-cell wide perimeter at the front panel of the combustion chamber. The pressure at the inlet boundaries is extrapolated from the interior and may induce a drift in the required target mass flow rates in the simulation LESc. To avoid any significant deviation from the target mass flow rates in LESc, the inlet velocities are rescaled at every time step by computing the instantaneous mass flow rates and re-scaling with the target mass flow rates. Hence, the inlet boundaries are fully reflecting with regard to the propagation of acoustic waves across the boundaries in the simulation LESc. This type of boundary treatment excludes equivalence ratio variations due to upstream propagating pressure waves modulating the inwards directed mass flow rates as a possible mechanism for sustained flame oscillation. To define uniform velocities at the inlet is in contradiction with LES, since LES assumes turbulent flow. However, the initially uniform flow at the inlet boundary in the critical swirler region evolves quickly into a turbulent flow as a result of the complex geometry of the swirler. The fuel injection through the holes in the swirler vanes is achieved by identifying the boundary grid cells which belong to each fuel injection hole. Each hole is resolved by a minimum of nine boundary cells [19].

At the outflow boundary, LESi employs zero gradient Neumann boundary conditions. In the case of LESc, the definition of the outflow conditions is more difficult because the static pressure must be specified. This is complicated by the fact that the fluid is still

in swirling motion at the outflow boundary inducing a pressure variation in the radial direction. This problem is not removed by just extending the computational domain and taking the exhaust cooling pipe into account because the swirl strength decays only slowly in the pipe. Hence, the fluid is still in swirling motion at the exit of the exhaust cooling pipe and the same problem is faced with regard to the definition of appropriate boundary conditions. The velocity components in the median plane of the combustion chamber measured in the experiment and predicted by LESi suggest that the flow remains subsonic throughout the combustion chamber. The flow at the exit of the combustion chamber is not choked, which necessitates consideration of the wave propagation across the boundary. This led to the application of Yoo and Im [109]'s characteristic boundary conditions for compressible, reacting mixtures. Yoo and Im's boundary conditions are based on the hyperbolic form of the field equations for compressible Euler fluids. Additional terms are introduced in order to account for shearing flow and chemical reactions at the boundary, which is of particular importance when the pressure field is influenced by the swirling motion of the fluid. The boundary conditions are implemented into BOFFIN and validated using the test cases presented by Yoo and Im [109]. However, when applied in the present case, the pressure experiences a continuous drift from the specified far field pressure and eventually the simulation becomes unstable. Various values of the reflection parameter were tested leading to the same outcome. It was therefore decided to use a different approach and apply the pressure field of a two-dimensional steady vortex at the outflow boundary

$$\pi = \pi_\infty - \rho \frac{C^2}{R_c^2} \exp\left[-\frac{(y-y_0)^2 + (z-z_0)^2}{2R_c^2} \right], \tag{4.1}$$

where C, R_c, and π_∞ are the vortex strength, the vortex radius and the far field pressure. The far field pressure is set equal to the operating pressure 6 bar. The above pressure field (4.1) is the potential flow solution of a steady vortex in an incompressible, inviscid fluid. Viscosity effects at the boundary can be neglected due to the high Reynolds number. The LESi results show that the vortex strength varies only marginally about the time-averaged mean value which lends justification for the use of a steady flow approximation. The vortex strength and vortex radius are estimated from the time-averaged velocity vector predicted by LESi. By assuming a pressure profile of the form (4.1), acoustic wave propagation across the boundary cannot be accounted for. Pressure waves incident upon the boundary from the interior of the domain will be fully reflected at the boundary. It is clear that this boundary condition is too strong of an idealisation and adversely affects the acoustic field prediction in the combustion chamber, but is necessary to preserve numerical stability.

The combustor walls are in both simulations LESi and LESc assumed to be adiabatic since the heat release rate is much larger than the heat flux at the boundary. In addition, the flame is aerodynamically stabilised in the shear layers and hence not in contact with the wall. The near-wall turbulence is not resolved but accounted for by wall functions based on the Grötzbach-Schumann equation [26].

Computational Cost

The simulations are carried out on 30 computing nodes, where each node comprises two 2.5 GHz Quad core Intel Xeon processors. The nodes are connected with InfiniBand, which enables high transfer rates between the nodes. Some important simulation parameters are listed in Table 4.4.

Table 4.4.: Simulation Parameters.

	LESi	LESc
Time step size [s]	$5.0 \cdot 10^{-7}$	$1.0 \cdot 10^{-7}$
Averaging time [ms]	32	8
# Stochastic fields	8	8
# MPI processes	240	240
# Time steps	400,000	500,000
Running time [d]	230	190

A constant time step is employed to facilitate the frequency analysis of time histories recorded at probe locations in the combustion chamber. With the time step listed in Table 4.4 the maximum COURANT number in the simulation LESi is 0.35. In the case LESc the COURANT number associated with the maximum speed at which information is propagated in the mixture is approximately two orders of magnitude higher than that of LESi. The time step in LESc is too large to resolve appropriately the propagation of the smallest acoustic waves in the combustion chamber, but ensures numerical stability. The time step was chosen in light of the significant computational demand and the required minimum time period to be resolved in order to obtain reliable time-averaged statistics. Yet the averaging time in the case LESc is still too short to obtain fully converged statistical results, which was solely due to limited computational resources. On average the number of iterations to solve for the pressure correction equation in LESi is two orders of magnitude higher than in the case LESc, which leads to a decreased wall clock time per time step in LESc. In both cases the largest amount of time is spent on the integration of the numerically stiff chemical source terms despite the parallelisation used in solving for the chemical source terms. Consequently, the computational speed up gained in LESc due to fewer number of iterations in the pressure solving is severely limited by the source step calculation.

4.4. Results and Discussion

Time-Averaged Results

The field variables of LESi are initialised using the fully developed flow field results of BULAT [19] at the 3 bar operating pressure. This was done to avoid resolving the costly ignition period. Before collecting the statistics, a time period of 40 ms was resolved to let the flow attain a fully developed stage. In the case of LESc, the mixture is initialised as hot air at a temperature of 2,200 K. The simulation was first run without the fuel injection until the pre-heated, but cooler air from the swirler inlet has filled the swirler vanes and entered the pre-chamber. Then, the fuel was injected through the holes in

the swirler vanes which led to mixing with the oxidiser in the pre-chamber establishing the flame through auto-ignition. To speed up the computation, the ignition phase in LESc is resolved without taking account of the costly sub-filter turbulence-chemistry interaction modelled by means of the PDF approach. The PDF approach is only applied after completion of the ignition phase. Time-averaged quantities and fluctuations about the time average are denoted by $\langle\cdot\rangle_t$ and a double prime, respectively.

The resulting time-averaged flow patterns of LESi and LESc are shown in Figure 4.4 (a) and (c), respectively.

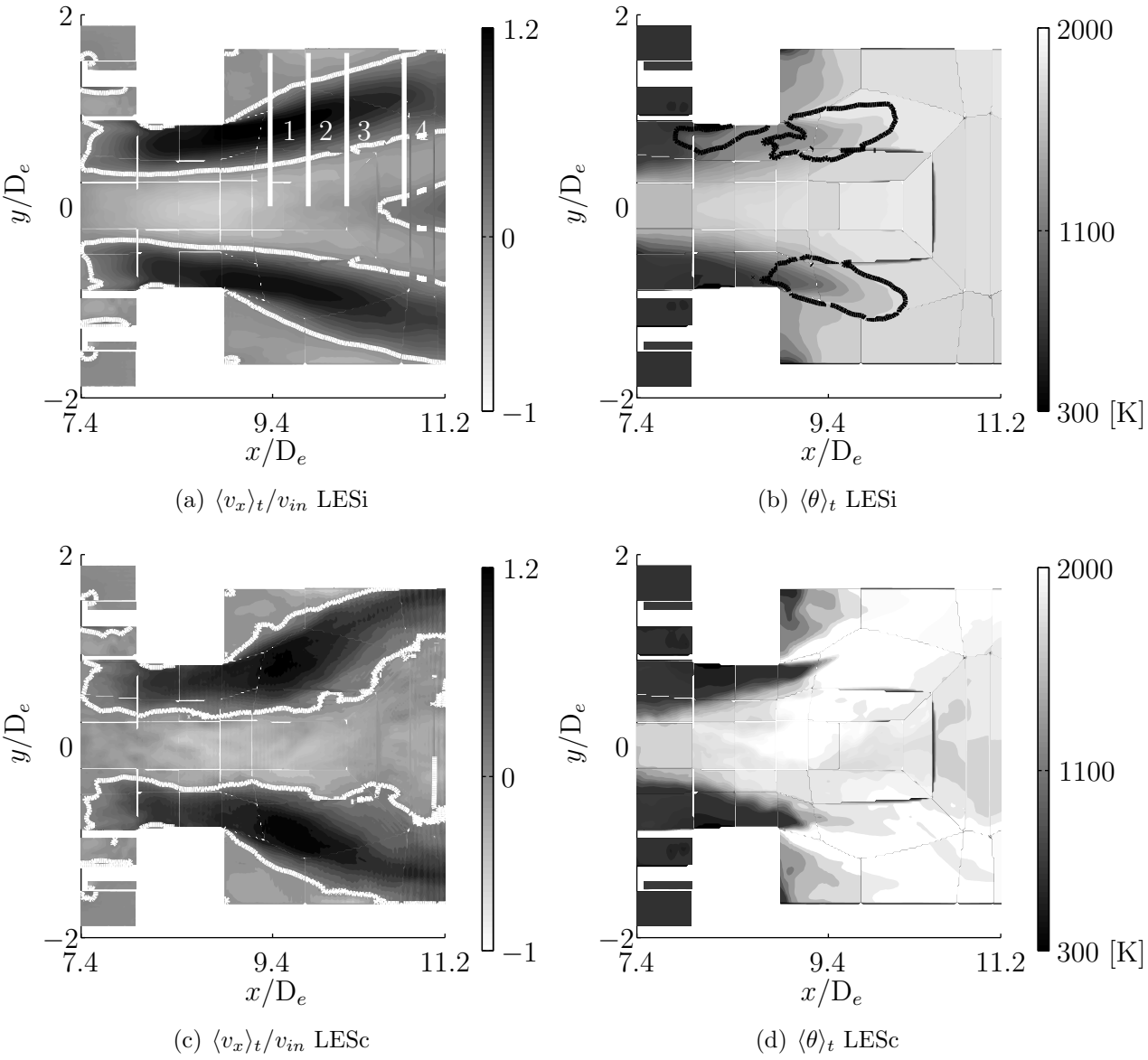

(a) $\langle v_x\rangle_t/v_{in}$ LESi

(b) $\langle\theta\rangle_t$ LESi

(c) $\langle v_x\rangle_t/v_{in}$ LESc

(d) $\langle\theta\rangle_t$ LESc

Figure 4.4.: Time-averaged results in the median plane of the combustion chamber. v_{in} has a value of 40.4 m/s. The numbered lines in (a) mark the axial stations at which the RAMAN measurements were taken. The white thick lines in (a) and (c) represent the contour with zero axial velocity. The black line in (b) represents the contour of the heat release rate at 15 % of the maximum heat release rate.

Both simulations show the formation of a swirling jet in the pre-chamber which expands radially when entering the combustion chamber. Further downstream, the swirling jet becomes unstable generating a vortex bubble on the centre axis of the combustion chamber. This results in the reversal of the flow direction in the central region of the pre-chamber, which is referred to as Central Recirculation Zone (CRZ) in the remainder. Consequently, a free stagnation point exists on the centre axis. Downstream of the free stagnation point along the centre axis forms a vortex which extends to the exit of the combustion chamber. This vortex is referred to as Central Vortex Core (CVC), *c.f.* Bulat [19]. The presence of the CVC at the exit of the combustion chamber complicates the imposition of appropriate boundary conditions for the static pressure, as was addressed in the discussion of the boundary conditions. The dimensions of the CRZ are visualised by means of the zero contour of the axial velocity in Figure 4.4 (a) and (c). LESi and LESc both suggest that the CRZ extends to the front panel of the combustion chamber. In addition, a recirculation zone is generated in the outer region of the combustion chamber, subsequently referred to as Outer Recirculation Zone (ORZ). The flow pattern at 6 bar operating pressure is qualitatively the same as in the 3 bar case, see [19, 20].

The flame is aerodynamically stabilised in the shear layer between the CRZ and the swirling jet, as can be concluded from the black contour of the heat release rate in Figure 4.4 (b). Both the heat release rate contour and temperature profile in Figure 4.4 (b) predicted by LESi also suggest burning inside the pre-chamber, which was not observed in the experiment. In the course of the simulation, it was noticed that the flame tip first stabilised at the corner of the pre-chamber exit, then left its anchoring position and propagated upstream into the pre-chamber finally stabilising in the shear layer of the small recirculation zone at the wall. The reason for this flame tip propagation is suspected to be due to a non-recurring lateral movement of the swirling jet connecting temporarily the ORZ with the near-wall recirculation zone in the pre-chamber. This flame tip propagation was, however, not observed in the simulation LESc. By comparing the temperature distribution of LESi [Figure 4.4 (b)] with LESc [Figure 4.4 (d)] it becomes clear that the temperature in the central part of the combustion chamber is approximately 200 K higher in the case LESc. This significant temperature difference is likely the result of different flame characteristics in the case LESc and not connected with the relatively short averaging time in LESc. The high temperatures in LESc were observed early on in the simulation. Differences between the results of LESi and LESc, and the measurements are now analysed in more detail by comparing the transverse profiles at the four axial stations highlighted in Figure 4.4 (a).

Figure 4.5 compares the profiles of the axial velocity. Both simulations are able to reproduce the measurements at all axial stations. However, LESc overestimates the lateral dimension of the annular swirling jet by approximately 20 % at X_1 near the inlet of the combustion chamber, but predicts the peak velocities better. Both simulations show good agreement with the measurements in the CRZ ($-0.5 \leq y/\mathrm{D}_e \leq 0.5$). Further downstream at X_2, LESi overpredicts the peak velocities by approximately 25 %. The results of LESc are in better agreement with the measurements both in terms of the lateral dimension and the mean radial position of the swirling jet. The slight asymmetry observed in the LESi profile at X_2 is likely an effect of the flame flash back into the pre-chamber observed in Figure 4.4 (b). Further downstream, at X_3 and X_4, LESc predicts the minimum velocity in the CRZ generally better than LESi. The reversal of the flow direction on the centre axis between the axial stations X_3 and X_4 implies that the time-averaged mean free stagnation point is located between these two axial stations in LESi. Consequently, the

axial extent of the CVC is overestimated by LESi.

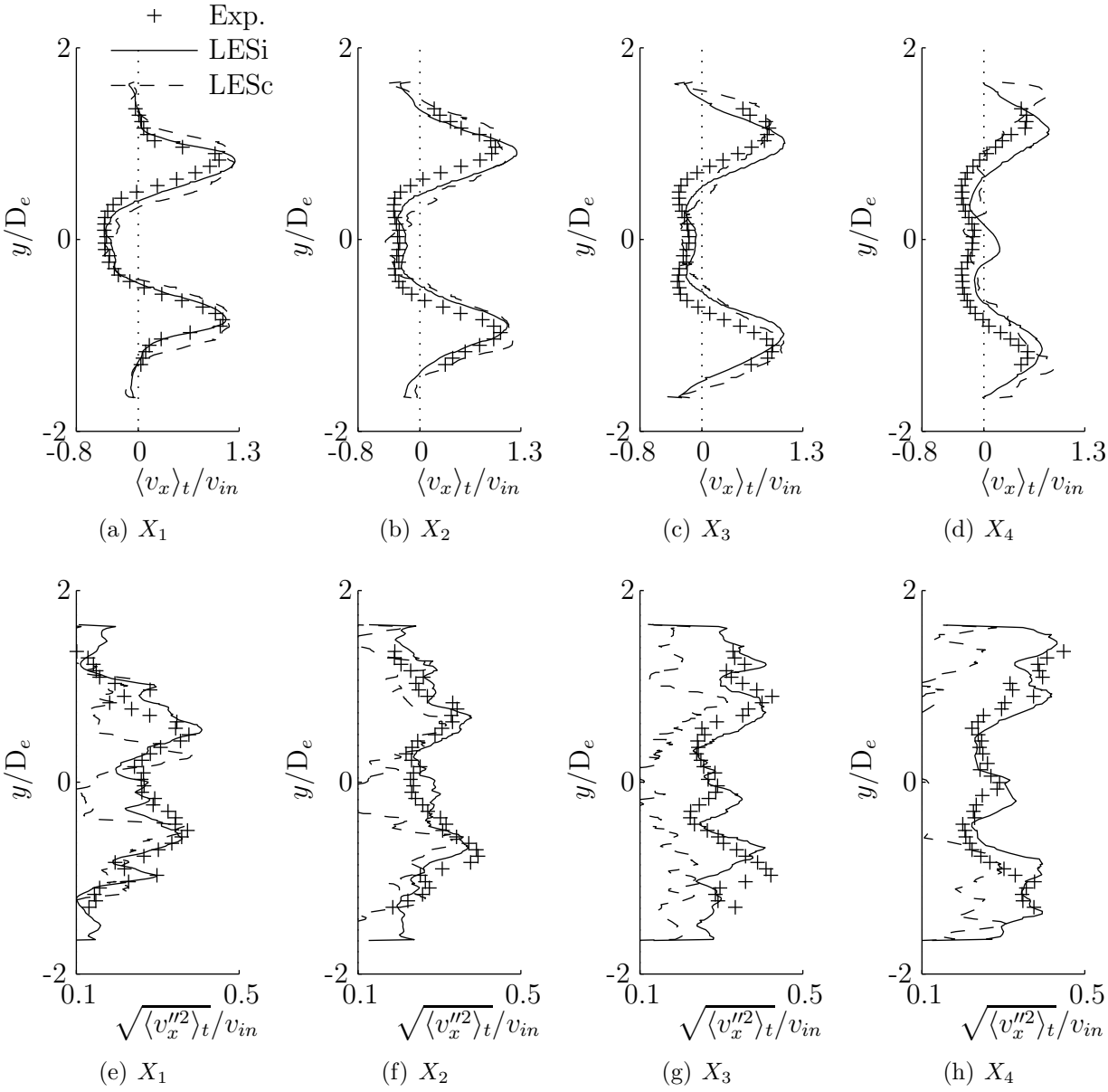

(a) X_1 (b) X_2 (c) X_3 (d) X_4

(e) X_1 (f) X_2 (g) X_3 (h) X_4

Figure 4.5.: Transverse profiles of axial velocity statistics, symbols: experiment [92], solid lines: simulation; (a)-(d) time-averaged mean, (e)-(h) root-mean-square.

The root-mean-square of the turbulent fluctuations predicted by LESi are at all axial stations in excellent agreement with the measurements, *c.f.* Figure 4.5 (e)-(h). The LESc results, on the other hand, are not converged due to an insufficient averaging time and show large deviations from the measurements, especially in the CRZ where the velocities and the convergence rate of the statistics are low. The measurements as well as the LESi results show two peaks at the edges of the swirling jet, which are associated with the inner and outer shear layer of the swirling jet. The inner shear layer is more pronounced than the outer shear layer.

Statistical results for the radial velocity are presented in Figure 4.6. It can be seen that both simulations overpredict the measured mean radial velocity at all axial stations. The results of LESc tend to agree closer with the measurements throughout, especially at

X_4. The trends at X_1 and X_2 are qualitatively reproduced by the simulations, showing peak velocities in the swirling jet. However, the mean radial velocities in the swirling jet predicted by LESi decay too slowly along the axial direction. In fact, the edge values of the predicted linear profile across the centre axis appear to increase along the axial direction towards the exit of the combustor. This again suggests that the CVC predicted by LESi is too pronounced in comparison to the measurements. The agreement between the measured and predicted turbulence levels is less satisfactory than in the previous case of the axial velocities, *c.f.* Figure 4.5.

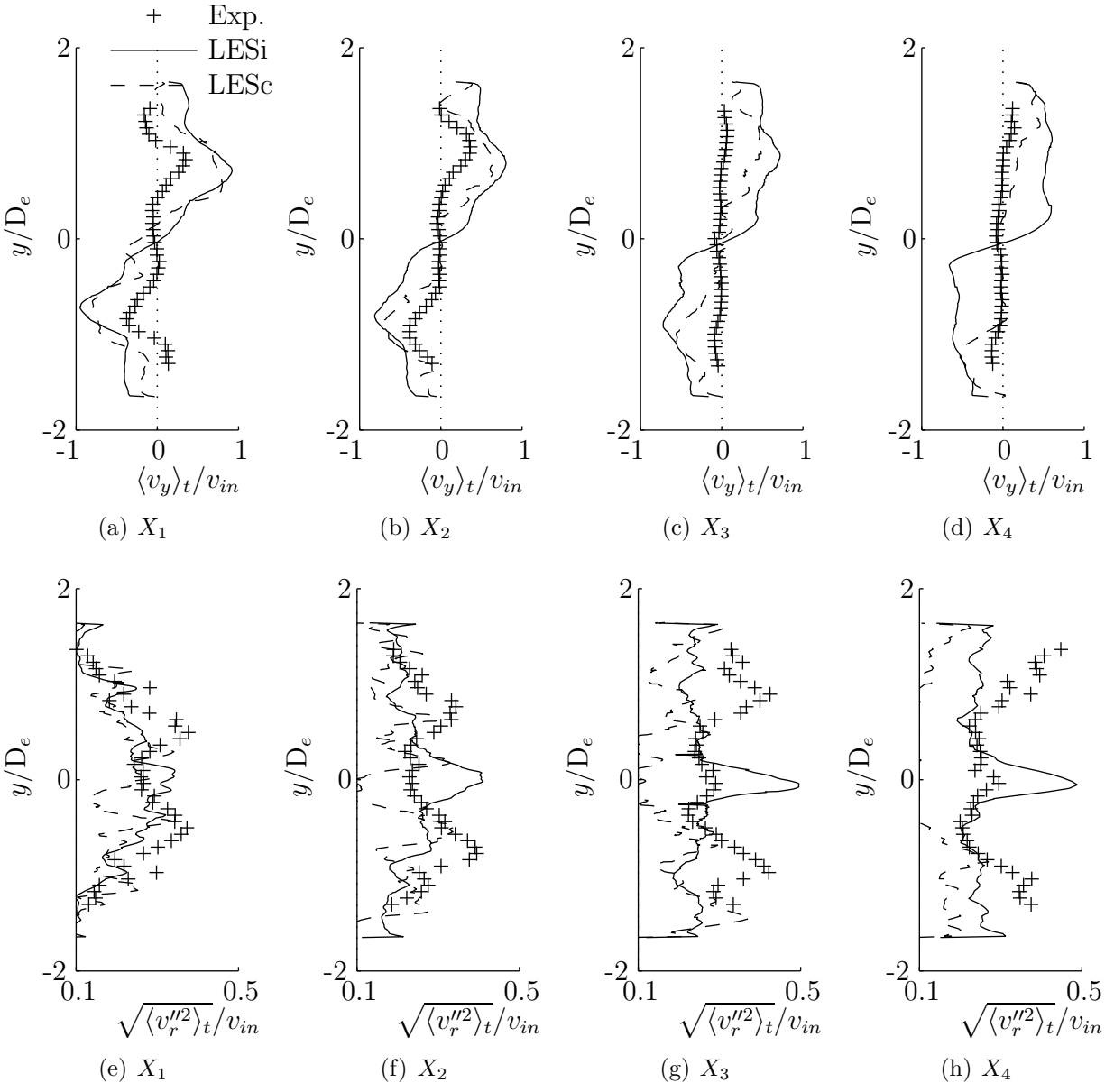

Figure 4.6.: Transverse profiles of radial velocity statistics, symbols: experiment [92], solid lines: simulation; (a)-(d) time-averaged mean, (e)-(h) root-mean-square.

Acceptable agreement is only achieved at the axial station nearest to the inlet of the combustor, namely X_1. Further downstream, the LESi results show a significant deviation from the measurements near the centre axis. The turbulence levels in the CRZ and CVC are overpredicted by up to 60 %, while in the swirling jet they are underpredicted

by approximately 40 % and remain flat. Both simulations are not able to reproduce qualitatively the trends at the axial stations $X_2 - X_4$. LESi clearly overestimates the axial extent and turbulence levels of the CVC. This appears unlikely to stem from the applied NEUMANN boundary conditions at the exit of the combustion chamber. Instead, compressibility effects likely influence the swirl induced momentum transfer in the CVC near the exit of the combustor, which can be concluded from the MACH contours presented in Figure 4.7. MAYER AND POWELL [68] have studied similarity solutions for compressible viscous vortex cores and found that, as the MACH number rises, the slope of the swirl velocity near the axis of rotation decreases. In addition, the authors showed that the axial velocity in the core region becomes less pronounced as the MACH number increases and flattens out, which is consistent with the results obtained in the present case.

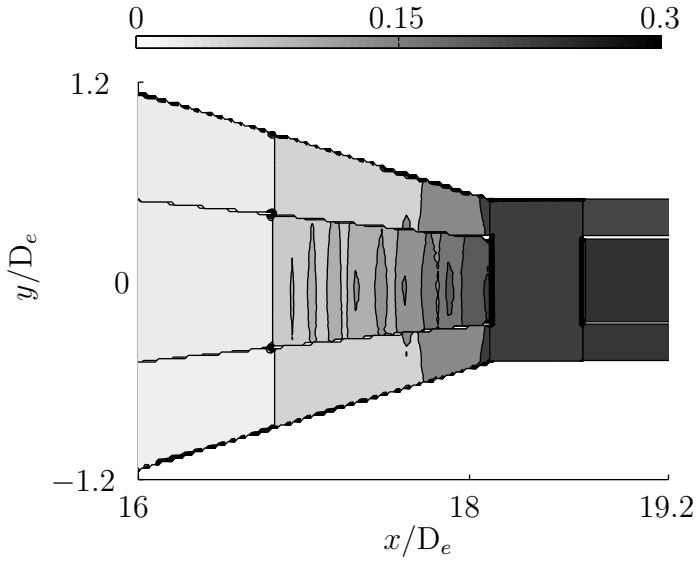

Figure 4.7.: Time-averaged MACH contours predicted by LESc near the exit of the combustor.

A comparison between the predicted and measured temperature profiles is shown in Figure 4.8. LESi is able to reproduce the temperature in the CRZ with good accuracy. Larger deviations between LESi and the measurements are observed only in the swirling jet where the temperature is overpredicted by approximately 60 %. This seems likely to be the result of an upstream shift of the flame position. The cause of this flame shift could not be identified satisfactorily, but may be connected with a slight difference between the actual experimental and numerically imposed fuel mass flow rates. Another source of error could be the reaction mechanism applied in the simulation leading to an overestimation of the fuel consumption rate. The asymmetry in the temperature profiles is the result of the flame flash back into the pre-chamber. On the other hand, LESc overestimates the temperature at all axial stations and across the transverse direction. The highest temperatures are found in the outer shear layer consistent with the LESi results, but they exceed the LESi results by approximately 25 %. A local increase of the flame speed in LESc due to pressure values below the operating pressure are unlikely to produce an observable upstream shift of the flame position which could explain the difference in the temperature predictions. It is expected that the flow fields predicted by LESi and LESc behave very similar in the pre-chamber and near the combustor inlet, since the MACH number is very low in this region. It is conceivable that the reduction of the numerical

time step in LESc leads to larger stochastic velocities which induce in turn larger errors in the local mixture composition directly affecting the flame characteristics and hence the mixture temperature on the burnt side.

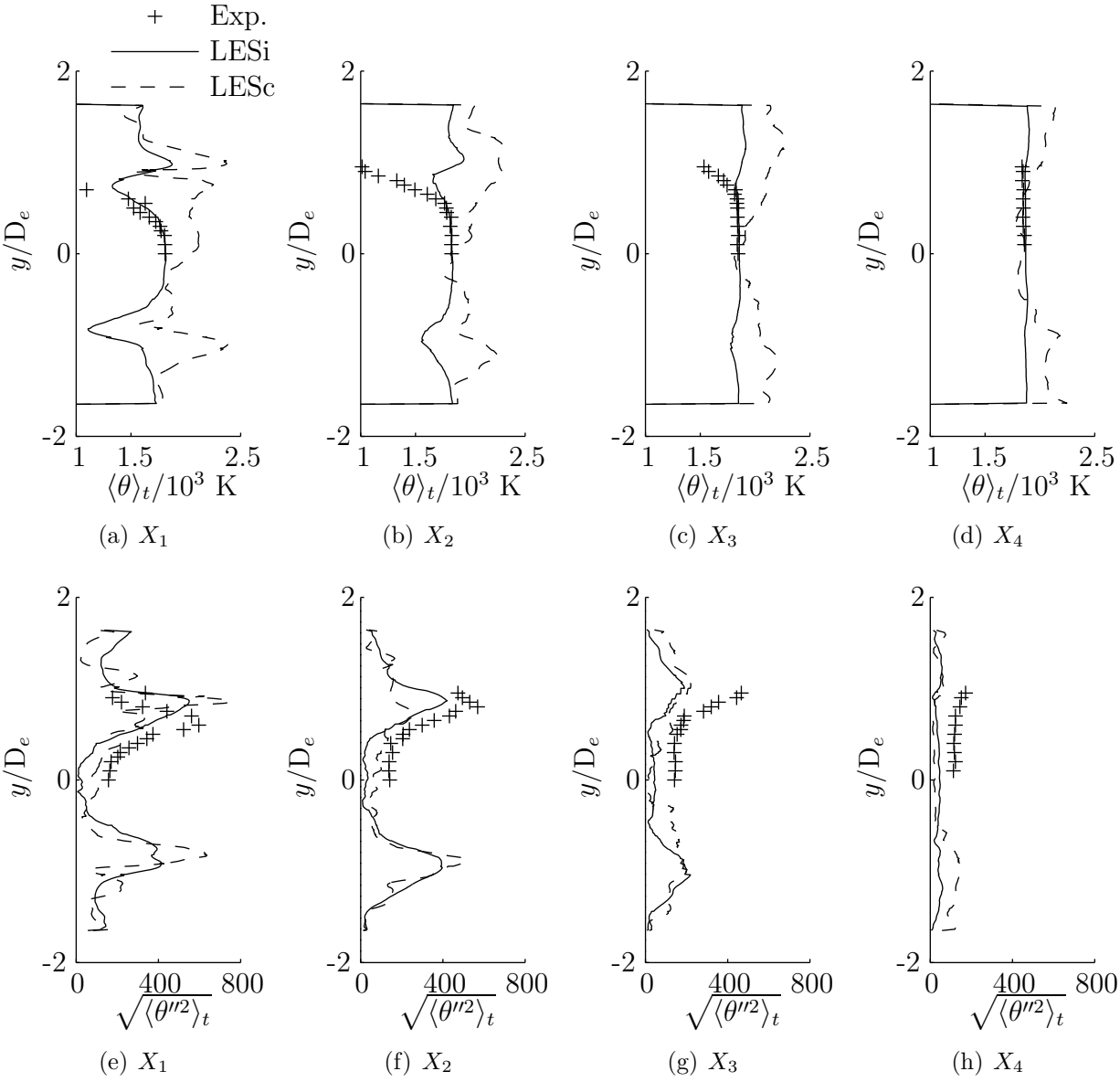

Figure 4.8.: Transverse profiles of temperature statistics, symbols: experiment [92], solid lines: simulation; (a)-(d) time-averaged mean, (e)-(h) root-mean-square.

The agreement between the predicted and measured root-mean-square of the temperature fluctuations is generally more satisfactory, *c.f.* Figure 4.8 (e)-(h). The trends are qualitatively well reproduced at all axial stations. However, both simulations underestimate the level of the temperature fluctuations in the annular swirling jet and the CRZ. The largest discrepancies occur in the swirling jet at X_3, where both simulations underestimate the measurements by approximately 50 %. The discrepancies may be due to the upstream shift of the flame in the simulations, leading to less mixing with fluid at a lower temperature than the burnt mixture temperature.

Figure 4.9 presents the statistical mass fraction profiles of CH_4. At all axial stations, both simulations underpredict the measured mean CH_4 mass fraction in the swirling jet.

The discrepancies are particularly pronounced at the upstream station X_1, where LESi underpredicts the measurements by approximately 60 % and LESc by roughly 80 %. The time-averaged mean profile of LESc at X_1 is somewhat narrower than the LESi profile, which significantly affects the profiles further downstream. This may be interpreted as the result of an overpredicted fuel consumption rate in the simulations leading to an upstream shift of the flame position. Consistent with the temperature predictions, the shift of the flame position is more pronounced in LESc.

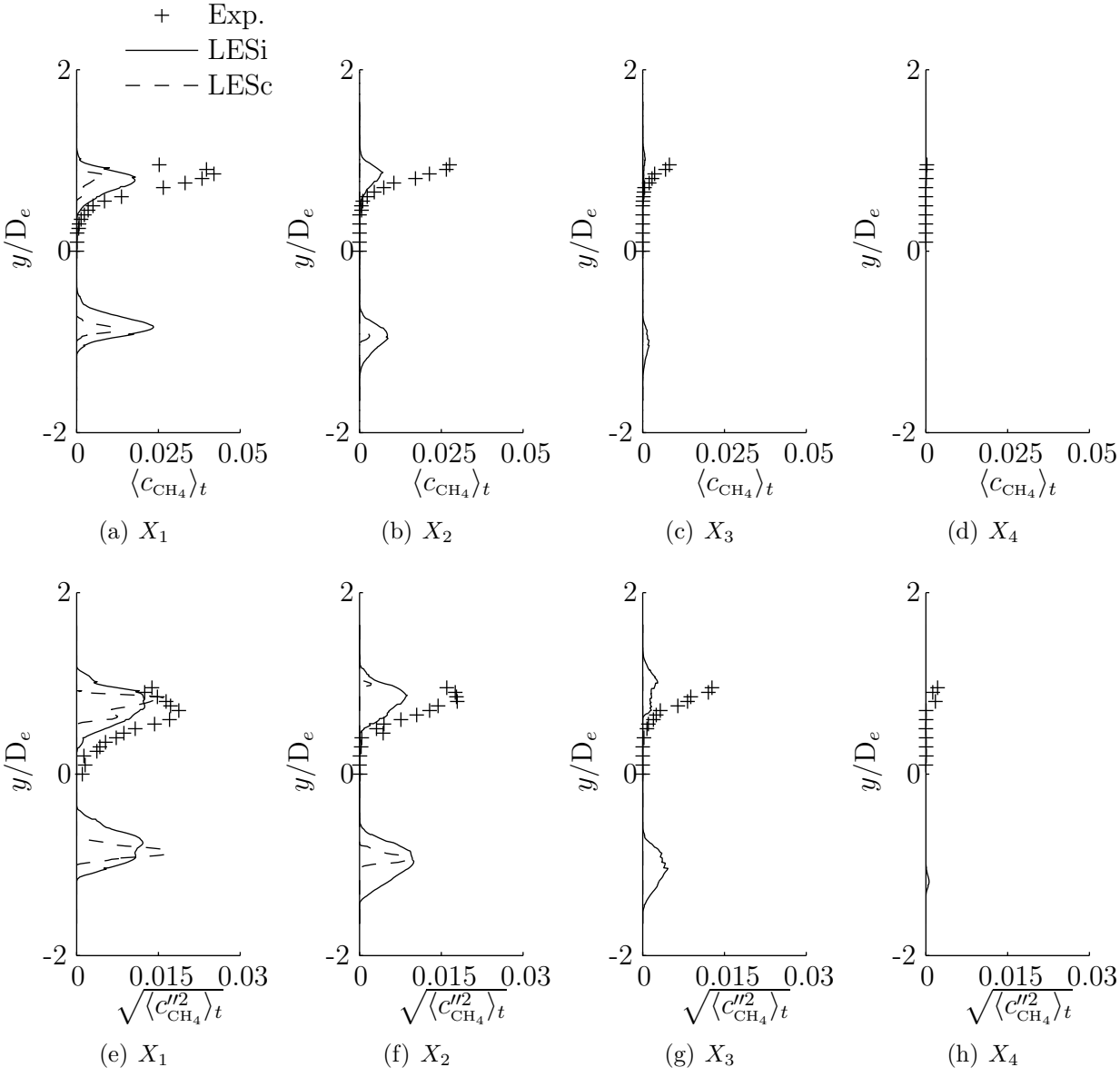

Figure 4.9.: Transverse profiles of $c_{\mathrm{CH_4}}$ statistics, symbols: experiment [92], solid lines: simulation; (a)-(d) time-averaged mean, (e)-(h) root-mean-square.

The predicted root-mean-square levels of the $c_{\mathrm{CH_4}}$ fluctuations are in better agreement with the measurements. LESi is able to predict the measured profile at X_1. However, further downstream, LESi predicts the peak values in the swirling jet to decay faster than the measurements, which appears to be a consequence of the flame shift. The measurements at X_3 show a non-zero fuel mass fraction in the swirling jet confirming that the flame is still present at this location. LESc, on the other hand, suggests zero

mean mass fraction and zero root-mean-square of the mass fraction fluctuations at this station, leading to the conclusion that the fluid has already approached the fully burnt state.

Consistent with the above results, the mean O_2 mass fraction in the swirling jet is underpredicted by both simulations, *c.f.* Figure 4.10. This trend is again more pronounced in the simulation LESc. Moreover, the mean values predicted by LESc are significantly underestimated in the CRZ at X_1, where LESi is able to reproduce the measurements with good accuracy. The mean O_2 mass fractions predicted by LESc in the CRZ recover further downstream and tend to agree better with the measurements at the axial stations $X_2 - X_4$.

The root-mean-square levels of the oxygen mass fraction fluctuations are generally better predicted than the time-averaged mean values, *c.f.* Figure 4.10 (e)-(h). Larger discrepancies between the measurements and the predictions are evident at X_3 in the swirling jet, where both simulations underestimate the measurements by roughly 50 %.

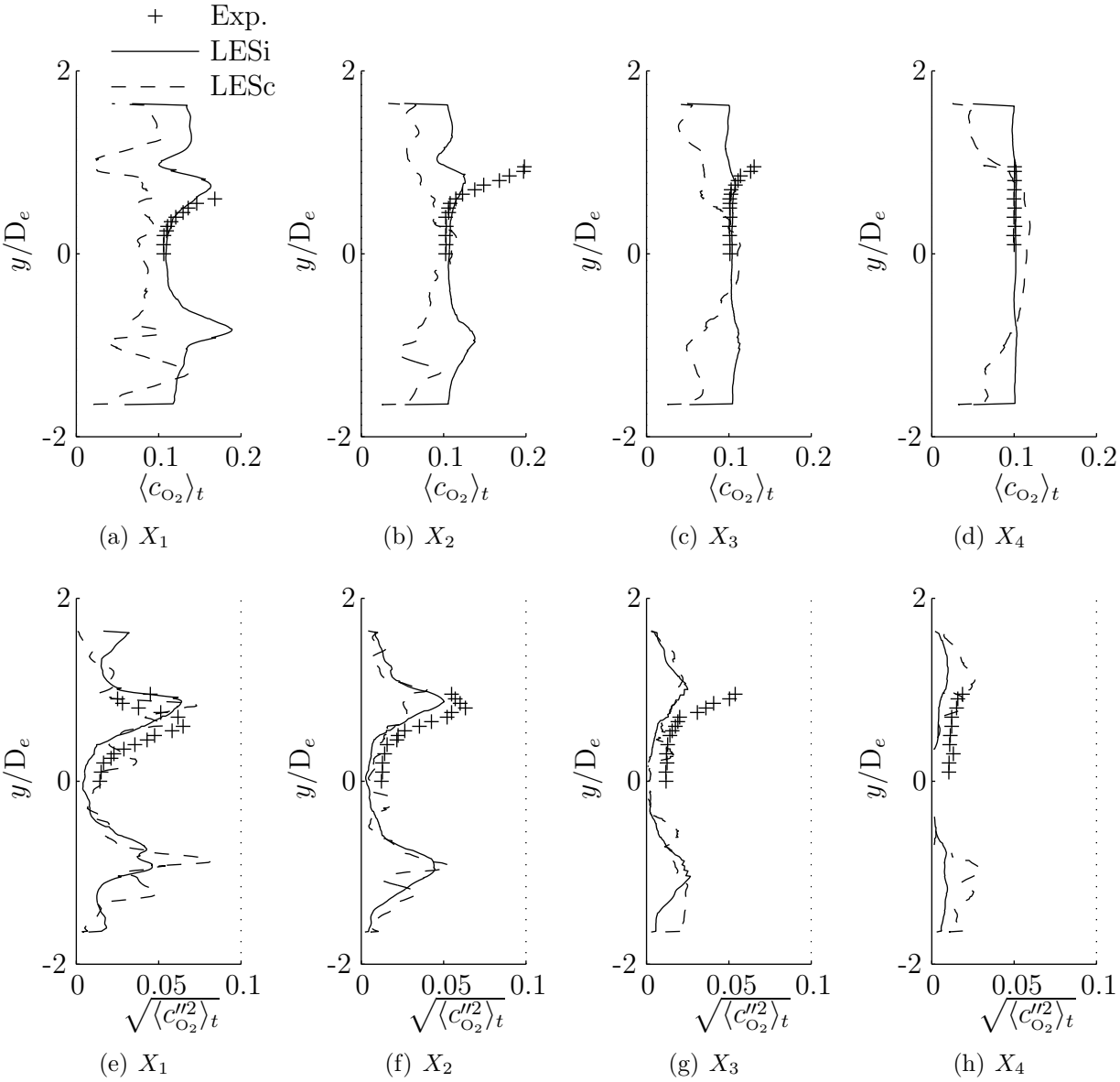

(a) X_1 (b) X_2 (c) X_3 (d) X_4

(e) X_1 (f) X_2 (g) X_3 (h) X_4

Figure 4.10.: Transverse profiles of c_{O_2} statistics, symbols: experiment [92], solid lines: simulation; (a)-(d) time-averaged mean, (e)-(h) root-mean-square.

Profiles of the CO_2 statistics are shown in Figure 4.11. The time-averaged mean values are well predicted by LESi at all axial stations, in particular in the CRZ at X_1 and X_2, *c.f.* Figure 4.11 (a)-(d). Further downstream, at X_3 and X_4, LESi slightly overestimates the measured time-averaged mean values. The asymmetry in the LESi profiles about the centre axis is the result of the observed flame flash back into the pre-chamber [*c.f.* Figure 4.4 (b)], yielding higher mean mass fractions of CO_2 in the swirling jet at $y/\mathrm{D}_e \approx 1$. LESc overpredicts the mean mass fraction at X_1 across the transverse direction, which is consistent with the underprediction of the oxygen mass fraction discussed above, *c.f.* Figure 4.10 (a). This result clearly indicates that the flame position is significantly shifted further upstream in LESc. At the downstream positions X_3 and X_4, the LESc results agree closer with the measurements, especially in the centre region $-0.2 \leq y/\mathrm{D}_e \leq 0.2$. In fact, at X_4, LESc agrees better with the measurements in the centre region than LESi. Due to the short averaging time in LESc, the mean profiles appear asymmetric with respect to the centre axis.

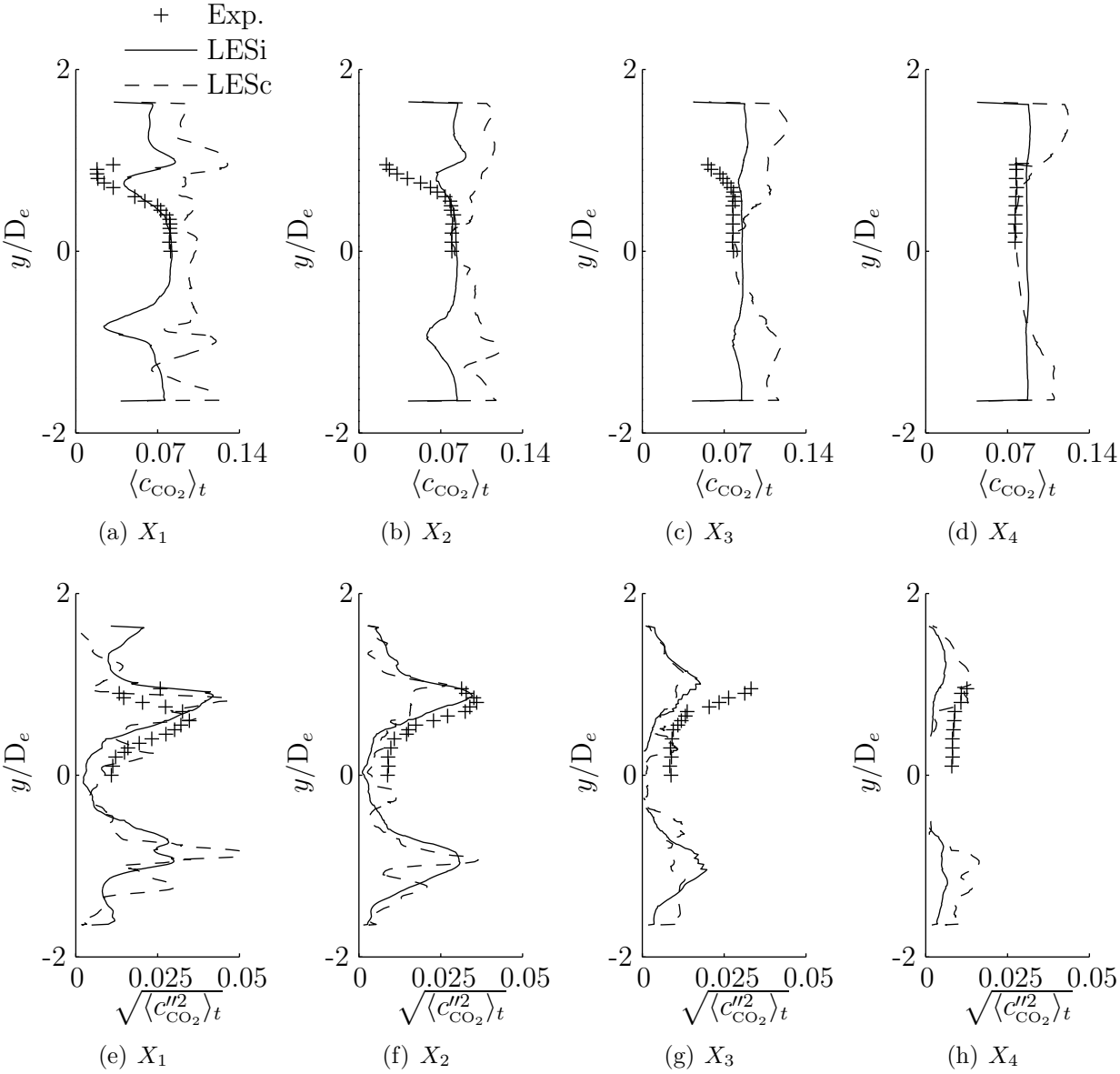

Figure 4.11.: Transverse profiles of c_{CO_2} statistics, symbols: experiment [92], solid lines: simulation; (a)-(d) time-averaged mean, (e)-(h) root-mean-square.

The predicted root-mean-square levels of the c_{CO_2} fluctuations are generally in good agreement with the measurements throughout.

Transverse profiles of the mixture fraction statistics are shown in Figure 4.12. The mean mixture fraction profiles predicted by LESi agree closely with the measurements at all axial stations. At X_1, the mean mixture fraction appears fairly equally distributed, suggesting good mixing of fuel and oxidiser. With increasing distance from the inlet of the combustion chamber the mean mixture fraction profiles become more uniform. At X_4, the profiles have become entirely flattened out, which is well predicted by LESi. The LESc results, on the other hand, show noticeable deviations from the measurements in the swirling jet which is due to the significant flame shift. The root-mean-square levels of the mixture fraction fluctuations generally agree better with the measurements than the mean mixture fraction. Both simulations slightly underestimate the level of the fluctuations, but reproduce the profile shapes.

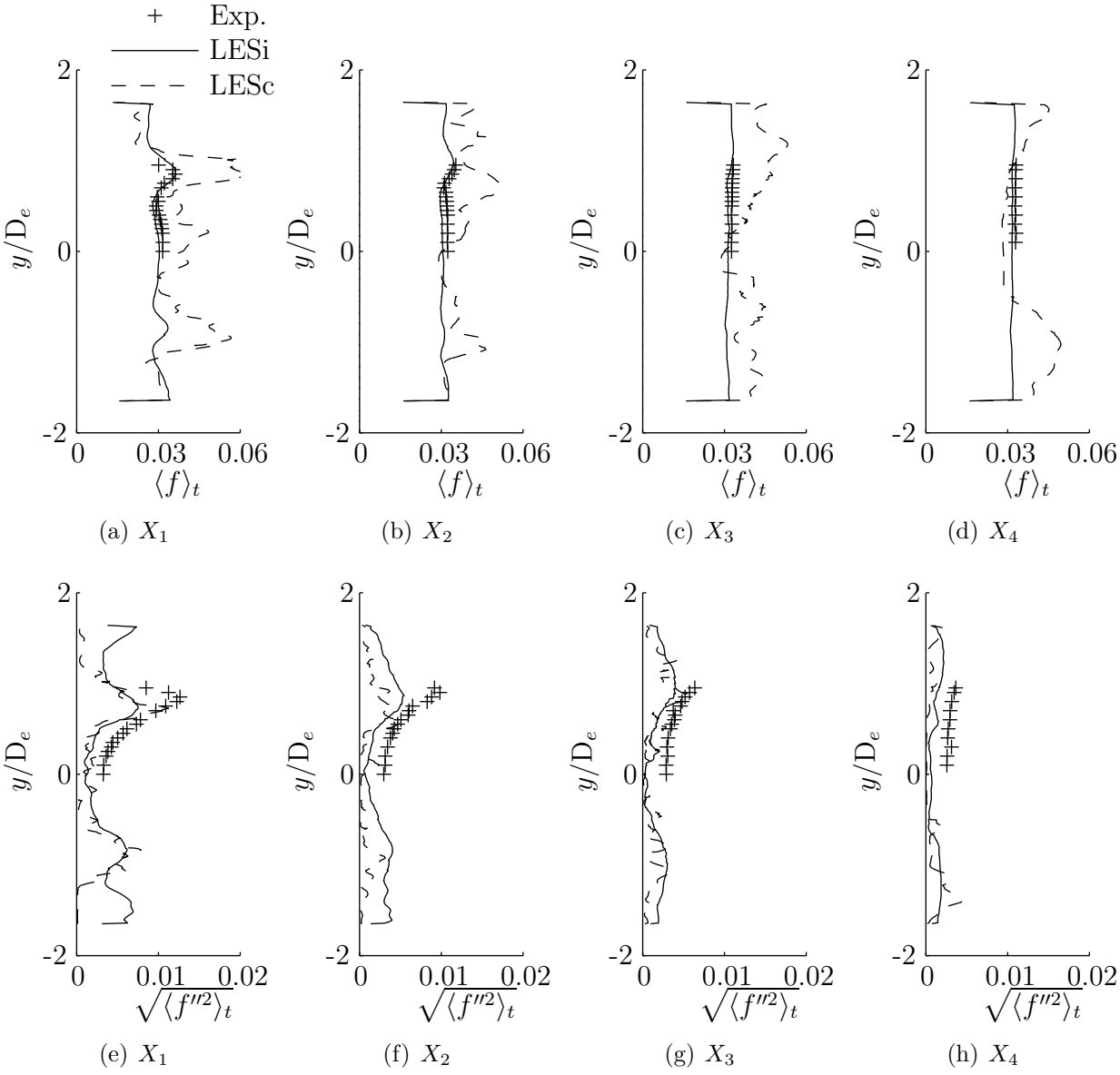

(a) X_1 (b) X_2 (c) X_3 (d) X_4

(e) X_1 (f) X_2 (g) X_3 (h) X_4

Figure 4.12.: Transverse profiles of the mixture fraction statistics, symbols: experiment [92], solid lines: simulation; (a)-(d) time-averaged mean, (e)-(h) root-mean-square.

Frequency Analysis

The following analysis is dedicated to investigate whether or not the simulation LESc is able to predict the self-excited flame oscillation observed in the experiment. For this reason, Figure 4.13 compares the single-sided amplitude spectrum of the measured with that of the predicted pressure time history. The spectrum of the predicted pressure history was computed by joining the HANN-windowed pressure histories of eight monitor positions distributed circumferentially at the same axial position where the pressure tap was located in the experiment. In light of the relatively short time period resolved in the simulation LESc, this led to a better frequency resolution than computing the amplitude spectrum for each monitor individually and applying an ensemble average to the individual spectra. The frequency resolution achieved with this approach is 29 Hz. On the other hand, the frequency spectrum contains redundant information on the same flow phenomena in the resolved time period. STOPPER *et al.* reported about systematic errors in the acoustic measurements and indicated that the dominant frequency is accurate to within 10 Hz. Thus there is larger uncertainty with regard to the characteristic frequencies in the spectra of the predicted time histories.

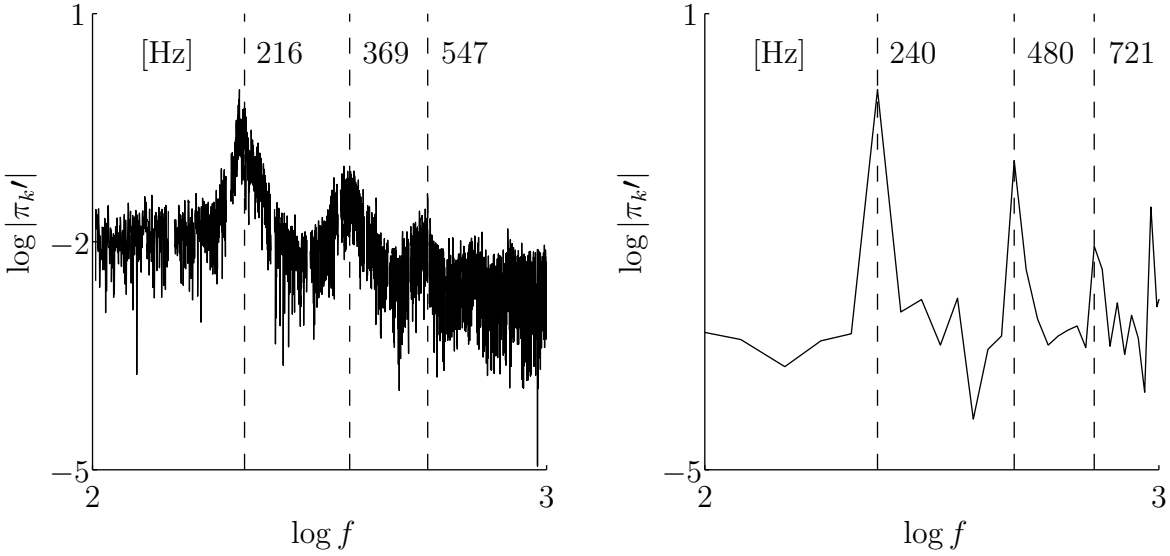

Figure 4.13.: Single-sided amplitude spectrum of the pressure fluctuations; (a) experiment [92], (b) LESc.

Both the experimental and predicted spectra identify three characteristic frequencies with decreasing amplitude. The dominant frequency in the predicted pressure spectrum is 240 Hz and in the experimental spectrum 216 Hz. It should be remarked at this point that the resolved time period in the simulation only covers approximately two periods of the oscillation at the dominant frequency. Hence, the predicted characteristic frequencies must be regarded with caution. Larger deviation between experiment and simulation is evident at the two higher characteristic frequencies. The second and third characteristic frequency predicted in the simulation differ from the experimental ones by 30 % and 32 %, respectively. It appears that the second characteristic frequency predicted by LESc is the second harmonic of the dominant frequency. This is not the case in the experimental

spectrum. From the obtained results can be concluded that the simulation indeed predicts an energetic pressure oscillation at a frequency close to the experimentally determined.

The dominant frequency of 240 Hz also exists in the predicted spectrum of the turbulent kinetic energy, *c.f.* Figure 4.14. However, the two higher characteristic frequencies are absent. This result seems to suggest that the pressure field excites the velocity field only at the dominant frequency. Hence implying a low-pass behaviour of the velocity field, which was also observed in the analysis of the forced flame excitation in the preceding chapter.

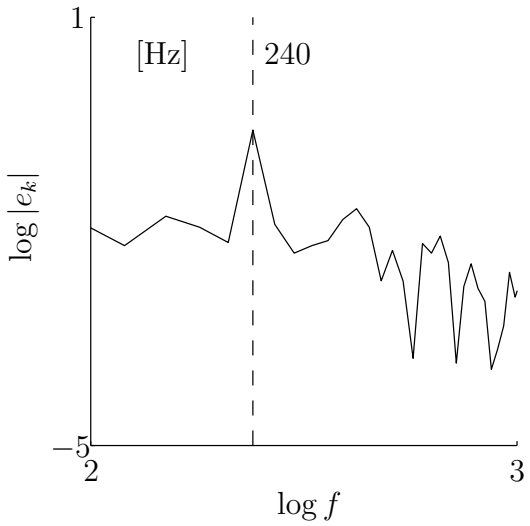

Figure 4.14.: Single-sided amplitude spectrum of the turbulent kinetic energy predicted by LESc

Figure 4.15 shows the recorded time signal of the total heat release rate along with snapshots of the axial velocity in the median plane of the combustion chamber at different times during the presumed oscillation cycle. The recorded time signal indeed shows large fluctuations of the total heat release rate reaching up to 30 % of its time-averaged mean value. The simulation predicts a mean value of 900 kW, which lies above the value of 685 kW given in [92]. This is consistent with the overpredicted temperatures on the burnt side, *c.f.* Figure 4.8. The heat release rate contour clearly shows a lateral movement of the flame in the course of the oscillation cycle. With a short time delay the CRZ begins to expand laterally and to move axially leading to lower velocities in the CRZ near the inlet of the combustion chamber. At the same time the ORZ becomes weaker, divides axially into two parts and decreases in its radial extent. This evolving flow pattern is approximately symmetric with respect to the centre axis. Stopper *et al.* have observed the very same flow features in their experiment. In addition, the authors identified mixture fraction variations near the inlet of the combustion chamber which they attributed to global equivalence ratio variations caused by different responses of the fuel and oxidiser supply lines to upstream propagating pressure waves. As was mentioned in section 4.3, this mechanism is excluded in the simulation due to the inlet boundary treatment employed in the present case. The inlet boundary treatment does not admit global equivalence ratio variations. The mixture fraction variations may thus be explained with the laterally moving flame.

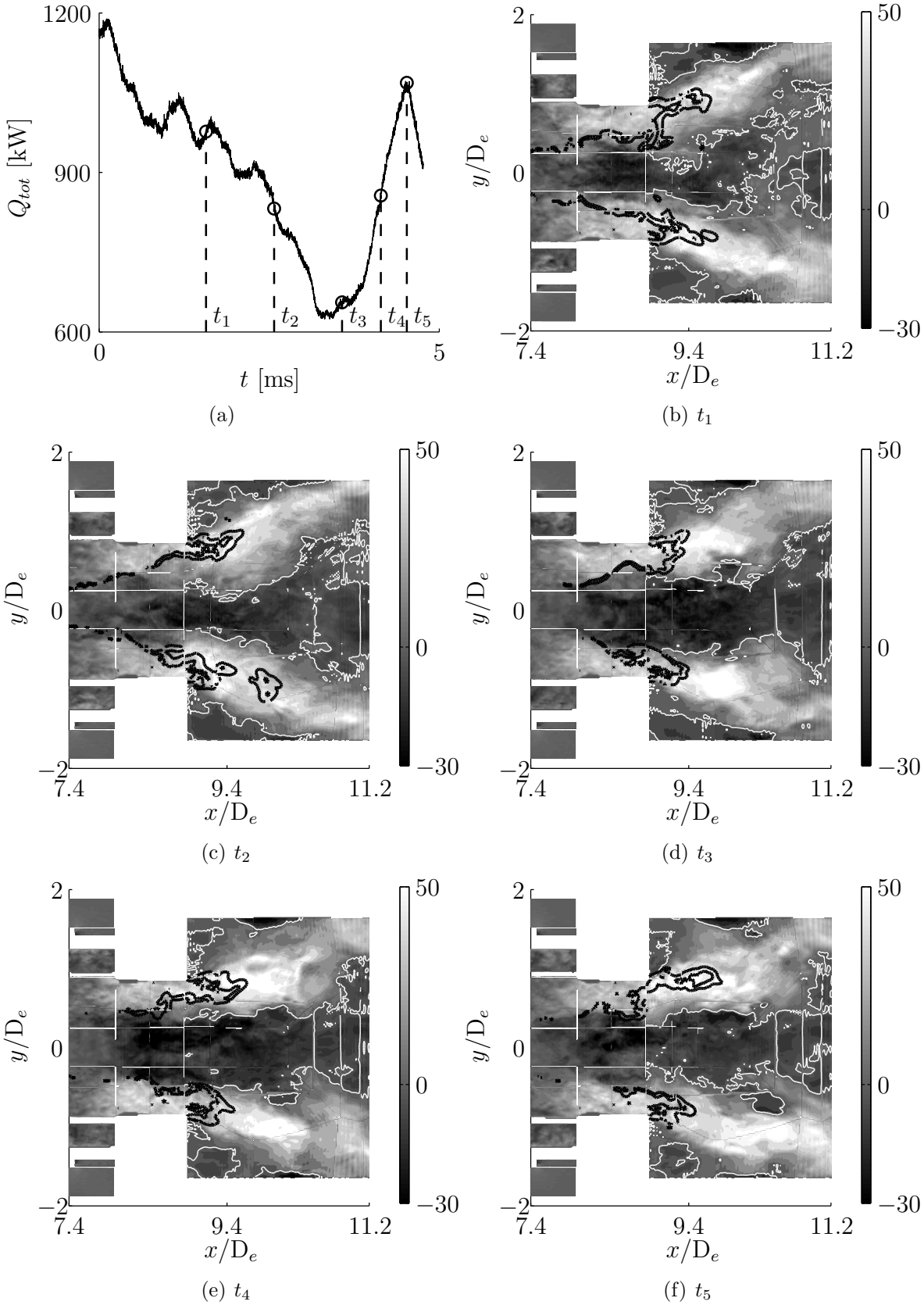

Figure 4.15.: Flame oscillation predicted by LESc; (a) time signal of the total heat release rate, (b)-(f) axial velocity in the combustor median plane at different times during the cycle. The thin white lines represent the zero contour of the axial velocity. The thick black line is the contour of the heat release rate at 10^9 Wm^{-3}.

In a rather casual description the flame oscillation may be compared with an expanding and contracting rubber bulb 'pumping' periodically fluid into the pre-chamber. However, a longer time period must be resolved in the simulation to confirm whether or not the flame oscillation is sustained. If confirmed the implications of such a flame behaviour are twofold. First, the dominant frequency in the pressure spectrum is not primarily an interaction of the flame with an acoustic mode of the combustion chamber, as the acoustic modes lie above the dominant frequency. Second, the flame oscillation is not caused by global equivalence ratio variations induced by mass flow rate modulations of the fuel and oxidiser supply lines.

Figure 4.16 shows the instantaneous velocity vector together with the contour of the heat release rate in the median plane of the combustion chamber at the same times which are marked in Figure 4.15 (a).

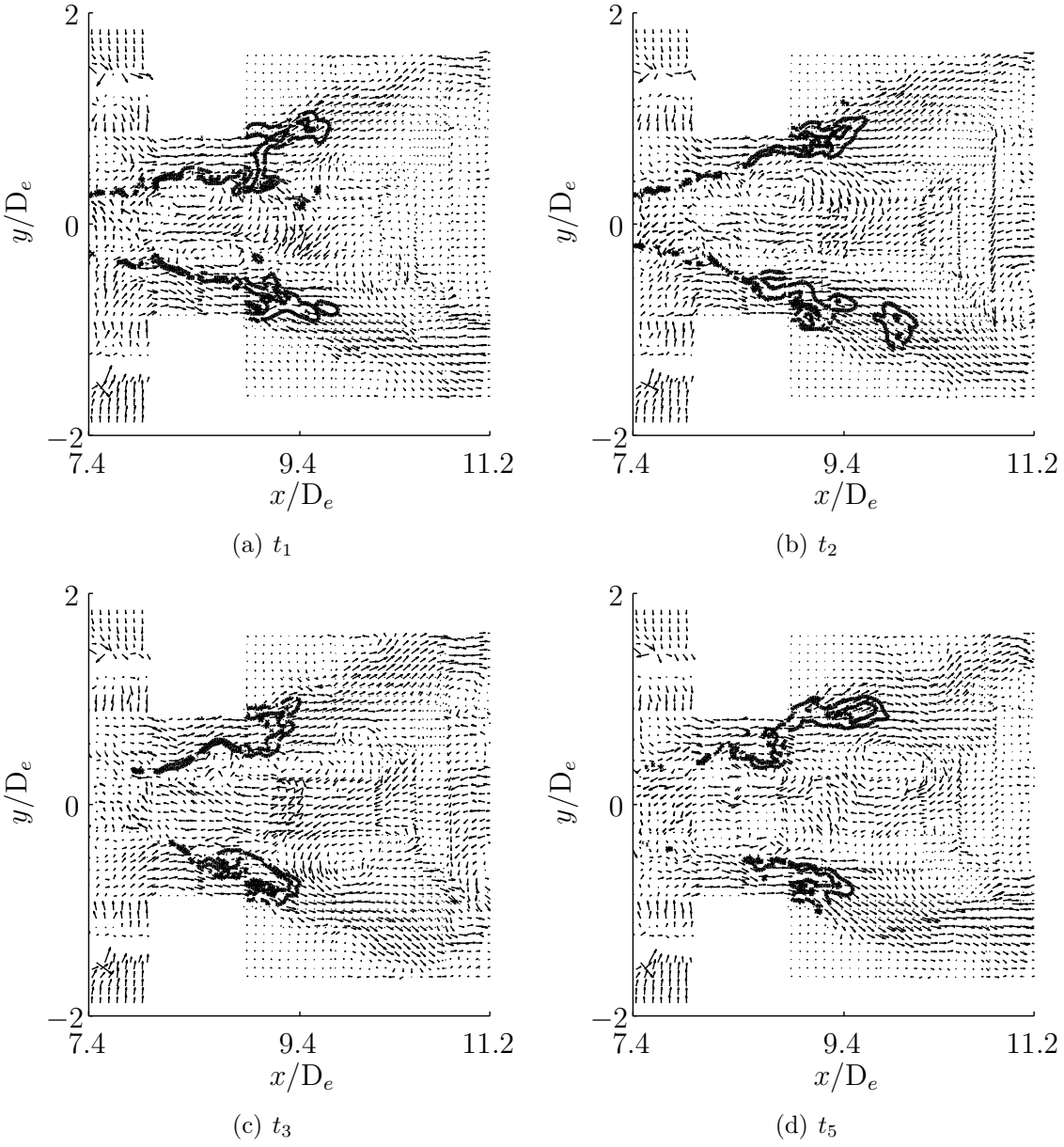

(a) t_1 (b) t_2

(c) t_3 (d) t_5

Figure 4.16.: Velocity vector in the median plane of the combustion chamber together with the contour of the heat release rate at 10^9 Wm^{-3} (thick black line). The swirl component of the velocity vector is omitted.

A vortex ring is present in the pre-chamber at t_1. In the course of the cycle this vortex ring convects out of the pre-chamber and appears to expand radially, thereby pushing the flame radially outwards. It seems as if the flame is 'pulled' back from the front panel of the pre-chamber when the vortex ring exerts tangential forces on the flame in the inner shear layer at the exit of the pre-chamber. As a result, the flame is no more attached to the front panel of the pre-chamber at t_3, implying a likely extinction of the flame by high shear forces. The vector plot at t_3 also shows a noticeable reverse flow in the centre-region of the pre-chamber consistent with Figure 4.15 (d). Hence, fluid from the region downstream of the combustor inlet is convected into the pre-chamber. The interaction of the vortex ring with the flame appears to be responsible for the lateral movement of the flame and the large fluctuations of the total heat release rate, *c.f.* Figure 4.15 (a).

4.5. Conclusions

The time-averaged results show that LESi is able to predict the statistics for the velocity field, species mass fractions and temperature near the inlet of the combustion chamber with good accuracy. Small deviations between the simulation and experiment are observed in the swirling jet, which is attributed to a slight upstream shift of the flame position in LESi. Larger differences are found in the velocity field at the downstream measurement stations near the centre axis. These discrepancies are associated with an overestimation of the vortex strength of the Central Vortex Core (CVC) due to the assumption of an incompressible fluid. The MACH number at the exit of the combustion chamber has a value of approximately 0.3, which implies that compressibility effects play an important role in this region. As a result the simulation predicts the CVC too far upstream towards the inlet of the combustion chamber.

The mean temperature and mass fraction profiles predicted by LESc are in less satisfactory agreement with the measurements. The predicted results indicate that the mean flame position is shifted even further upstream, leading to an underprediction of the mean fuel mass fraction near the combustor inlet. At the same time, the mean mass fraction of carbon dioxide is overpredicted. The large flame shift is suspected to be connected with inaccuracies in the measured fuel and oxidiser mass flow rates and numerical errors in the mixture composition on the unburnt side caused by large values of the stochastic velocities. On the other hand, LESc gives better results for the time-averaged velocity vector near the centre axis. This can be ascribed to a better representation of the vortex strength of the CVC, since the velocity field of the CVC is affected by the fluid compressibility near the exit of the combustion chamber.

The frequency analysis of the results obtained with LESc reveals a dominant frequency in the pressure spectrum which is reasonably close to the experimentally determined frequency of the flame oscillation. The difference between the two frequencies is 11 %. Further analysis shows that the flame is indeed oscillating, predominantly in the lateral direction. A larger time period must be resolved to confirm the sustained flame oscillation. The obtained results imply that the flame oscillation is not coupled to the acoustic mode of the exhaust cooling pipe, since the pipe was not included in the computational domain. In addition, the imposed inlet boundary treatment in LESc excludes global equivalence ratio variations as a mechanism for sustained flame oscillation. The instantaneous velocity field suggests that the flame is pushed radially outwards by an expanding vortex ring originating from the pre-chamber. The vortex ring appears to 'pull' the flame from the front panel when leaving the pre-chamber, which leads to an axial contraction of the

flame. At the same time fluid is convected into the Central Recirculation Zone (CRZ) from the region downstream of the inlet of the combustion chamber.

5. Summary and Outlook

The first part of the thesis describes a modelling framework for investigating the interaction of pressure waves with flames to identify conditions under which flame oscillation may be initiated. A numerical framework based on the Discontinuous Galerkin (DG) method with high-order accuracy in space and time is presented to carry out the investigations. Both pressure wave and flame are assumed to remain plane at all times to exclude three-dimensional effects and to isolate the influence of the reaction-diffusion processes on the flame response when perturbed by the pressure wave. The following strategy is pursued to carry out the investigations. First, solutions of the field equations are sought which describe the steady propagation of plane flames. This is done by solving the field equations in a frame which moves with the flame. It was shown that the DG method reproduces the flame speed and the steady flame structure with good accuracy. After the flame has approached the state of steady propagation, the velocity of the moving frame is held fix in time and a pressure wave is imposed at the boundary on the unburnt side of the flame. The simulation results of the pressure wave-flame interaction have revealed the following. The pressure wave incident upon the flame is reflected at and transmitted through the flame when the time scale associated with the wave just in front of the flame is of the same order as the time scales of the chemical reactions in the primary reaction zone. In this case, the velocity wave associated with the imposed pressure wave is amplified due to the fluid acceleration across the flame layer. The flame response also depends on the wave strength upon impact. The results suggest that an amplitude threshold exists below which the pressure wave is damped out. Systematic studies should be conducted to assess thoroughly the effect of the mixture composition on the unburnt side of the flame and the wave properties, such as wave shape, wave length and amplitude, on the response of the flame. In order to facilitate the analysis an implicit time integration scheme should be considered to lift the strict stability requirements on the time step leading to prohibitively small time step sizes.

The second part of the thesis is concerned with the analysis of the forced oscillating flame in the turbulent flow around a conical bluff body using the Large Eddy Simulation (LES) technique in conjunction with the Probability Density Function (PDF) modelling of the unresolved turbulence-chemistry interaction. Good overall agreement is obtained between the LES predictions and the measurements for both the chemically inert and reacting flows. The non-linear evolution of the total heat release rate is especially well captured. However, the results show a noticeable phase shift between the predicted total heat release rate and the measured OH^* chemiluminescence. This phase shift is investigated by comparing the measured OH^* chemiluminescence and the predicted OH mass fraction with the predicted total heat release rate. The bulk of the measured OH^* chemiluminescence as well as the predicted OH mass fraction are found in the secondary reaction zone while the majority of the heat of reaction is liberated at an earlier time in the primary reaction zone implying a phase shift between the total heat release rate and the bulk of the OH mass fraction. In further studies it should be considered to investigate whether the phase shift depends on the frequency of the mass flow rate excitation. Alter-

native chemical markers to quantify the total heat release rate variation are investigated. In the present case of a lean-premixed ethylene-air mixture at atmospheric pressure it is found that formaldehyde-based markers are not appropriately representing the phase and amplitude of the total heat release rate. The product of the mass fractions of molecular oxygen and the ketenyl radical correlates better with the total heat release rate.

The last part of the thesis presents the simulation of a self-excited flame oscillation in turbulent swirling flow using the LES-PDF approach. The burner system studied is the Siemens SGT-100 combustor comprising the swirl generating device, pre-chamber, combustion chamber and transition duct to the exhaust pipe. Two simulations are conducted. In the first one the mixture is assumed to be incompressible (LESi) and in the second one the mixture is modelled as being compressible (LESc). The simulation LESi is used as a reference for the case LESc in the comparison of the predicted flow statistics. The LESi results are in good agreement with the measurements for the velocity field, species mass fraction and temperature. Small deviations between the LESi results and measurements are observed in the swirling jet, which is attributed to a slight upstream shift of the flame position in the simulation. The time-averaged mean results of LESc are in less satisfactory agreement with the measurements. Although LESc predicts the velocity field better than LESi the temperature and mass fraction profiles predicted by LESc differ significantly from the measurements. This is attributed to an even larger upstream flame shift in LESc. The frequency analysis of the predicted pressure recordings reveals a dominant frequency which differs by 11 % from that of the experimentally determined spectrum. Further analysis suggests that the flame is indeed oscillating, predominantly in the lateral direction. A vortex ring which is convected out of the pre-chamber is likely responsible for the flame oscillation. A larger time period must be resolved to confirm the sustained flame oscillation.

A. Rational Thermodynamics for Flames

A.1. Basic Concepts

A rather general and complete mixture theory which avoids the paradox of diffusion is the theory of mixtures developed by MÜLLER [71]. MÜLLER's theory originates from the *Rational Thermodynamics* (RT) of TRUESDELL AND TOUPIN [99] and contains as a special case the Ordinary Thermodynamics (OT) of mixtures employing FICK's law, *cf.* section 1.4. The terms Rational Thermodynamics and MÜLLER's theory are used interchangeably here. Full understanding of this section requires good knowledge of the concepts and formulae of RT. The reader may thus consult [16, 71, 97, 99] and the references cited therein for further information on the subject. The description of the well-established kinematics of mixtures can be found in the above references. Equations in the following are expressed in the direct notation introduced by TRUESDELL AND NOLL [98].

The application of MÜLLER's theory to flames requires two extensions: the theory must admit more than two mixture constituents and chemical reactions. Such extensions are indeed possible and will be laid down in the following. The subsequent derivation follows closely MÜLLER's work [71] both in structure and methodology. To begin with, it seems advantageous to give the principles and ideas that underlie MÜLLER's theory:

1.) All properties of the mixture must be mathematical consequences of properties of the constituents (TRUESDELL [97, Lecture 5]).

2.) "So as to describe the motion of a constituent, we may in imagination isolate it from the rest of the mixture, provided we allow properly for the actions of the other constituents upon it" (TRUESDELL [97, Lecture 5]).

3.) The motion of the mixture is governed by the same equations as is a single body (TRUESDELL [97, Lecture 5]).

4.) The principle of equipresence of the independent constitutive variables in the material functionals (TRUESDELL AND TOUPIN [99]).

5.) The principle of local action (BERTRAM [11]).

6.) The principle of determinism (BERTRAM [11]).

7.) The principle of objectivity (BERTRAM [11]).

8.) The second axiom of thermodynamics must to be satisfied identically (COLEMAN AND NOLL [23]).

9.) The entropy flux is not related *a priori* to the heating flux, but is given by a constitutive equation (MÜLLER [71]).

Basic Dynamical Equations

A mixture composed of $\mathfrak{N}$ non-polar constituents is considered. It is supposed that every place in the region of space occupied by the mixture is simultaneously taken by exactly $\mathfrak{N}$ particles from the $\mathfrak{N}$ constituents that make up the mixture. The kinematical description of the motion of each constituent is supposed to ensure that any two particles from the same constituent, $X_{\mathfrak{a}}^1$ and $X_{\mathfrak{a}}^2$, cannot occupy the same spatial position $\mathbf{x}$. Equally, it is assumed that a particle $X_{\mathfrak{a}}$ of the $\mathfrak{a}$th constituent cannot occupy two spatial positions. Each constituent has its own mass and thus its mass density $\rho_{\mathfrak{a}} = \rho_{\mathfrak{a}}(\mathbf{x}, t)$, and its own velocity $\mathbf{v}_{\mathfrak{a}} = \mathbf{v}_{\mathfrak{a}}(\mathbf{x}, t)$ relative to some frame of reference. All constituents have the same temperature $\theta = \theta(\mathbf{x}, t)$. A few definitions in addition to (1.1)-(1.3) are made to simplify the formulae in the remainder:

barycentric velocity	$\mathbf{v} \equiv \frac{1}{\rho} \sum_{\mathfrak{a}=1}^{\mathfrak{N}} \rho_{\mathfrak{a}} \mathbf{v}_{\mathfrak{a}}$,	(A.1)
rate of deformation tensor of the $\mathfrak{a}$th constituent	$\mathbf{D}_{\mathfrak{a}} \equiv \operatorname{sym}\{\operatorname{grad} \mathbf{v}_{\mathfrak{a}}\}$,	(A.2)
velocity differences	$\mathbf{v}_{\mathfrak{a}\mathfrak{N}} \equiv \mathbf{v}_{\mathfrak{a}} - \mathbf{v}_{\mathfrak{N}}$,	(A.3)
density gradient of the $\mathfrak{a}$th constituent	$\mathbf{d}_{\mathfrak{a}} \equiv \operatorname{grad} \rho_{\mathfrak{a}}$,	(A.4)
temperature gradient	$\mathbf{g} \equiv \operatorname{grad} \theta$,	(A.5)

In Rational Thermodynamics the $4\mathfrak{N} + 1$ fields $\{\rho_{\mathfrak{a}}, \mathbf{v}_{\mathfrak{a}}, \theta\}$ are governed by the equations of balance of masses and linear momenta of the constituents and by the conservation law of energy of the mixture. These differential equations may be written in the form listed in Table A.1.

Table A.1.: List of thermomechanical equations of balance.

Equation	Differential form	Ref.	Number
Balance of mass for the $\mathfrak{a}$th constituent	$\dot{\rho}_{\mathfrak{a}} + \operatorname{div}(\mathbf{v}_{\mathfrak{a}} \rho_{\mathfrak{a}}) = \widehat{c}_{\mathfrak{a}}$	$(A.6)$	$\mathfrak{N} - 1$
Balance of mass for the mixture	$\dot{\rho} + \operatorname{div}(\rho \mathbf{v}) = 0$	$(A.7)$	1
Balance of momentum for the $\mathfrak{a}$th constituent	$\overset{\bullet}{\overline{(\rho_{\mathfrak{a}} \mathbf{v}_{\mathfrak{a}})}} + \operatorname{div}(\rho_{\mathfrak{a}} \mathbf{v}_{\mathfrak{a}} \otimes \mathbf{v}_{\mathfrak{a}} - \mathbf{T}_{\mathfrak{a}}) = \widehat{\mathbf{m}}_{\mathfrak{a}}$	$(A.8)$	$3(\mathfrak{N} - 1)$
Balance of momentum for the mixture	$\overset{\bullet}{\overline{(\rho \mathbf{v})}} + \operatorname{div}(\rho \mathbf{v} \otimes \mathbf{v} - \mathbf{T}) = \mathbf{0}$	$(A.9)$	3
Energy balance for the mixture	$\overset{\bullet}{\overline{(\rho \epsilon)}} + \operatorname{div}(\rho \epsilon \mathbf{v} + \mathbf{q}) = \operatorname{tr}(\mathbf{TD})$	$(A.10)$	1
		Sum	$4\mathfrak{N} + 1$

Body force terms and the external heat supply density are neglected in the above set of differential equations. The functions $\widehat{\mathbf{m}}_{\mathfrak{a}} = \widehat{\mathbf{m}}_{\mathfrak{a}}(\mathbf{x}, t)$ in the equations of balance of linear momenta (A.8) represent the momentum supply for the $\mathfrak{a}$th constituent, which arises from the momentum exchange due to diffusion. Together with $\widehat{c}_{\mathfrak{a}}$, these terms have major importance in the mathematical treatment of flames, as discussed in section 1.4. What distinguishes the above system of non-linear differential equations from Ordinary

Thermodynamics are the momentum balances (A.8). These determine the motion of the $\mathfrak{a}$th constituent and hence constitute a more general form of FICK's law. The intensity of the chemical reactions in the flame layer and thus the flame speed depend to a large extent on the mass fractions of the radicals, which themselves are only formed in the flame layer. The diffusion processes in the flame layer are not taking place under isothermal or isobaric conditions, which raises concerns about the validity of FICK's law in this regime. MÜLLER's theory produces more accurate results than Ordinary Thermodynamics for the diffusion processes under unsteady conditions. By using the definition

$$\mathbf{T} \equiv \sum_{\mathfrak{a}=1}^{\mathfrak{N}} \mathbf{T}_{\mathfrak{a}} - \sum_{\mathfrak{a}=1}^{\mathfrak{N}} \rho_{\mathfrak{a}} \mathbf{u}_{\mathfrak{a}} \otimes \mathbf{u}_{\mathfrak{a}} \ , \tag{A.11}$$

it can be shown that (A.7) and (A.9) are equivalent to

$$\sum_{\mathfrak{a}=1}^{\mathfrak{N}} \widehat{c}_{\mathfrak{a}} = 0 \quad \text{and} \quad \sum_{\mathfrak{a}=1}^{\mathfrak{N}} \widehat{\mathbf{m}}_{\mathfrak{a}} = \mathbf{0} \ , \tag{A.12}$$

respectively. The additional fields $\mathbf{T}_{\mathfrak{a}}$ in (A.8) represent the partial stresses. From the conservation of moment of momentum follows the symmetry of the total stress. Since the constituents of the mixture are assumed to be non-polar the balance of moment of momentum of the $\mathfrak{a}$th constituent implies the symmetry of the partial stresses. For all the additional $10\mathfrak{N}+4$ fields $\{\widehat{c}_{\mathfrak{a}}, \widehat{\mathbf{m}}_{\mathfrak{a}}, \mathbf{T}_{\mathfrak{a}}, \epsilon, \mathbf{q}\}$ in (A.6)-(A.10) supplementary relations must be provided which take account of the specific material considered. This is done in the constitutive modelling.

Constitutive Functionals

As was noted at the beginning, the results presented in the following differ in two respects from MÜLLER's paper [71]. First, the constitutive functionals are valid for a mixture of $\mathfrak{N}$ constituents with $\mathfrak{N} > 2$. Second, chemical reactions are admitted, *i.e.* $\widehat{c}_{\mathfrak{a}} \neq 0$. Before proceeding with the constitutive modelling, the form of the entropy inequality must be discussed. In the present case, the entropy inequality takes the form

$$\dot{\overline{(\rho\eta)}} + \operatorname{div}(\rho\eta\mathbf{v} + \mathbf{\Phi}) \geq 0 \ , \tag{A.13}$$

in which η and $\mathbf{\Phi}$ represent the entropy density of the mixture, and the flux of entropy through the surface, respectively. The entropy supply density does not appear in (A.13) due to the earlier neglect of the external heat supply density in the conservation law of energy (A.10). More convenient forms of the entropy inequality for use in the COLEMAN-NOLL procedure are derived by employing the following definitions

$$\psi \equiv \epsilon - \theta\eta \ , \tag{A.14}$$

$$\mathbf{k} \equiv \mathbf{\Phi} - \frac{\mathbf{q}}{\theta} - \frac{1}{\theta} \sum_{\mathfrak{a}=1}^{\mathfrak{N}} \mathbf{T}_{\mathfrak{a}} \mathbf{u}_{\mathfrak{a}} \ . \tag{A.15}$$

The quantity ψ in (A.14) is known as the free energy. $\mathbf{k}$ in (A.15) denotes the modified entropy flux. What distinguishes MÜLLER's theory from all earlier attempts of constructing a unifying theory for mixtures of fluids is the fact that the entropy flux is not *a priori* re-

lated to the heat flux. Instead, it is determined by the COLEMAN-NOLL procedure which also restricts the functionals for $\{\widehat{c}_\mathfrak{a}, \widehat{\mathbf{m}}_\mathfrak{a}, \mathbf{T}_\mathfrak{a}, \epsilon, \mathbf{q}\}$, see point 9 of the principles underlying this theory. In MÜLLER's theory these functionals are written as ordinary functions of

$$\rho_\mathfrak{b}, \quad \mathbf{d}_\mathfrak{b}, \quad \mathbf{v}_\mathfrak{b}, \quad \operatorname{grad}\mathbf{v}_\mathfrak{b}, \quad \theta, \quad \mathbf{g}\ , \quad \mathfrak{b}=1,2,\ldots,\mathfrak{N}\ , \tag{A.16}$$

which respects the principle of local action and determinism (point 5 and 6). By also applying the principle of material objectivity the constitutive functionals reduce to isotropic tensor functions of

$$\rho_\mathfrak{b}, \quad \mathbf{d}_\mathfrak{b}, \quad \mathbf{v}_{\mathfrak{b}\mathfrak{N}}, \quad \mathbf{D}_\mathfrak{b}, \quad \theta, \quad \mathbf{g}\ , \quad \mathfrak{b}=1,2,\ldots,\mathfrak{N}\ , \tag{A.17}$$

for which representation theorems were worked out by SMITH [89]. In principle, it is also possible to admit differences of the skew symmetric part of the tensors $\operatorname{grad}\mathbf{v}_\mathfrak{a}$ as objective combinations in the list (A.17). This is, however, not necessary since the mixture theory applies only to non-polar constituents. It is an important feature of MÜLLER's theory that density gradients are admitted in the list of independent constitutive functions (A.16) as this represents an important generalisation of classical thermochemistry. From here on, one proceeds with the COLEMAN-NOLL procedure, which is a rather lengthy process. It is thus refrained from giving a detailed account of the derivation and the reader is instead encouraged to consult [71] for guidance. The idea behind the COLEMAN-NOLL procedure is that the entropy inequality (A.13) must be fulfilled for all admissible thermo-kinematical processes, *i.e.* those processes $\{\widehat{c}_\mathfrak{a}, \widehat{\mathbf{m}}_\mathfrak{a}, \mathbf{T}_\mathfrak{a}, \epsilon, \mathbf{q}\}$ which satisfy the balance equations listed in Table 1.1. For non-linear constitutive functionals the entropy inequality is fulfilled if the following conditions hold

1.) The free energy is a potential for the entropy

$$\eta = -\frac{\partial\psi}{\partial\theta}\ . \tag{A.18}$$

2.) The free energy is independent of the functions $\mathbf{g}$ and $\mathbf{D}_\mathfrak{a}$, and takes the form

$$\psi = \psi_I\left(\theta, \rho_\mathfrak{a}, \mathbf{d}_\mathfrak{a}\right) + \frac{1}{2}\sum_{\mathfrak{a}=1}^{\mathfrak{N}}\left(c_\mathfrak{a}\mathbf{u}_\mathfrak{a}\cdot\mathbf{u}_\mathfrak{a}\right)\ , \tag{A.19}$$

where ψ_I is the *inner part of the free energy.*

3.) The following differential equations must be satisfied

$$\mathbf{0} = \operatorname{sym}\left\{\frac{\partial\mathbf{k}}{\partial\mathbf{g}} - \frac{\rho}{\theta}\sum_{\mathfrak{a}=1}^{\mathfrak{N}}\left(\frac{\partial\psi_I}{\partial\mathbf{d}_\mathfrak{b}}\otimes\frac{\partial\widehat{c}_\mathfrak{b}}{\partial\mathbf{g}}\right)\right\}\ , \tag{A.20}$$

$$\mathbf{0} = \operatorname{sym}\left\{\frac{\partial}{\partial\mathbf{d}_\mathfrak{a}}\left(\mathbf{k} + \frac{\rho}{\theta}\psi_I\mathbf{u}_\mathfrak{a}\right) - \frac{\rho}{\theta}\sum_{\mathfrak{b}=1}^{\mathfrak{N}}\left(\frac{\partial\psi_I}{\partial\mathbf{d}_\mathfrak{b}}\otimes\frac{\partial\widehat{c}_\mathfrak{b}}{\partial\mathbf{d}_\mathfrak{a}}\right)\right\}\ , \tag{A.21}$$

$$\mathbf{0} = \operatorname{skw}\left\{\frac{\partial\mathbf{k}}{\partial\mathbf{v}_{\mathfrak{b}\mathfrak{N}}} - \frac{\rho}{\theta}\sum_{\mathfrak{a}=1}^{\mathfrak{N}}\left(\frac{\partial\widehat{c}_\mathfrak{a}}{\partial\mathbf{v}_{\mathfrak{b}\mathfrak{N}}}\otimes\frac{\partial\psi_I}{\partial\mathbf{d}_\mathfrak{a}}\right)\right\}\ , \tag{A.22}$$

$$\mathbf{0} = \frac{\partial}{\partial\mathbf{D}_\mathfrak{a}}\otimes\mathbf{k} + \frac{\rho\rho_\mathfrak{a}}{\theta}\mathbf{I}\otimes\frac{\partial\psi_I}{\partial\mathbf{d}_\mathfrak{a}} - \frac{\rho}{\theta}\sum_{\mathfrak{b}=1}^{\mathfrak{N}}\left(\frac{\partial\widehat{c}_\mathfrak{b}}{\partial\mathbf{D}_\mathfrak{a}}\otimes\frac{\partial\psi_I}{\partial\mathbf{d}_\mathfrak{b}}\right)\ , \tag{A.23}$$

where ($\mathfrak{a} = 1, 2, \ldots, \mathfrak{N}$) and ($\mathfrak{b} = 1, 2, \ldots, \mathfrak{N}-1$) for the free indices. skw $\{\cdot\}$ denotes the skew-symmetric part of $\{\cdot\}$.

A simplified set of restrictions is obtained when the constitutive functionals, $\mathfrak{F}_{(\cdot)}$, for $\{\widehat{c}_\mathfrak{a}, \widehat{\mathbf{m}}_\mathfrak{a}, \mathbf{T}_\mathfrak{a}, \epsilon, \mathbf{q}\}$ are made explicit by assuming a linear dependence on the independent constitutive quantities (A.17). This implies that these constitutive functionals may not be applicable when processes far from equilibrium are considered. It seems rather questionable to apply linear constitutive functionals in the modelling of the secondary instability observed in YANG *et al.* [108]'s experiment. For the present purpose, it is sufficient to describe flames with linear constitutive functionals. With the help of the representation theorems by SMITH [89], and by dropping bilinear and trilinear combinations of (A.17), the functionals can be written in the form

$$\mathfrak{F}_{\widehat{c}_\mathfrak{a}}\{\theta,\ \mathbf{g},\ \rho_\mathfrak{b},\ \mathbf{d}_\mathfrak{b},\ \mathbf{v}_{\mathfrak{b}\mathfrak{N}}, \mathbf{D}_\mathfrak{b}\} = \widehat{c}_\mathfrak{a}(\theta, \rho_\mathfrak{b}) \ , \tag{A.24}$$

$$\mathfrak{F}_{\widehat{\mathbf{m}}_\mathfrak{a}}\{\theta,\ \mathbf{g},\ \rho_\mathfrak{b},\ \mathbf{d}_\mathfrak{b},\ \mathbf{v}_{\mathfrak{b}\mathfrak{N}}, \mathbf{D}_\mathfrak{b}\} = -m^\theta_\mathfrak{a}\mathbf{g} - \sum_{\mathfrak{b}=1}^{\mathfrak{N}} m^\rho_{\mathfrak{a}\mathfrak{b}}\mathbf{d}_\mathfrak{b} - \sum_{\mathfrak{b}=1}^{\mathfrak{N}-1} m^v_{\mathfrak{a}\mathfrak{b}}\mathbf{v}_{\mathfrak{b}\mathfrak{N}} \ , \tag{A.25}$$

$$\mathfrak{F}_{\mathbf{T}_\mathfrak{a}}\{\theta,\ \mathbf{g},\ \rho_\mathfrak{b},\ \mathbf{d}_\mathfrak{b},\ \mathbf{v}_{\mathfrak{b}\mathfrak{N}}, \mathbf{D}_\mathfrak{b}\} = -\pi_\mathfrak{a}\mathbf{I} + \sum_{\mathfrak{b}=1}^{\mathfrak{N}} [\xi_{\mathfrak{a}\mathfrak{b}}\mathrm{tr}(\mathbf{D}_\mathfrak{b})\mathbf{I} + 2\zeta_{\mathfrak{a}\mathfrak{b}}\mathbf{D}_\mathfrak{b}] \ , \tag{A.26}$$

$$\mathfrak{F}_\psi\{\theta,\ \mathbf{g},\ \rho_\mathfrak{b},\ \mathbf{d}_\mathfrak{b},\ \mathbf{v}_{\mathfrak{b}\mathfrak{N}}, \mathbf{D}_\mathfrak{b}\} = \psi(\theta, \rho_\mathfrak{b}) \ , \tag{A.27}$$

$$\mathfrak{F}_\mathbf{q}\{\theta,\ \mathbf{g},\ \rho_\mathfrak{b},\ \mathbf{d}_\mathfrak{b},\ \mathbf{v}_{\mathfrak{b}\mathfrak{N}}, \mathbf{D}_\mathfrak{b}\} = -q_\theta\mathbf{g} - \sum_{\mathfrak{b}=1}^{\mathfrak{N}} q^\rho_\mathfrak{b}\mathbf{d}_\mathfrak{b} - \sum_{\mathfrak{b}=1}^{\mathfrak{N}-1} q^v_\mathfrak{b}\mathbf{v}_{\mathfrak{b}\mathfrak{N}} \ , \tag{A.28}$$

$$\mathfrak{F}_\eta\{\theta,\ \mathbf{g},\ \rho_\mathfrak{b},\ \mathbf{d}_\mathfrak{b},\ \mathbf{v}_{\mathfrak{b}\mathfrak{N}}, \mathbf{D}_\mathfrak{b}\} = \eta(\theta, \rho_\mathfrak{b}) \ , \tag{A.29}$$

$$\mathfrak{F}_\mathbf{k}\{\theta,\ \mathbf{g},\ \rho_\mathfrak{b},\ \mathbf{d}_\mathfrak{b},\ \mathbf{v}_{\mathfrak{b}\mathfrak{N}}, \mathbf{D}_\mathfrak{b}\} = k_\theta\mathbf{g} + \sum_{\mathfrak{b}=1}^{\mathfrak{N}} k^\rho_\mathfrak{b}\mathbf{d}_\mathfrak{b} + \sum_{\mathfrak{b}=1}^{\mathfrak{N}-1} k^v_\mathfrak{b}\mathbf{v}_{\mathfrak{b}\mathfrak{N}} \ . \tag{A.30}$$

The coefficients $\pi_\mathfrak{a}$, $\xi_{\mathfrak{a}\mathfrak{b}}$, $\zeta_{\mathfrak{a}\mathfrak{b}}$, $m^\theta_\mathfrak{a}$, $m^\rho_{\mathfrak{a}\mathfrak{b}}$, $m^v_{\mathfrak{a}\mathfrak{b}}$, q_θ, $q^\rho_\mathfrak{b}$, $q^v_\mathfrak{b}$, k_θ, $k^\rho_\mathfrak{b}$ and $k^v_\mathfrak{b}$ in (A.24)-(A.30) are allowed to depend on $(\theta, \rho_\mathfrak{b})$. It is worth noting that the mathematical consequences of the principles $4-7$ alone produce quite explicit forms of the constitutive functionals. Equations (A.24)-(A.30) account for the phenomena of heat conduction, viscosity, chemical reaction and diffusion, albeit in the linear regime. The coefficients $\pi_\mathfrak{a}$, $\xi_{\mathfrak{a}\mathfrak{b}}$, $\zeta_{\mathfrak{a}\mathfrak{b}}$ and q_θ are already familiar from the NAVIER-STOKES theory for single fluids, and represent the partial pressures, coefficients of viscosity and heat conductivity, respectively. Another well appreciated feature of the above set of equations is the occurrence of the coefficients $m^\theta_\mathfrak{a}$ and $q^v_\mathfrak{b}$ representing diffusion due to temperature gradients and conduction of heat due to relative velocities, respectively. Such cross-effects have been proposed by ECKART [36] in his linear irreversible thermodynamics of mixtures of fluids. Here they are a consequence of the principles $4-7$ consistent with ECKART [36]'s work. In the modelling of flames one may neglect diffusion due to temperature gradients because it was found to have relatively little influence on the structure of the flame layer except in some special circumstances, such as lean hydrogen-air flames [45]. The above constitutive functionals are also consistent with the mechanical theory of diffusion by TRUESDELL [96] since the momentum supplies are proportional to the relative velocities. In Ordinary Thermodynamics the constitutive functionals for the partial stresses are replaced by the constitutive functional for the total stress, which has essentially the same form as the partial pressures, but employs mixture coefficients.

In the linear theory, equation (A.19) implies that the free energy is a function of $(\theta, \rho_{\mathfrak{b}})$ only, since the diffusive contribution is quadratic in the diffusion velocities. Hence,

$$\psi = \psi_I(\theta, \rho_{\mathfrak{b}}) = \psi(\theta, \rho_{\mathfrak{b}}) \ , \ (\mathfrak{b} = 1, 2, \ldots, \mathfrak{N}) \ , \tag{A.31}$$

and through (A.18) and (A.14)

$$\eta = \eta(\theta, \rho_{\mathfrak{b}}) = -\frac{\partial \psi_I(\theta, \rho_{\mathfrak{b}})}{\partial \theta} = -\frac{\partial \psi(\theta, \rho_{\mathfrak{b}})}{\partial \theta} \ , \tag{A.32}$$

$$\epsilon = \epsilon(\theta, \rho_{\mathfrak{b}}) = \psi(\theta, \rho_{\mathfrak{b}}) + \theta\eta(\theta, \rho_{\mathfrak{b}}) \ , \tag{A.33}$$

respectively. The restrictions (A.20)-(A.22) upon the modified entropy flux $\mathbf{k}$ reduce to

$$\left.\begin{aligned} \operatorname{sym}\left(\frac{\partial \mathbf{k}}{\partial \mathbf{g}}\right) &= \mathbf{0} \ , \\ \operatorname{sym}\left(\frac{\partial \mathbf{k}}{\partial \mathbf{d}_{\mathfrak{a}}}\right) &= \mathbf{0} \ , \\ \operatorname{skw}\left(\frac{\partial \mathbf{k}}{\partial \mathbf{v}_{\mathfrak{a}\mathfrak{N}}}\right) &= \mathbf{0} \ , \end{aligned}\right\} \tag{A.34}$$

which are satisfied if the coefficients in the constitutive functional (A.30) are $k_\theta = 0$, $k^\rho_{\mathfrak{b}} = 0$ and $k^v_{\mathfrak{b}} \neq 0$. The restriction (A.23) is identically satisfied in the linear theory. Thus the modified entropy flux takes the reduced form

$$\mathbf{k} = \sum_{\mathfrak{b}=1}^{\mathfrak{N}-1} k^v_{\mathfrak{b}} \mathbf{v}_{\mathfrak{b}\mathfrak{N}} \ . \tag{A.35}$$

The above result (A.35) shows that the Coleman-Noll procedure can be, in fact, exploited to *derive* an explicit expression for the entropy flux rather than relating it *a priori* to the energy flux. Additional relations restricting the constitutive functionals are obtained if further conclusions are drawn from the residual entropy inequality which remains after the above conditions are satisfied. This is done by considering the equilibrium state of the mixture.

Equilibrium properties

First, the equilibrium state for the theory of non-linear constitutive functionals is discussed. This is followed by addressing what the equilibrium state implies for the linear theory. An excellent treatment of equilibrium states in mixtures with chemical reaction is given by Bowen [14, 15] and the same approach is used here to derive additional restrictions upon the constitutive functionals. The residual entropy inequality is a function of the same arguments as the constitutive functionals (A.17), and may be denoted as

$$\sigma_\eta \left(\rho_{\mathfrak{a}}, \mathbf{d}_{\mathfrak{a}}, \mathbf{v}_{\mathfrak{a}\mathfrak{N}}, \mathbf{D}_{\mathfrak{a}}, \theta, \mathbf{g}\right) \geq 0 \ . \tag{A.36}$$

The mixture is said to be in an equilibrium state if

$$\left.\begin{aligned} \mathbf{g} &= \mathbf{0} \ , \\ \mathbf{d}_{\mathfrak{a}} &= \mathbf{0} \ , \quad (\mathfrak{a} = 1, 2, \ldots, \mathfrak{N}) \ , \\ \mathbf{v}_{\mathfrak{a}\mathfrak{N}} &= \mathbf{0} \ , \quad (\mathfrak{a} = 1, 2, \ldots, \mathfrak{N} - 1) \ , \\ \mathbf{D}_{\mathfrak{a}} &= \mathbf{0} \ , \quad (\mathfrak{a} = 1, 2, \ldots, \mathfrak{N}) \ , \end{aligned}\right\} \tag{A.37}$$

holds. Moreover, it is assumed that there exists at least one temperature θ°, and $\mathfrak{N}$ densities $\rho_{\mathfrak{b}}^\circ$ such that

$$\sum_{\mathfrak{a}=1}^{\mathfrak{N}} \left(\rho \frac{\partial \psi}{\partial \rho_{\mathfrak{a}}} \widehat{c}_{\mathfrak{a}} \right) \Big|^\circ = 0 \ . \tag{A.38}$$

The symbol $(\cdot)^\circ$ denotes the equilibrium value (weak equilibrium) of $(\cdot)$. The sextuple $(\theta^\circ, \mathbf{0}, \rho_{\mathfrak{b}}^\circ, \mathbf{0}, \mathbf{0}, \mathbf{0})$ arising from (A.37) and (A.38) represents the equilibrium state. This implies that the mixture is at rest in equilibrium. By introducing the *intrinsic chemical potentials* known from classical thermochemistry

$$\mu_{\mathfrak{a}}^I \equiv \frac{\partial(\rho \psi_I)}{\partial \rho_{\mathfrak{a}}} \ , \ (\mathfrak{a} = 1, 2, \ldots, \mathfrak{N}) \ , \tag{A.39}$$

and the functional relationship between the chemical source terms $\widehat{c}_{\mathfrak{a}}$ and reaction rate densities $\widehat{j_a}$

$$\widehat{c}_{\mathfrak{a}} = \rho M_{\mathfrak{a}} \sum_{c=1}^{\mathfrak{N}-C} P_c^{\mathfrak{a}} \widehat{j}_c \ , \ (\mathfrak{a} = 1, 2, \ldots, \mathfrak{N}) \ , \tag{A.40}$$

one can rewrite (A.38) in a form which is more familiar from classical thermochemistry

$$\sum_{\mathfrak{a}=1}^{\mathfrak{N}} \sum_{c=1}^{\mathfrak{N}-C} \left(P_c^{\mathfrak{a}} M_{\mathfrak{a}} \mu_{\mathfrak{a}}^I \widehat{j}_c \right) \Big|^\circ = 0 \ . \tag{A.41}$$

The quantities $M_{\mathfrak{a}}$ and $P_c^{\mathfrak{a}}$ in (A.40) denote the molecular weight of the $\mathfrak{a}$th constituent and the stoichiometric matrix with the dimensions $(\mathfrak{N} - C) \times \mathfrak{N}$ and the rank $\mathfrak{N} - C$. C denotes the rank of the matrix representing the number of moles of the ath atomic substance in one mole of the $\mathfrak{a}$th molecular substance [16]. According to [16] there are two choices which achieve the result (A.41). First, it can be assumed that

$$\widehat{j_c}^\circ = \widehat{j_c}\,(\theta^\circ, \mathbf{0}, \rho_{\mathfrak{b}}^\circ, \mathbf{0}, \mathbf{0}, \mathbf{0}) = 0 \ , \tag{A.42}$$

for $(c = 1, 2, \ldots, \mathfrak{N} - C)$ and $(\mathfrak{b} = 1, 2, \ldots, \mathfrak{N})$. The second choice to satisfy (A.41) is to require

$$\sum_{\mathfrak{a}=1}^{\mathfrak{N}} \left(P_c^{\mathfrak{a}} M_{\mathfrak{a}} \mu_{\mathfrak{a}}^I \right) \Big|^\circ = 0 \ , \ (c = 1, 2, \ldots, \mathfrak{N} - C) \ , \tag{A.43}$$

which represents the *law of mass action*. For a given temperature θ° the conditions (A.43) impose $\mathfrak{N} - C$ constraints on the equilibrium values $\rho_{\mathfrak{b}}^\circ$ [72]. A state at which (A.42) holds is called a *weak equilibrium state*. When both (A.42) and (A.43) hold the mixture is said to be in a *strong equilibrium state*, which is denoted by the symbol $(\cdot)^\bullet$. It is sufficient here to report only the consequences of the weak equilibrium state as defined by (A.42).

It follows immediately that at $(\theta^\circ, \mathbf{0}, \rho_\mathfrak{b}^\circ, \mathbf{0}, \mathbf{0}, \mathbf{0})$

$$\sigma_\eta^\circ = \sigma_\eta\left(\theta^\circ, \mathbf{0}, \rho_\mathfrak{b}^\circ, \mathbf{0}, \mathbf{0}, \mathbf{0}\right) = 0\ . \tag{A.44}$$

Hence, the residual entropy inequality has a minimum at the weak equilibrium state, namely zero. This implies that its derivative must vanish and its second derivative must be positive semi-definite. These conditions place further restrictions upon the constitutive functionals and one obtains

$$0 = \sum_{\mathfrak{a}=1}^{\mathfrak{N}} \sum_{c=1}^{\mathfrak{N}-C} \left[P_c^\mathfrak{a} M_\mathfrak{a} \mu_\mathfrak{a}^I \left(\frac{\partial \widehat{j_c}}{\partial \theta} \right) \right] \Bigg|^\circ , \tag{A.45}$$

$$0 = \sum_{\mathfrak{a}=1}^{\mathfrak{N}} \sum_{c=1}^{\mathfrak{N}-C} \left[P_c^\mathfrak{a} M_\mathfrak{a} \mu_\mathfrak{a}^I \left(\frac{\partial \widehat{j_c}}{\partial \rho_\mathfrak{b}} \right) \right] \Bigg|^\circ , \tag{A.46}$$

$$-\widehat{\mathbf{m}}_\mathfrak{a}^\circ = \sum_{\mathfrak{b}=1}^{\mathfrak{N}} \sum_{c=1}^{\mathfrak{N}-C} \left[P_c^\mathfrak{b} M_\mathfrak{b} \mu_\mathfrak{b}^I \left(\frac{\partial \widehat{j_c}}{\partial \mathbf{v}_{\mathfrak{a}\mathfrak{N}}} \right) \right] \Bigg|^\circ , \tag{A.47}$$

$$\mathbf{q}^\circ = \left(\theta^2 \frac{\partial \mathbf{k}}{\partial \theta} \right) \Bigg|^\circ - \theta^\circ \left\{ \sum_{\mathfrak{a}=1}^{\mathfrak{N}} \sum_{c=1}^{\mathfrak{N}-C} \left[P_c^\mathfrak{a} M_\mathfrak{a} \left(\mu_\mathfrak{a}^I \frac{\partial \widehat{j_c}}{\partial \mathbf{g}} + \rho \frac{\partial \widehat{j_c}}{\partial \theta} \frac{\partial \psi_I}{\partial \mathbf{d}_\mathfrak{a}} \right) \right] \right\} \Bigg|^\circ , \tag{A.48}$$

$$\frac{\partial \mathbf{k}}{\partial \rho_\mathfrak{b}} \Bigg|^\circ = \frac{1}{\theta^\circ} \sum_{\mathfrak{a}=1}^{\mathfrak{N}} \sum_{c=1}^{\mathfrak{N}-C} \left[P_c^\mathfrak{a} M_\mathfrak{a} \left(\mu_\mathfrak{a}^I \frac{\partial \widehat{j_c}}{\partial \mathbf{d}_\mathfrak{b}} + \rho \frac{\partial \widehat{j_c}}{\partial \rho_\mathfrak{b}} \frac{\partial \psi_I}{\partial \mathbf{d}_\mathfrak{a}} \right) \right] \Bigg|^\circ , \tag{A.49}$$

$$-\mathbf{T}_\mathfrak{a}^\circ = \rho^\circ \rho_\mathfrak{a}^\circ \frac{\partial \psi_I}{\partial \rho_\mathfrak{a}} \Bigg|^\circ \mathbf{I} + \theta^\circ \frac{\partial \mathbf{k}}{\partial \mathbf{v}_{\mathfrak{a}\mathfrak{N}}} \Bigg|^\circ - \rho^\circ \sum_{\mathfrak{b}=1}^{\mathfrak{N}} \left(\frac{\partial \widehat{c_\mathfrak{b}}}{\partial \mathbf{v}_{\mathfrak{a}\mathfrak{N}}} \otimes \frac{\partial \psi_I}{\partial \mathbf{d}_\mathfrak{b}} \right) \Bigg|^\circ , \tag{A.50}$$

$$-\mathbf{T}_\mathfrak{N}^\circ = \rho^\circ \rho_\mathfrak{N}^\circ \frac{\partial \psi_I}{\partial \rho_\mathfrak{N}} \Bigg|^\circ \mathbf{I} + \sum_{\mathfrak{a}=1}^{\mathfrak{N}-1} \left[-\theta^\circ \frac{\partial \mathbf{k}}{\partial \mathbf{v}_{\mathfrak{a}\mathfrak{N}}} \Bigg|^\circ + \rho^\circ \sum_{\mathfrak{b}=1}^{\mathfrak{N}} \left(\frac{\partial \widehat{c_\mathfrak{b}}}{\partial \mathbf{v}_{\mathfrak{a}\mathfrak{N}}} \otimes \frac{\partial \psi_I}{\partial \mathbf{d}_\mathfrak{b}} \right) \Bigg|^\circ \right] , \tag{A.51}$$

where $(\mathfrak{a} = 1, 2, \ldots, \mathfrak{N}-1)$ and $(\mathfrak{b} = 1, 2, \ldots, \mathfrak{N})$ for the free indices. The equilibrium conditions in this generality are somewhat surprising since the supply of linear momentum and the heat flux no longer need not to vanish. In addition, (A.50) and (A.51) show that the partial stress in equilibrium is no longer solely determined by the free energy. If (A.50) is summed on $\mathfrak{a}$ from 1 to $\mathfrak{N}-1$, and added to (A.51) it follows that

$$\pi \equiv \sum_{\mathfrak{a}=1}^{\mathfrak{N}} \pi_\mathfrak{a} = -\left(\sum_{\mathfrak{a}=1}^{\mathfrak{N}-1} \mathbf{T}_\mathfrak{a}^\circ + \mathbf{T}_\mathfrak{N}^\circ \right) = \rho^\circ \sum_{\mathfrak{a}=1}^{\mathfrak{N}} \left(\rho_\mathfrak{a}^\circ \frac{\partial \psi_I}{\partial \rho_\mathfrak{a}} \Bigg|^\circ \right)\ . \tag{A.52}$$

The result can be identified as the total pressure in thermostatics, where $\pi_\mathfrak{a}$ is the partial pressure which has already been introduced in (A.26). As shown by Müller [71], if the $\mathfrak{N}$ densities $\rho_\mathfrak{b}$ in the list of independent constitutive variables of the inner part of the free energy are replaced by $(\rho, c_1, c_2, \ldots, c_{\mathfrak{N}-1})$, then the total pressure can be written in the more familiar form

$$\pi = \rho^{\circ 2} \frac{\partial \psi_I}{\partial \rho} \Bigg|^\circ \tag{A.53}$$

A closer inspection of (A.46) shows that if the matrix $[\partial \widehat{j_c}/\partial \rho_\mathfrak{b}]^T$ is assumed to be regular at $(\theta^\circ, \mathbf{0}, \rho_\mathfrak{b}^\circ, \mathbf{0}, \mathbf{0}, \mathbf{0})$ then the weak equilibrium state is necessarily a strong equilibrium

state and the results (A.45)-(A.49) reduce to

$$0 = \widehat{j_c}^{\bullet} \,, \tag{A.54}$$

$$0 = \sum_{\mathfrak{a}=1}^{\mathfrak{N}} \left(P_c^{\mathfrak{a}} M_{\mathfrak{a}} \mu_{\mathfrak{a}}^I \right) \Big|^{\bullet} \,, \tag{A.55}$$

$$\mathbf{0} = \widehat{\mathbf{m}}_{\mathfrak{a}}^{\bullet} \,, \tag{A.56}$$

$$\mathbf{q}^{\bullet} = \left(\theta^2 \frac{\partial \mathbf{k}}{\partial \theta} \right) \Big|^{\bullet} - \rho^{\bullet} \theta^{\bullet} \sum_{\mathfrak{a}=1}^{\mathfrak{N}} \left(\frac{\partial \widehat{c}_{\mathfrak{a}}}{\partial \theta} \frac{\partial \psi_I}{\partial \mathbf{d}_{\mathfrak{a}}} \right) \Big|^{\bullet} \,, \tag{A.57}$$

$$\frac{\partial \mathbf{k}}{\partial \rho_{\mathfrak{b}}} \Big|^{\bullet} = \frac{\rho^{\bullet}}{\theta^{\bullet}} \sum_{\mathfrak{a}=1}^{\mathfrak{N}} \left(\frac{\partial \widehat{c}_{\mathfrak{a}}}{\partial \rho_{\mathfrak{b}}} \frac{\partial \psi_I}{\partial \mathbf{d}_{\mathfrak{a}}} \right) \Big|^{\bullet} \,, \tag{A.58}$$

where again ($\mathfrak{a} = 1, 2, \ldots, \mathfrak{N}-1$) and ($\mathfrak{b} = 1, 2, \ldots, \mathfrak{N}$), and ($c = 1, 2, \ldots, \mathfrak{N} - C$) for the free indices. The results (A.50)-(A.53) are also valid in a strong equilibrium state. The distinction between weak and strong equilibrium is an important one in the modelling of flames. The upstream side (*unburnt side*) of a flame propagating in a mixture at rest is in weak equilibrium, *i.e.* vanishing reaction rates, but non-vanishing chemical affinities, while the downstream side (*burnt side*) is in a strong equilibrium state, *i.e.* both the reaction rates and chemical affinities vanish. This is why chemical reactions on the unburnt side of the flame are solely inhibited through low temperatures.

In the linear theory the conditions (A.45)-(A.51) reduce to

$$0 \geq \sum_{\mathfrak{a}=1}^{\mathfrak{N}} \sum_{c=1}^{\mathfrak{N}-C} \left[P_c^{\mathfrak{a}} M_{\mathfrak{a}} \left(2 \frac{\partial \mu_{\mathfrak{a}}}{\partial \theta} \frac{\partial \widehat{j_c}}{\partial \theta} + \mu_{\mathfrak{a}} \frac{\partial^2 \widehat{j_c}}{\partial \theta^2} \right) \right] \Big|^{\circ} \,, \tag{A.59}$$

$$[\gamma_{\mathfrak{a}\mathfrak{b}}] \text{ negative semi-definite} \,, \tag{A.60}$$

$$k_{\mathfrak{a}}^{v\circ} = \left[\frac{1}{\theta} \left(\pi_{\mathfrak{a}} - \rho_{\mathfrak{a}} \mu_{\mathfrak{a}} + \rho_{\mathfrak{a}} \psi \right) \right] \Big|^{\circ} \,, \tag{A.61}$$

$$\sum_{\mathfrak{a}=1}^{\mathfrak{N}-1} k_{\mathfrak{a}}^{v\circ} = \left[\frac{1}{\theta} \left(-\pi_{\mathfrak{N}} + \rho_{\mathfrak{N}} \mu_{\mathfrak{N}} - \rho_{\mathfrak{N}} \psi \right) \right] \Big|^{\circ} \,, \tag{A.62}$$

$$\left[\xi_{\mathfrak{a}\mathfrak{b}} + \tfrac{2}{3} \zeta_{\mathfrak{a}\mathfrak{b}} \right] \Big|^{\circ} \text{ positive semi-definite} \,, \tag{A.63}$$

$$[\zeta_{\mathfrak{a}\mathfrak{b}}] \Big|^{\circ} \text{ positive semi-definite} \,, \tag{A.64}$$

$$[m_{\mathfrak{a}\mathfrak{b}}^{v}] \Big|^{\circ} \text{ positive semi-definite} \,, \tag{A.65}$$

$$m_{\mathfrak{a}\mathfrak{b}}^{\rho\,\circ} = \left[\rho_{\mathfrak{a}} \frac{\partial \mu_{\mathfrak{a}}}{\partial \rho_{\mathfrak{b}}} - \frac{\partial \pi_{\mathfrak{a}}}{\partial \rho_{\mathfrak{b}}} \right] \Big|^{\circ} \,, \tag{A.66}$$

$$q_\theta{}^{\circ} \geq 0 \,, \tag{A.67}$$

$$q_{\mathfrak{a}}^{\rho\circ} = 0 \,, \tag{A.68}$$

where in (A.60) each element of the $\mathfrak{N} \times \mathfrak{N}$ matrix $[\gamma_{\mathfrak{a}\mathfrak{b}}]$ is given by

$$\gamma_{\mathfrak{a}\mathfrak{b}} = \sum_{\mathfrak{d}=1}^{\mathfrak{N}} \sum_{c=1}^{\mathfrak{N}-C} \left[P_c^{\mathfrak{d}} M_{\mathfrak{d}} \left(\frac{\partial \mu_{\mathfrak{d}}}{\partial \rho_{\mathfrak{b}}} \frac{\partial \widehat{j_c}}{\partial \rho_{\mathfrak{a}}} + \frac{\partial \mu_{\mathfrak{d}}}{\partial \rho_{\mathfrak{a}}} \frac{\partial \widehat{j_c}}{\partial \rho_{\mathfrak{b}}} + \mu_{\mathfrak{d}} \frac{\partial^2 \widehat{j_c}}{\partial \rho_{\mathfrak{a}} \partial \rho_{\mathfrak{b}}} \right) \right] \Big|^{\circ} \,. \tag{A.69}$$

A commonly used ansatz for the reaction rate densities, which is compatible with the law

of mass action (A.43), is

$$\widehat{j}_c = \widehat{j}_c^{\,f} - \widehat{j}_c^{\,b} = k_c(\theta) \prod_{\mathfrak{a}=1}^{\mathfrak{N}} n_{\mathfrak{a}}^{\beta_{\mathfrak{a}}^c} - k_c'(\theta) \prod_{\mathfrak{a}=1}^{\mathfrak{N}} n_{\mathfrak{a}}^{\gamma_{\mathfrak{a}}^c} \ , \tag{A.70}$$

where the exponents $\beta_{\mathfrak{a}}^c$ and $\gamma_{\mathfrak{a}}^c$ are some real numbers, and k_c and k_c' denote the rate constant for the forward and backward reaction, respectively. In addition, $n_{\mathfrak{a}}$ is the molar concentration

$$n_{\mathfrak{a}} = \rho \frac{c_{\mathfrak{a}}}{M_{\mathfrak{a}}} \ . \tag{A.71}$$

The temperature dependence of the rate constants is usually given by the empirical expressions

$$k_c(\theta) = A_c(\theta) \exp\left(-\frac{E_c}{R\theta}\right) , \qquad \text{and} \qquad k_c'(\theta) = A_c'(\theta) \exp\left(-\frac{E_c'}{R\theta}\right) , \tag{A.72}$$

where R denotes the universal gas constant. This form of the rate constants was proposed by Arrhenius, and is supported by arguments from kinetic theory. E_c is referred to as the *activation energy*, and A_c as the *pre-exponential factor*. As pointed out by Bowen [16] and Müller [71], the results (A.59)-(A.68) are only necessary conditions for the residual entropy inequality to attain a minimum. It is not possible to derive sufficient conditions with constitutive functionals which are linear in the quantities (A.17). The heat flux and supply of linear momentum have then the final form

$$\mathbf{q} = -q_\theta \mathbf{g} - \sum_{\mathfrak{b}=1}^{\mathfrak{N}-1} q_{\mathfrak{b}}^v \mathbf{v}_{\mathfrak{b}\mathfrak{N}} \ , \qquad q_\theta \geq 0 \ , \tag{A.73}$$

$$\widehat{\mathbf{m}}_{\mathfrak{a}} = -m_{\mathfrak{a}}^\theta \mathbf{g} - \sum_{\mathfrak{b}=1}^{\mathfrak{N}} m_{\mathfrak{a}\mathfrak{b}}^\rho \mathbf{d}_{\mathfrak{b}} - \sum_{\mathfrak{b}=1}^{\mathfrak{N}-1} m_{\mathfrak{a}\mathfrak{b}}^v \mathbf{v}_{\mathfrak{b}\mathfrak{N}} \ , \qquad [m_{\mathfrak{a}\mathfrak{b}}^v] \text{ positive semi-definite} \ . \tag{A.74}$$

Both the heat flux and supplies of linear momentum vanish in a weak and strong equilibrium state. Hence, the heat flux is *caused* by temperature gradients and non-vanishing diffusion velocities, while the supplies of linear momentum are *caused* by temperature and density gradients as well as non-vanishing diffusion velocities. With the aid of (A.61), the modified entropy flux becomes

$$\mathbf{k} = \frac{1}{\theta} \sum_{\mathfrak{a}=1}^{\mathfrak{N}-1} \left[\left(\pi_{\mathfrak{a}} - \rho \rho_{\mathfrak{a}} \frac{\partial \psi}{\partial \rho_{\mathfrak{a}}} \right) \mathbf{v}_{\mathfrak{a}\mathfrak{N}} \right] \ . \tag{A.75}$$

In (A.75) the symbol $\circ$ has been dropped for brevity. The entropy flux $\mathbf{\Phi}$ is related to $\mathbf{k}$ through (A.15). If terms which are bilinear in the independent constitutive variables are dropped in the evaluation of the product $\mathbf{T}_{\mathfrak{a}}\mathbf{u}_{\mathfrak{a}}$, the entropy flux can be written as

$$\mathbf{\Phi} = \frac{\mathbf{q}}{\theta} + \frac{1}{\theta} \sum_{\mathfrak{a}=1}^{\mathfrak{N}} \sum_{\mathfrak{b}=1}^{\mathfrak{N}-1} \left[\left(\rho_{\mathfrak{a}} \rho_{\mathfrak{b}} \frac{\partial \psi}{\partial \rho_{\mathfrak{a}}} - \rho \rho_{\mathfrak{b}} \frac{\partial \psi}{\partial \rho_{\mathfrak{b}}} \right) \mathbf{v}_{\mathfrak{b}\mathfrak{N}} \right] \ . \tag{A.76}$$

The above form of the entropy flux is an extension of Müller's entropy flux to mixtures

with $\mathfrak{N} > 2$ constituents. In (A.76) it has been made use of the identity

$$\mathbf{u}_{\mathfrak{a}} = \sum_{\mathfrak{b}=1}^{\mathfrak{N}-1} \left[\left(\delta_{\mathfrak{a}\mathfrak{b}} - \frac{\rho_{\mathfrak{b}}}{\rho} \right) \mathbf{v}_{\mathfrak{b}\mathfrak{N}} \right] \ . \tag{A.77}$$

As expected, the entropy flux for a mixture of fluids contains a term which is associated with the heat flux of the mixture. Yet, it also contains a term which originates from diffusion and which may give rise to a non-monotone growth of entropy from the unburnt to the burnt side. Although the dependence of the material functionals on the spin differences was excluded, a non-vanishing modified entropy flux $\mathbf{k}$ was obtained, since (A.34) requires only that the skew-symmetric part of the tensor $(\partial \mathbf{k}/\partial \mathbf{v}_{\mathfrak{a}\mathfrak{N}})$ be zero. Thus even in the linear theory the equilibrium partial stresses, or partial pressures, are allowed to depend on the derivative of the modified entropy flux with respect to the relative velocities. Nothing has thus far been said about how the free energy ψ of the mixture can be evaluated from the free energies of its constituents. Any decomposition rule for ψ is admitted at the current state. MÜLLER has shown that a special form for the decomposition of ψ can be derived by omitting density gradients from the list of independent constitutive functions (A.17). This is known to lead to relations appropriate for so-called *simple mixtures of fluids* and will be investigated in the following.

Simple Mixtures of Fluids

The omission of density gradients in (A.17) leads to an additional restriction for the modified entropy flux

$$\frac{\partial \mathbf{k}}{\partial \rho_{\mathfrak{a}}} = -\frac{\rho}{\theta} \frac{\partial \psi}{\partial \rho_{\mathfrak{a}}} \mathbf{u}_{\mathfrak{a}} - \frac{1}{\rho\theta} \left(\mathbf{T} - \sum_{\mathfrak{c}=1}^{\mathfrak{N}} \mathbf{T}_{\mathfrak{c}} \right) \mathbf{u}_{\mathfrak{a}} \ . \tag{A.78}$$

The free energy in a non-linear theory for simple mixtures is given by

$$\psi = \psi_I(\theta, \rho_{\mathfrak{b}}) + \frac{1}{2} \sum_{\mathfrak{b}=1}^{\mathfrak{N}} \left(c_{\mathfrak{b}} \mathbf{u}_{\mathfrak{b}} \cdot \mathbf{u}_{\mathfrak{b}} \right) \ , \tag{A.79}$$

which, when put into (A.78), together with the symmetry of the second derivatives of the modified entropy flux with respect to the densities $\rho_{\mathfrak{a}}$, leads to differential equations for $\rho\psi_{\mathbf{I}}$, namely

$$\frac{\partial^2 (\rho\psi_I)}{\partial \rho_{\mathfrak{a}} \partial \rho_{\mathfrak{b}}} = \rho \frac{\partial^2 \psi_I}{\partial \rho_{\mathfrak{a}} \partial \rho_{\mathfrak{b}}} + \frac{\partial \psi_I}{\partial \rho_{\mathfrak{a}}} + \frac{\partial \psi_I}{\partial \rho_{\mathfrak{b}}} \ , \ (\mathfrak{a}, \mathfrak{b} = 1, 2, \ldots, \mathfrak{N}) \ . \tag{A.80}$$

The solution of these differential equations is

$$\rho\psi_I = \sum_{\mathfrak{a}=1}^{\mathfrak{N}} \rho_{\mathfrak{a}} \psi_{\mathfrak{a}}^I(\theta, \rho_{\mathfrak{a}}) \ , \tag{A.81}$$

which shows that the free energy of the mixture is the mass fraction-weighted sum of the free energies of its constituents. Moreover, the free energy of the $\mathfrak{a}$th constituent is given as a function of temperature and only its "own" density, as if completely isolated from the other constituents of the mixture. It seems therefore reasonable to assume that the

internal energy and the entropy decompose in the same way as the free energy, hence

$$\rho\epsilon_I(\theta,\rho_{\mathfrak{a}}) = \sum_{\mathfrak{a}=1}^{\mathfrak{N}} \rho_{\mathfrak{a}}\epsilon_{\mathfrak{a}}(\theta,\rho_{\mathfrak{a}}) \ , \tag{A.82}$$

$$\rho\eta(\theta,\rho_{\mathfrak{a}}) = \sum_{\mathfrak{a}=1}^{\mathfrak{N}} \rho_{\mathfrak{a}}\eta_{\mathfrak{a}}(\theta,\rho_{\mathfrak{a}}) \ . \tag{A.83}$$

When resorting to the linear theory the partial pressures take the form

$$\pi_{\mathfrak{a}} = \rho_{\mathfrak{a}}\mu_{\mathfrak{a}} - \rho_{\mathfrak{a}}\psi_{\mathfrak{a}} + s \ , \tag{A.84}$$

where $s = s(\theta)$ is an arbitrary function of temperature subject to the restrictions (A.48)-(A.51). Using the definition of the chemical potentials, one can rewrite (A.84) and obtains

$$\pi_{\mathfrak{a}}(\theta,\rho_{\mathfrak{a}}) = \rho_{\mathfrak{a}}^2\frac{\partial\psi_{\mathfrak{a}}(\theta,\rho_{\mathfrak{a}})}{\partial\rho_{\mathfrak{a}}} + s(\theta) \ . \tag{A.85}$$

Müller [71, Section 8] has shown that one can get rid of s by analysing the partial pressures in the limit $\rho_{\mathfrak{a}} \to 0$. Thus the final form of the partial pressures in a simple mixture of fluids is

$$\pi_{\mathfrak{a}} = \rho_{\mathfrak{a}}^2\frac{\partial\psi_{\mathfrak{a}}}{\partial\rho_{\mathfrak{a}}} \ . \tag{A.86}$$

The above is a well-known thermostatic result for mixtures of ideal gases. With this the modified entropy flux in a simple mixture of fluids becomes

$$\mathbf{k} = \frac{1}{\theta}\sum_{\mathfrak{a}=1}^{\mathfrak{N}-1}\left[(\rho_{\mathfrak{a}}\psi - \rho_{\mathfrak{a}}\psi_{\mathfrak{a}})\,\mathbf{v}_{\mathfrak{a}\mathfrak{N}}\right] \ . \tag{A.87}$$

Sommerfeld [90] has shown that the free energy of the $\mathfrak{a}$th constituent in a mixture of ideal gases is given by

$$\left.\begin{aligned} \psi_{\mathfrak{a}} = \psi_{\mathfrak{a}}(\theta,\rho_{\mathfrak{a}}) = h_{\mathfrak{a}}(\theta,\pi) - \frac{R\theta}{M_{\mathfrak{a}}}\left(\ln\sum_{\mathfrak{b}=1}^{\mathfrak{N}}\frac{\rho_{\mathfrak{b}}}{M_{\mathfrak{b}}} - \ln\frac{\rho_{\mathfrak{a}}}{M_{\mathfrak{a}}}\right) - \frac{R}{M_{\mathfrak{a}}}\theta \ , \\ \pi = R\theta\sum_{\mathfrak{b}=1}^{\mathfrak{N}}\frac{\rho_{\mathfrak{b}}}{M_{\mathfrak{b}}} \ , \qquad\qquad (\mathfrak{a}=1,2,\ldots,\mathfrak{N}) \ , \end{aligned}\right\} \tag{A.88}$$

in which $h_{\mathfrak{a}}$ denotes the specific free enthalpy of the $\mathfrak{a}$th constituent. This yields for the partial pressures

$$\pi_{\mathfrak{a}} = \rho_{\mathfrak{a}}\frac{R}{M_{\mathfrak{a}}}\theta \ . \tag{A.89}$$

In deriving (A.89) it was made use of [71]

$$\frac{\partial h_{\mathfrak{a}}}{\partial\pi} = \frac{R\theta}{M_{\mathfrak{a}}\pi} \ . \tag{A.90}$$

A few remarks seem appropriate to conclude this section. First, the theory just outlined does not produce concrete forms for the material coefficients in (A.24)-(A.30). Instead these must be determined by experiment or kinetic theory. However, conditions were

derived, which constrain these material coefficients in order that for all admissible thermodynamic processes $\{\widehat{c}_\mathfrak{a}, \widehat{\mathbf{m}}_\mathfrak{a}, \mathbf{T}_\mathfrak{a}, \epsilon, \mathbf{q}\}$ the entropy inequality is satisfied. To put it in NOLL's words [75], "Thus, the second law is not a restriction on the kind of processes that can occur in nature, but a restriction on the kind of material properties that physical systems occurring in nature can have." Second, when mixtures at high pressures are considered it is mandatory to include density gradients in the list of independent constitutive quantities. Thus the constitutive functionals contain material coefficients which are associated with density gradients. The free energy of the mixture cannot simply be computed as the mass fraction-weighted sum of the free energies of its constituents, but must be determined otherwise. Third, flame processes occurring near equilibrium may be described as simple mixtures of fluids with linear constitutive functionals. The free energy of the mixture is then given explicitly as the mass fraction-weighted sum of the free energies of its constituents, as is known from mixtures of ideal gases. Fourth, the major difference between MÜLLER's theory and Ordinary Thermodynamics lies in the treatment of the motion of the constituents. In MÜLLER's theory each constituent has its own velocity which is governed by its associated balance of linear momentum. Ordinary Thermodynamics, on the other hand, employs only the balance of linear momentum of the mixture. Thus, all constituents move at a common speed, the barycentric velocity. In Ordinary Thermodynamics the constitutive functionals for the total stress and the heat flux have the same form as in the NAVIER-STOKES theory for a single fluid, but employ mixture material coefficients, which are calculated by some mixing rule from the individual constituents.

A.2. Compact Finite-Difference Discretisation in 1D

The present section describes a Compact Finite-Difference (CFD) discretisation for Rational Thermodynamics (RT) in one dimension. The numerical method is developed with the goal in mind to investigate the pressure wave-flame interaction described in chapter 2. Hence, the numerical scheme is applied to the field equations of RT in a moving frame, namely

$$\frac{\partial \rho_\mathfrak{a}}{\partial t} + \frac{\partial}{\partial \xi}\left[\rho_\mathfrak{a}\left(v_\mathfrak{a} - v\right)\right] = \widehat{c}_\mathfrak{a} \ , \qquad (\mathfrak{a} = 1, 2, \ldots, \mathfrak{N}) \tag{A.91}$$

$$\frac{\partial \rho_\mathfrak{a} v_\mathfrak{a}}{\partial t} + \frac{\partial}{\partial \xi}\left[\rho_\mathfrak{a} v_\mathfrak{a}\left(v_\mathfrak{a} - v\right) - T_\mathfrak{a}\right] = \widehat{m}_\mathfrak{a} \ , \qquad (\mathfrak{a} = 1, 2, \ldots, \mathfrak{N}) \tag{A.92}$$

$$\frac{\partial \rho \epsilon}{\partial t} + \frac{\partial}{\partial \xi}\left[\rho\epsilon\left(v - v\right) + q\right] = T\frac{\partial v}{\partial \xi} \ . \tag{A.93}$$

An extension to two- and three-dimensional problems is straightforward. The spatial discretisation of (A.91)-(A.93) cannot be carried out with Discontinuous Galerkin (DG) methods, such as described in section 2.3. This is a consequence of the weak coupling at the element nodes, which requires an exact or approximate solution of the RIEMANN problem. In contrast to Ordinary Thermodynamics (OT) where all constituents move at a common velocity, namely the barycentric velocity, RT permits each constituent to move at its 'own' velocity. Two types of wave phenomena must be distinguished, the so-called *first* and *second sound*. The former consists of the joint oscillation of the mixture constituents, while in the latter they move relative to each other with no motion of the mixture as a whole. The two are coupled, but propagate at different speeds. Hence, if

the first sound is stimulated the second follows, and vice versa. Current approximate RIEMANN solvers like HARTEN, LAX and VAN LEER (HLL) or HARTEN, LAX and VAN LEER Contact (HLLC) cannot account for the second sound, which leads to stability problems in the simulation. The CFD method of LELE [62] is not based on approximate RIEMANN solvers and maintains high-order accuracy for the spatial derivatives. At present the field equations (A.91)-(A.93) are solved on a uniform grid with constant grid spacing, Δ_ξ. Non-uniform grids can be treated by either introducing an affine mapping to map the grid in physical space onto a uniform grid or deriving an expression of the first derivative which applies directly to non-uniform grids. The latter is outlined in [41]. The first derivative on the interior nodes at grid node i may be expressed as

$$\alpha \frac{\partial \mathbf{U}_h}{\partial \xi}\Big|_{i-1} + \frac{\partial \mathbf{U}_h}{\partial \xi}\Big|_{i} + \alpha \frac{\partial \mathbf{U}_h}{\partial \xi}\Big|_{i+1} = a\frac{\mathbf{U}^h_{i+1} - \mathbf{U}^h_{i-1}}{2\Delta_\xi} + b\frac{\mathbf{U}^h_{i+2} - \mathbf{U}^h_{i-2}}{4\Delta_\xi} \ . \tag{A.94}$$

$\mathbf{U}_h$ denotes the numerical approximation of the set of balanced variables, *cf.* section 2.3. By matching the TAYLOR series coefficients of various orders, relations between the coefficients α, and a and b can be derived. The first unmatched coefficient in (A.94) determines the formal truncation error of the compact finite-difference approximation. For a sixth-order accurate scheme the coefficients are

$$\alpha = \frac{1}{3} \ , \qquad a = \frac{14}{9} \ , \quad \text{and} \quad b = \frac{1}{9} \ . \tag{A.95}$$

This scheme leads to an algebraic equation system with a strictly tri-diagonal matrix which can be solved easily with the THOMAS-algorithm. One-sided boundary formulations of (A.94) together with the corresponding coefficients can be found in [40]. The diffusive fluxes are formed by successive application of the first derivative. LELE [62] has shown that the methodology for constructing discretisation schemes for the first derivative can also be used to develop filtering schemes. This is exploited here to stabilise the computed solution by removing spurious oscillations. The cutoff-wavelength of the filtering scheme is determined by the order of the filtering scheme and its coefficients. On a uniform grid the filtering scheme on the interior nodes takes the form

$$\alpha_f \overline{\mathbf{U}}^h_{i-1} + \overline{\mathbf{U}}^h_i + \alpha_f \overline{\mathbf{U}}^h_{i+1} = \sum_{n=0}^{F} \frac{a_n}{2} \left(\mathbf{U}^h_{i+n} + \mathbf{U}^h_{i-n} \right) \ , \tag{A.96}$$

in which $\overline{\mathbf{U}}^h_i$ denotes the filtered set $\mathbf{U}^h_i$. The filter coefficient, α_f, is a free parameter, but must be in the range $|\alpha_f| < 0.5$. The other filter coefficients at the interior nodes are listed in Table A.2. An explicit filter is obtained when α_f is set to zero. One-sided filtering expressions for the near-boundary nodes can also be found in [40]. However, filtering is not applied directly at the boundary nodes, since the field variables are determined by the boundary conditions for the problem under consideration. The resulting algebraic equation system can be conveniently solved using the THOMAS-algorithm. GAITONDE AND VISBAL have thoroughly investigated the spectral properties of the filtering scheme and found that the damping effect decreases with increasing order of the filtering scheme and α_f. In the present computations the tenth-order filter, F10, is used in combination with a filter coefficient of $\alpha_f = 0.3$. Filtering was applied only to the balanced variables once at the end of each time step.

Table A.2.: Filter coefficients for various orders. Source [40].

Scheme	a_0	a_1	a_2	a_3	a_4	a_5
F2	$\frac{1}{2}+\alpha_f$	$\frac{1}{2}+\alpha_f$	0	0	0	0
F4	$\frac{5}{8}+\frac{3}{4}\alpha_f$	$\frac{1}{2}+\alpha_f$	$-\frac{1}{8}+\frac{1}{4}\alpha_f$	0	0	0
F6	$\frac{11}{16}+\frac{5}{8}\alpha_f$	$\frac{15}{32}+\frac{17}{16}\alpha_f$	$-\frac{3}{16}+\frac{3}{8}\alpha_f$	0	$\frac{1}{32}-\frac{1}{16}\alpha_f$	0
F8	$\frac{93+70\alpha_f}{128}$	$\frac{7+18\alpha_f}{16}$	$\frac{-7+14\alpha_f}{32}$	$\frac{1}{16}-\frac{1}{8}\alpha_f$	$\frac{-1}{128}+\frac{1}{64}\alpha_f$	0
F10	$\frac{193+126\alpha_f}{256}$	$\frac{105+302\alpha_f}{256}$	$\frac{-15+30\alpha_f}{64}$	$\frac{45-90\alpha_f}{512}$	$\frac{-5+10\alpha_f}{256}$	$\frac{1-2\alpha_f}{512}$

Yet, filtering alone was not sufficient to stabilise the scheme enough. Kravchenko and Moin [61] have shown that aliasing errors in the simulation of the flow of compressible Navier-Stokes fluids can lead to stability problems when high-order finite difference schemes for the spatial discretisation are employed. By simulating a turbulent channel flow the authors found that such schemes become unstable when the convective terms of the balance equations, *i.e.* the left-hand sides of (A.91), (A.92), and (A.93) are written in the above given divergence form. Kravchenko and Moin found that high-order finite-difference schemes produce stable solutions when the convective terms are instead discretised in the so-called *skew-symmetric form*. Moreover, it was shown that the discretisation of the skew-symmetric form is energy-conserving, even in the presence of aliasing errors. Hence, the convective terms are here re-written in the skew-symmetric form, which leads to

$$\frac{\partial \rho_{\mathfrak{a}}}{\partial t}+\frac{\partial}{\partial \xi}\left[\rho_{\mathfrak{a}}\left(v_{\mathfrak{a}}-v\right)\right]=\widehat{c}_{\mathfrak{a}}\ , \tag{A.97}$$

$$\sqrt{\rho_{\mathfrak{a}}}\frac{\partial \sqrt{\rho_{\mathfrak{a}}}v_{\mathfrak{a}}}{\partial t}+\frac{1}{2}\left\{\frac{\partial}{\partial \xi}\left[\rho_{\mathfrak{a}}v_{\mathfrak{a}}\left(v_{\mathfrak{a}}-v\right)\right]+\rho_{\mathfrak{a}}\left(v_{\mathfrak{a}}-v\right)\frac{\partial v_{\mathfrak{a}}}{\partial \xi}\right\}=\frac{\partial T_{\mathfrak{a}}}{\partial \xi}+\widehat{m}_{\mathfrak{a}}+\frac{1}{2}\widehat{c}_{\mathfrak{a}}v_{\mathfrak{a}}\ , \tag{A.98}$$

$$\sqrt{\rho}\frac{\partial \sqrt{\rho}e}{\partial t}+\frac{1}{2}\left\{\frac{\partial}{\partial \xi}\left[\rho e\left(v-v\right)\right]+\rho\left(v-v\right)\frac{\partial e}{\partial \xi}\right\}=-\frac{\partial q}{\partial \xi}+T\frac{\partial v}{\partial \xi}+\sum_{\mathfrak{a}=1}^{\mathfrak{N}}\widehat{c}_{\mathfrak{a}}\Delta h_{\mathfrak{a}}^{0}\ , \tag{A.99}$$

where $\mathfrak{a}=1,2,\ldots,\mathfrak{N}$. Following Morinishi [70], in the derivation of (A.98) and (A.99) it was made use of the identity

$$\frac{1}{2}\left(\frac{\partial \rho\varphi}{\partial t}+\rho\frac{\partial \varphi}{\partial t}\right)=\sqrt{\rho}\frac{\partial \sqrt{\rho}\phi}{\partial t}\ , \tag{A.100}$$

to allow for integration in time with the explicit three-stage Runge-Kutta method given in (2.25), *cf.* section 2.3. Strang splitting (2.22)-(2.24) is employed in the time integration to separate the numerically stiff chemical source terms from the convection and diffusion terms. The chemical source terms are integrated with Radau5 [46] using relative and absolute tolerances of 10^{-10} and 10^{-8}, respectively. What must also be addressed from a numerical point of view is the absence of certain constituents of the mixture in parts of the computational domain, *e.g.* radical species which exist only in the flame layer. To put it in different words, the spatial extent of the region in which the mass fraction is non-zero varies from constituent to constituent, and $\mathbf{v}_{\mathfrak{a}}\rightarrow 0$ when $c_{\mathfrak{a}}\rightarrow 0$ for $\mathfrak{a}=1,2,\ldots,\mathfrak{N}$. Since the length of the computational domain is fixed and the same for all

constituents, the absence of certain mixture constituents is addressed by clipping the mass fractions at and below an *a priori* defined threshold, namely 10^{-5}. This is complemented by re-scaling the mass fractions at the end of each time step to satisfy the identity

$$\sum_{\mathfrak{a}=1}^{\mathfrak{N}} c_{\mathfrak{a}} = 1 \ . \tag{A.101}$$

Since the CFD scheme does not satisfy $\mathbf{v}_{\mathfrak{a}} \to 0$ when $c_{\mathfrak{a}} \to 0$, the velocity is set to zero explicitly when the mass fraction value is at or below the threshold. In this way artificial velocity oscillations in the neighborhood of large mass fraction gradients are also removed. The linear momentum of the $\mathfrak{a}$th constituent is then re-scaled at the end of each time step by using the linear momentum of the mixture evaluated from the unclipped partial momenta. The time step is computed by

$$\Delta_t = \min\left(0.05\frac{\mathrm{C}_c\ \Delta_\xi}{|v_{\mathfrak{a}} - v| + s_a}, 0.1\frac{\mathrm{C}_d\ \Delta_\xi^2}{\zeta_{\mathfrak{a}}}\right) \ , \tag{A.102}$$

where $\mathrm{C}_c = 0.87$, and $\mathrm{C}_d = 0.36$ for the sixth-order CFD scheme in combination with the three-step Runge-Kutta method.

B. LES-PDF method

B.1. Introductory Remarks

LES is a modelling approach to reduce the computational demand for the simulation of turbulent flows. This is achieved by application of a spatial filter with an *a priori* defined length scale to the field equations describing the fluid motion. The length scale associated with the filtering is referred to as *filter scale* in the remainder of this work. Turbulent length scales at and above the filter scale are resolved explicitly while the length scales below the filter scale are not resolved. It seems thus appropriate to speak of *resolved* and *unresolved* turbulent length scales in the context of LES. The influence which the unresolved length scales exert on the resolved length scales is represented by the so-called *closure* model. By choosing a filter scale which is smaller than the energetic, but larger than the smallest turbulent length scale (i.e. KOLMOGOROV length scale), one aims at achieving accurate predictions whilst reducing computational demand. With an appropriate choice of the filter scale one may also reduce the sensitivity of the closure model on the final solution. This immediately poses the question of how an appropriate filter scale is chosen. In the practical application of LES this was answered by choosing a reference dimension of the local grid cell as the filter scale. Hence the filter scale varies spatially and the filtered governing equations are altered when the computational grid is modified.

One of the main challenges in predicting turbulent flames accurately with LES lies in the modelling of the filtered chemical source terms. Since the primary reaction zone is not resolved within LES the filtered chemical source terms are strongly affected by the unresolved sub-filter scale fluctuations of the species mass fractions and temperature. These can be accounted for by a transport equation for the filtered one-point, one-time joint Probability Density Function (PDF) for all of the scalar quantities required to describe the chemical reactions. This is known as the PDF model. The PDF model does not assume a particular combustion regime and therefore offers a wide range of applicability, including non-premixed, and premixed, as well as stratified and spray combustion, see for example BULAT *et al.* [20] and JONES *et al.* [54–56]. There are no conceptual difficulties in incorporating detailed reaction mechanisms into the PDF method, which is particularly important in the modelling of flame oscillation.

B.2. Filtering and Filtered Governing Equations

The present section formally introduces the filtering operator briefly mentioned in the preceding section. Applied to a smooth scalar field, $\phi(\mathbf{x}, t)$, in an unbounded domain the filtering operator $\overline{(\cdot)}$ takes the form of the convolution product

$$\overline{\phi}\left(\mathbf{x}\right) = \int_{-\infty}^{+\infty} \phi\left(\boldsymbol{\xi}\right) G\left(\mathbf{x} - \boldsymbol{\xi}, \Delta\left(\mathbf{x}\right)\right) d\boldsymbol{\xi} \ , \tag{B.1}$$

where G denotes the filter kernel which may depend upon the spatial position. The filtering symbol must not be confused with the time derivative in (1.5) and (1.6) in section 1.4. As was mentioned in the preceding section, the filters in LES have only local support and are assumed to possess the following properties

1.) Linear in the argument function,

2.) Commutation of filtering and spatial differentation,
$\operatorname{grad} \int_{-\infty}^{+\infty} \phi(\boldsymbol{\xi})\, G(\mathbf{x}-\boldsymbol{\xi}, \Delta(\mathbf{x}))\, d\boldsymbol{\xi} = \int_{-\infty}^{+\infty} \operatorname{grad} \phi(\boldsymbol{\xi})\, G(\mathbf{x}-\boldsymbol{\xi}, \Delta(\mathbf{x}))\, d\boldsymbol{\xi}$,

3.) Normalisation condition, $\int_{-\infty}^{+\infty} G(\mathbf{x}-\boldsymbol{\xi}, \Delta(\mathbf{x}))\, d\boldsymbol{\xi} = 1$.

Property 2 is immediately satisfied if the filter kernel is independent of the spatial position. For a filter kernel which varies in space this is considerably more challenging to satisy. In the present case the filter scale, $\Delta(\mathbf{x})$, is set equal to the reference grid cell dimension, $\Delta = (\Delta x \Delta y \Delta z)^{\frac{1}{3}}$, and thus varies in space. By assuming small spatial variations of the filter scale the commutation error is of second or higher order. Thus the grid stretching factor everywhere in the filtering domain must be small. In practical applications, it is usually maintained below 5 %. In the treatment of compressible fluids it is common practice to define a density-weighted filter

$$\widetilde{\phi}(\mathbf{x}, t) = \frac{\overline{\rho(\mathbf{x}, t)\phi(\mathbf{x}, t)}}{\overline{\rho(\mathbf{x}, t)}} \ . \tag{B.2}$$

When this filter operation is applied to the field equations of ordinary thermodynamics (see section 1.4), one obtains

• balance of mass of the $\mathfrak{a}$th constituent

$$\frac{\partial \overline{\rho}\widetilde{c}_{\mathfrak{a}}}{\partial t} + \operatorname{div}(\overline{\rho}\widetilde{c}_{\mathfrak{a}}\widetilde{\mathbf{v}}) = \operatorname{div}\left(\frac{\overline{\mu}}{\sigma} \operatorname{grad} \overline{c}_{\mathfrak{a}}\right) - \operatorname{div} \mathbf{J}_{\mathfrak{a}} + \overline{\widehat{c}_{\mathfrak{a}}} \ , \tag{B.3}$$

• balance of mass of the mixture

$$\frac{\partial \overline{\rho}}{\partial t} + \operatorname{div}(\overline{\rho}\widetilde{\mathbf{v}}) = 0 \ , \tag{B.4}$$

• balance of linear momentum of the mixture

$$\frac{\partial \overline{\rho}\widetilde{\mathbf{v}}}{\partial t} + \operatorname{div}(\overline{\rho}\widetilde{\mathbf{v}} \otimes \widetilde{\mathbf{v}}) = -\operatorname{grad} \overline{\pi} + \operatorname{div}\left(\overline{\mathbf{V}} - \mathbf{V}_{sfs}\right) \ , \tag{B.5}$$

• balance of energy of the mixture

$$\frac{\partial \overline{\rho}\widetilde{h}}{\partial t} + \operatorname{div}\left(\overline{\rho}\widetilde{\mathbf{v}}\widetilde{h}\right) = \operatorname{div}\left(\frac{\overline{\mu}}{\sigma} \operatorname{grad} \overline{h}\right) - \operatorname{div} \mathbf{J}_h \ , \tag{B.6}$$

where $\mathbf{V}_{sfs} = \overline{\rho}\left(\widetilde{\mathbf{v} \otimes \mathbf{v}} - \widetilde{\mathbf{v}} \otimes \widetilde{\mathbf{v}}\right)$ is the *sub-filter scale stress tensor*, which is here determined by means of the SMAGORINSKY model

$$\mathbf{V}_{sfs,a} = 2\mu_{sfs}\widetilde{\mathbf{S}} \ . \tag{B.7}$$

The quantities σ, $\mu_{sfs} = \overline{\rho}(C_s\Delta)^2||\widetilde{\mathbf{S}}||$, and $\widetilde{\mathbf{S}}$ denote the SCHMIDT number, the *sub-filter scale viscosity* and the resolved rate of strain tensor $\widetilde{\mathbf{S}}$, respectively. $||\cdot||$ is the Frobenius norm. The parameter C_s is calculated using the dynamic procedure of PIOMELLI AND LIU [77]. The isotropic part of the viscous and sub-filter scale stresses is absorbed into the total pressure. The filtered mass balances and the balance of energy of the mixture contain unknown sub-filter scale fluxes, $\mathbf{J}_{\mathfrak{a}}$ and $\mathbf{J}_h$, and the filtered chemical source terms, $\overline{\widehat{c_{\mathfrak{a}}}}$. These are computed with the PDF model.

B.3. PDF Modelling

Following GAO AND O'BRIEN [42], an equation describing the evolution of the density-weighted sub-filter PDF for the species mass fractions and the enthalpy of the mixture can be derived. This equation contains unknown terms which represent the sub-filter scale transport of the PDF and sub-filter scale mixing. In the present work these are approximated by a SMAGORINSKY type gradient model and the Linear Mean Square Estimation (LMSE) closure, respectively. The modelling of the sub-filter scale mixing is difficult and no entirely satisfactory model exists. The LMSE mixing model used in the present work constitutes a reasonable choice between simplicity and predictive capabilities. With these models the sub-filter PDF transport equations for the species mass fractions and enthalpy of the mixture have the following generic form

$$\left.\begin{aligned} &\overline{\rho}\frac{\partial \widetilde{P}_{sfs}(\underline{\psi})}{\partial t} + \overline{\rho}\widetilde{\mathbf{v}}\cdot\operatorname{grad}\widetilde{P}_{sfs}(\underline{\psi}) + \sum_{\alpha=1}^{\mathfrak{N}+1}\frac{\partial}{\partial\psi_\alpha}\left[\widehat{c}_\alpha(\underline{\psi})\widetilde{P}_{sfs}(\underline{\psi})\right] \\ &= \operatorname{div}\left[\left(\frac{\mu}{\sigma}+\frac{\mu_{sfs}}{\sigma_{sfs}}\right)\operatorname{grad}\widetilde{P}_{sfs}(\underline{\psi})\right] \\ &- \frac{C_d}{\tau_{sfs}}\sum_{\alpha=1}^{\mathfrak{N}+1}\frac{\partial}{\partial\psi_\alpha}\left[\overline{\rho}\left(\psi_\alpha-\widetilde{\phi}_\alpha\right)\widetilde{P}_{sfs}(\underline{\psi})\right] \end{aligned}\right\} \tag{B.8}$$

in which $\widetilde{\phi}_\alpha$ denotes either the mass fraction of the αth constituent of the mixture or the enthalpy. The quantity $\underline{\psi}$ designates the phase space of the scalar $\widetilde{\phi}_\alpha$. In the present work the constants σ_{sfs} and $\overline{C}_d$ are set to 0.7 and 2.0, respectively. The sub-filter mixing time scale τ_{sfs} is given by

$$\tau_{sfs} = \frac{\overline{\rho}\Delta^2}{\mu+\mu_{sfs}}\ . \tag{B.9}$$

B.4. Eulerian Stochastic Field Method

The PDF transport equation (B.8) is solved using the EULERIAN stochastic field method based on an ITŌ interpretation of the stochastic integral. The PDF $\widetilde{P}_{sfs}(\underline{\psi})$ is represented by an ensemble of N_s stochastic fields for each of the species mass fractions and the enthalpy, namely $\xi_\alpha^n(\mathbf{x},t)$, with $1 \le n \le N_s$. The evolution of the EULERIAN stochastic

fields is described by

$$\left.\begin{aligned}\overline{\rho} d\xi_\alpha^n = &- \overline{\rho}\widetilde{\mathbf{v}} \cdot \operatorname{grad} \xi_\alpha^n dt + \operatorname{div}\left(\Gamma \operatorname{grad} \xi_\alpha^n\right) dt + \overline{\rho}\sqrt{\frac{2\Gamma}{\overline{\rho}}} \operatorname{grad} \xi_\alpha^n \cdot d\mathbf{W}^n \\ &- \frac{C_d \overline{\rho}}{2\tau_{sfs}} \left(\xi_\alpha^n - \widetilde{\phi}_\alpha\right) dt + \widehat{c}_\alpha^n dt \ ,\end{aligned}\right\} \tag{B.10}$$

where Γ and $d\mathbf{W}$ represent the total diffusion coefficient and the increments of a vector Wiener process which is different for each stochastic field, but independent of the spatial position. This stochastic process has no influence on the first moments (i.e. filtered mean values). The Wiener process is approximated by time-step increments $\eta_i^n \sqrt{dt}$, where η_i^n is a $\{-1, +1\}$ dichotomic vector. The solutions of (B.10) preserve any bounded properties of the scalar in question as the gradient of the scalar will tend to zero when the value of the scalar approaches extrema, and therefore the stochastic contribution will tend to zero. For a more detailed discussion of the Eulerian stochastic field method the reader should consult Sabelnikov and Soulard [85].

B.5. Flow Solver BOFFIN

The LES-PDF method briefly outlined above is implemented into the flow solver BOFFIN-LES [51, 56], which is a block-structured, boundary-conforming finite volume code with second-order discretisation schemes in space and time. The code utilises a co-located storage arrangement and is fully parallelised by means of domain decomposition and MPI message passing routines. The convective terms of the momentum balance are discretised with an energy-conserving scheme and all other spatial derivatives except for the convection terms in the scalar balance equations are discretised with second-order central differences. To avoid unphysical overshoots, a Total Variation Diminishing (TVD) scheme is used to discretise the convective terms in the scalar equations. A fractional step method is employed to solve the stochastic field equations and a Newton-method to integrate the numerically stiff chemical source terms. The numerical integration of the chemical source terms is additionally parallelised to speed up the computation.

Two versions of the flow solver are available to treat the fluid either as incompressible or compressible. In both versions the momentum and continuity equations are solved using a SIMPLE-type pressure correction method [76] to maintain an implicit time integration scheme and avoid excessively small numerical time steps when the Mach number approaches zero. The extension of the standard pressure correction method for incompressible to compressible fluids is described in [29, 102].

References

[1] Abgrall, R. and Karni, S. Computations of Compressible Multifluids. *Journal of Computational Physics*, 169:594–623, 2001.

[2] Ahmed, S. F., Balachandran, R., Marchione, T., and Mastorakos, E. Spark ignition of turbulent nonpremixed bluff-body flames. *Combustion and Flame*, 151:366–385, 2007.

[3] Angelberger, C., Veynante, D., and Egolfopoulos, F. LES of Chemical and Acoustic Forcing of a Premixed Dump Combustor. *Flow, Turbulence and Combustion*, 65: 205–222, 2000.

[4] Armitage, C. A., Balachandran, R., Mastorakos, E., and Cant, R. S. Investigation of the nonlinear response of turbulent premixed flames to imposed inlet velocity oscillations. *Combustion and Flame*, 146:419–436, 2006.

[5] Ayache, S., Dawson, J. R., Triantafyllidis, A., Balachandran, R., and Mastorakos, E. Experiments and Large-Eddy Simulations of acoustically forced bluff-body flows. *International Journal of Heat and Fluid Flow*, 31(5):754–766, 2010.

[6] Ayoola, B. *Laser-based measurement of heat release rate and temperature in turbulent premixed flames.* PhD thesis, University of Cambridge, 2005.

[7] Balachandran, R. *Experimental Investigation of the Response of Turbulent Premixed Flames to Acoustic Oscillations*. PhD thesis, University of Cambridge, 2005.

[8] Bassi, F. and Rebay, S. GMRES Discontinuous Galerkin Solution of the Compressible Navier-Stokes Equations. In *Discontinuous Galerkin Methods*. Springer, 2000.

[9] Baulch, D. L., Griffiths, J. F., Pappin, A. J., and Sykes, A. F. Third-body Interactions in the Oscillatory Oxidation of Hydrogen in a Well Stirred Flow Reactor. *Journal of the Chemical Society, Faraday Transactions 1: Physical Chemistry in Condensed Phases*, 84(5):1575–1586, 1988.

[10] Bechtel, J. H., Blint, R. J., Dasch, C. J., and Weinberger, D. A. Atmospheric Pressure Premixed Hydrocarbon-Air Flames: Theory and Experiment. *Combustion and Flame*, 42:97–213, 1981.

[11] Bertram, A. *Elasticity and Plasticity of Large Deformations*. Springer, 2005.

[12] Biswas, R., Devine, K. D., and Flaherty, J. E. Parallel, adaptive finite element methods for conservation laws. *Applied Numerical Mathematics*, 14(1-3):255–283, 1994.

[13] Bourehla, A. and Baillot, F. Appearance and Stability of a Laminar Conical Premixed Flame Subjected to an Acoustic Perturbation. *Combustion and Flame*, 114: 303–318, 1998.

[14] Bowen, R. M. Thermochemistry of Reacting Materials. *Journal of Chemical Physics*, 49(4):1625–1637, 1968.

[15] Bowen, R. M. The Thermochemistry of a Reacting Mixture of Elastic Materials with Diffusion. *Archive for Rational Mechanics and Analysis*, 34:97–127, 1969.

[16] Bowen, R. M. *Continuum Physics - Mixtures and EM Field Theories*, volume III. Academic Press, 1976.

[17] Brock, L. B., Mischler, B., Rohlfing, E. A., Bise, R. T., and Neumark, D. M. Laser-induced fluorescence spectroscopy of the ketenyl radical. *Journal of Chemical Physics*, 107(2):665–668, 1997.

[18] Brown, N. J., Fristrom, R. M., and Sawyer, R. F. A Simple Premixed Flame Model Including an Application to H_2+ Air Flames. *Combustion and Flame*, 23:269–275, 1974.

[19] Bulat, G. *Large Eddy Simulations of Reacting Swirling Flows in an Industrial Burner*. PhD thesis, Imperial College London, 2012.

[20] Bulat, G., Jones, W. P., and Marquis, A. J. Large Eddy Simulation of an industrial gas-turbine combustion chamber using the sub-grid PDF method. *Proceedings of the Combustion Institute*, 34:3155–3164, 2013.

[21] Chu, B. T. On the Energy Transfer to Small Disturbances in Fluid Flow (Part I). *Acta Mechanica*, 1(3):215–234, 1965.

[22] Coats, C. M., Chang, Z., and Williams, P. D. Excitation of thermoacoustic oscillations by small premixed flames. *Combustion and Flame*, 157:1037–1051, 2010.

[23] Coleman, B. D. and Noll, W. The Thermodynamics of Elastic Materials with Heat Conduction and Viscosity. *Archive for Rational Mechanics and Analysis*, 13(1): 167–178, 1963.

[24] Crocco, L. and Cheng, S. *Theory of Combustion Instability in Liquid Propellant Rocket Motors*. Butterworths Publications LTD., 1956.

[25] da Silva, C. B., Balarac, G., and Métais, O. Transition in high velocity ratio coaxial jets analysed from direct numerical simulations. *Journal of Turbulence*, 4(24):1–18, 2003.

[26] di Mare, F. *Large Eddy Simulation of reacting and non-reacting turbulent flows in complex geometries*. PhD thesis, Imperial College London, 2002.

[27] di Mare, L., Klein, M., Jones, W. P., and Janicka, J. Synthetic turbulence inflow conditions for large-eddy simulation. *Physics of Fluids*, 18:(025107)1–11, 2006.

[28] di Rosa, M. D., Klavuhn, K. G., and Hanson, R. K. LIF Spectroscopy of NO and O_2 in High-Pressure Flames. *Combustion Science and Technology*, 118:257–283, 1996.

[29] Distelhoff, M. Computation of Two-dimensional Compressible Flow Using TVD-Schemes. Master's thesis, Imperial College London, 1993.

[30] Docquier, N. and Candel, S. Combustion control and sensors: a review. *Progress in Energy and Combustion Science*, 28:107–150, 2002.

[31] Dowling, A. P. Nonlinear self-excited oscillations of a ducted flame. *Journal of Fluid Mechanics*, 346:271–290, 1997.

[32] Dowling, A. P. A kinematic model of a ducted flame. *Journal of Fluid Mechanics*, 394:51–72, 1999.

[33] Dowling, A. P. and Morgans, A. S. Feedback Control of Combustion Oscillations. *Annual Review of Fluid Mechanics*, 37:151–182, 2005.

[34] Duchaine, F. and Poinsot, T. Sensitivity of flame transfer functions of laminar flames. *Center for Turbulence Research*, pages 251–258, 2010. Proceedings of the Summer Program.

[35] Dunn, J. E. and Fosdick, R. L. Steady, structured shock waves. Part 1: Thermoelastic materials. *Archive for Rational Mechanics and Analysis*, 104(4):295–365, 1988.

[36] Eckart, C. The Thermodynamics of Irreversible Processes. II. Fluid Mixtures. *Physical Review Letters*, 58(3):269–275, 1940.

[37] Franzelli, B., Riber, E., Gicquel, L. Y. M., and Poinsot, T. Large Eddy Simulation of combustion instabilities in a lean partially premixed swirled flame. *Combustion and Flame*, 159:621–637, 2012.

[38] Fristrom, R. M. Flame structure studies: past, present and future. *Pure and Applied Chemistry*, 62(5):839–849, 1990.

[39] Fristrom, R. M., Grunfelder, C., and Favin, S. Methane-Oxygen Flame Structure. I. Characteristic Profiles in a Low-Pressure, Laminar, Lean, Premixed Methane-Oxygen Flame. *Journal of Physical Chemistry*, 64(10):1386–1392, 1960.

[40] Gaitonde, D. V. and Visbal, M. R. High-Order Schemes for Navier-Stokes Equations: Algorithm and Implementation into FDL3DI. Technical report, Air Force Research Laboratory, 1998.

[41] Gamet, L., Ducros, F., Nicoud, F., and Poinsot, T. Compact finite difference schemes on non-uniform meshes. Application to direct numerical simulations of compressible flows. *International Journal for Numerical Methods in Fluids*, 29: 159–191, 1999.

[42] Gao, F. and O'Brien, E. E. A large eddy simulation scheme for turbulent reacting flows. *Physics of Fluids A: Fluid Dynamics*, 5:1282–1284, 1993.

[43] Gazi, A., Vourliotakis, G., Skevis, G., and Founti, M. A. Assessment of Chemical Markers for Heat-Release Rate Correlations in Laminar Premixed Flames. *Combustion Science and Technology*, 185:1482–1508, 2013.

[44] Goldman, A., Rahinov, I., and Cheskisu, S. Molecular oxygen detection in low pressure flames using cavity ring-down spectroscopy. *Applied Physics B*, 82:659–663, 2006.

[45] Grcar, J. F., Bell, J. B., and Day, M. S. The Soret Effect in Naturally Propagating, Premixed, Lean, Hydrogen-Air Flames. *Proceedings of the Combustion Institute*, 32 (1):1173–1180, 2009.

[46] Hairer, E. and Wanner, G. *Solving Ordinary Differential Equations II.* Springer, 1991.

[47] Hall, J. M., Rickard, M. J. A., and Petersen, E. L. Comparison of Characteristic Time Diagnostics for Ignition and Oxidation of Fuel/Oxidiser Mixtures behind Reflected Shock Waves. *Combustion Science and Technology*, 177:4455–483, 2005.

[48] Hesthaven, J. S. and Warburton, T. *Nodal Discontinuous Galerkin Methods.* Springer, 2008.

[49] Huang, Y., Sung, H.-G., Hsieh, S.-Y., and Yang, V. Large-Eddy Simulation of Combustion Dynamics of Lean-Premixed Swirl-Stabilized Combustor. *Journal of Propulsion and Power*, 19(5):782–794, 2003.

[50] Huang, Y. and Yang, V. Bifurcation of flame structure in a lean-premixed swirl-stabilized combustor: transition from stable to unstable flame. *Combustion and Flame*, 136:383–389, 2004.

[51] Jones, W. P., di Mare, F., and Marquis, A. J. LES-BOFFIN: Users Guide. Technical report, Imperial College London, 2002.

[52] Jones, W. P., Jurisch, M., and Marquis, A. J. Examination of an Oscillating Flame in the Turbulent Flow Around a Bluff Body with Large Eddy Simulation Based on the Probability Density Function Method. To appear in:. *Flow, Turbulence and Combustion*, 2015.

[53] Jones, W. P. and Lindstedt, R. Global reaction schemes for hydrocarbon combustion. *Combustion and Flame*, 73(3):233–249, 1988.

[54] Jones, W. P., Marquis, A. J., and Noh, D. LES of a methanol spray flame with a stochastic sub-grid model. *Proceedings of the Combustion Institute*, 35:1685–1691, 2015.

[55] Jones, W. P., Marquis, A. J., and Prasad, V. N. LES of a turbulent premixed swirl burner using the Eulerian stochastic field method. *Combustion and Flame*, 159: 30793095, 2012.

[56] Jones, W. P. and Prasad, V. N. Large Eddy Simulation of the Sandia Flame Series (DF) using the Eulerian stochastic field method. *Combustion and Flame*, 157:1621–1636, 2010.

[57] Karniadakis, G. and Sherwin, S. *Spectral/hp Element Methods for CFD.* Oxford University Press, 1999.

[58] Kaskan, W. E. An Investigation of Vibrating Flames. *Symposium (International) on Combustion*, 4(1):575–591, 1953.

[59] Klein, M., Sadiki, A., and Janicka, J. A digital filter based generation of inflow data for spatially developing direct numerical or large eddy simulations. *Journal of Computational Physics*, 186:652–665, 2003.

[60] Kornilov, V., Rook, R., ten Thije Boonkkamp, J. H. M., and de Goey, L. P. H. Experimental and numerical investigation of the acoustic response of multi-slit Bunsen burners. *Combustion and Flame*, 156:1957–1970, 2009.

[61] Kravchenko, A. G. and Moin, P. On the Effect of Numerical Errors in Large Eddy Simulations of Turbulent Flows. *Journal of Computational Physics*, 131:310–322, 1997.

[62] Lele, S. K. Compact Finite Difference Schemes with Spectral-like Resolution. *Journal of Computational Physics*, 103:16–42, 1992.

[63] Lieuwen, T. C. Modeling Premixed Combustion-Acoustic Wave Interactions: A Review. *Journal of Propulsion and Power*, 19(5):765–781, 2003.

[64] Luo, Z., Yoo, C. S., Richardson, E. S., Chen, J. H., Law, C. K., and Lu, T. Chemical explosive mode analysis for a turbulent lifted ethylene jet flame in highly-heated coflow. *Combustion and Flame*, 159:265–274, 2012.

[65] Lv, Y. and Ihme, M. Discontinuous Galerkin method for multicomponent chemically reacting flows and combustion. *Journal of Computational Physics*, 270:105–137, 2014.

[66] Maas, U. and Warnatz, J. Ignition Processes in Hydrogen-Oxygen Mixtures. *Combustion and Flame*, 74:53–69, 1988.

[67] Martin, C. E., Benoit, L., Sommerer, Y., Nicoud, F., and Poinsot, T. Large-Eddy Simulation and Acoustic Analysis of a Swirled Staged Turbulent Combustor. *American Institute of Aeronautics and Astronautics*, 44(4):741–750, 2006.

[68] Mayer, E. W. and Powell, K. G. Similarity solutions for viscous vortex cores. *Journal of Fluid Mechanics*, 238:487–507, 1992.

[69] McBride, B. J., Zehe, M. J., and Gordon, S. NASA Glenn Coefficients for Calculating Thermodynamic Properties of Individual Species. Technical Report NASA/TP2002-211556, Glenn Research Center, Cleveland, 2002.

[70] Morinishi, Y. Skew-symmetric form of convective terms and fully conservative finite difference schemes for variable density low-Mach number flows. *Journal of Computational Physics*, 229:276–300, 2010.

[71] Müller, I. A Thermodynamic Theory of Mixtures of Fluids. *Archive for Rational Mechanics and Analysis*, 28:1–39, 1968.

[72] Müller, I. and Ruggeri, T. *Extended Thermodynamics*. Springer, 1993.

[73] Nikolaou, Z. M. and Swaminathan, N. Heat release rate markers for premixed combustion. *Combustion and Flame*, 161:3073–3084, 2014.

[74] Noiray, N., Durox, D., Schuller, T., and Candel, S. A unified framework for nonlinear combustion instability analysis based on the flame describing function. *Journal of Fluid Mechanics*, 615:139–167, 2008.

[75] Noll, W. Thoughts on Thermomechanics. Technical report, Carnegie Mellon University, 2010.

[76] Patankar, S. V. and Spalding, D. B. A calculation procedure for heat, mass and momentum transfer in three-dimensional parabolic flows. *International Journal of Heat and Mass Transfer*, 15(10):1787–1806, 1972.

[77] Piomelli, U. and Liu, J. Large eddy simulation of rotating channel flows using a localized dynamic model. *Physics of Fluids*, 7:839–848, 1995.

[78] Poinsot, T. and Veynante, D. *Theoretical and Numerical Combustion*. Edwards, 2001.

[79] Poling, B. E., Prausnitz, J. M., and O' Connell, J. *The Properties of Gases and Liquids*. McGraw-Hill, 5th edition, 2000.

[80] Prigogine, I. and Nicolis, G. Biological order, structure and instabilities. *Quaterly Reviews of Biophysic*, 4:107–148, 1971.

[81] Rayleigh, J. W. S. *The Theory of Sound, Vol. 2*. Macmillan and Co., Ltd., 1896.

[82] Ruder, H., Ertl, T., Geyer, F., Herold, H., and Kraus, U. Line-of-sight integration: A powerful tool for visualisation of three-dimensional scalar fields. *Computers & Graphics*, 13(2):223–228, 1989.

[83] Rudy, D. H. and Strikwerda, J. C. A Nonreflecting Outflow Boundary Condition for Subsonic Navier-Stokes Calculation. *Journal of Computational Physics*, 36:55–70, 1980.

[84] Rudy, D. H. and Strikwerda, J. C. Boundary Conditions for Subsonic Compressible Navier-Stokes Calculation. *Computers and Fluids*, 9:327–338, 1981.

[85] Sabelnikov, V. and Soulard, O. Rapidly decorrelating velocity-field model as a tool for solving one-point Fokker-Planck equations for probability density functions of turbulent reactive scalars. *Physical Review E*, 72:016301(1–22), 2005.

[86] Searby, G. Acoustic Instability in Premixed Flames. *Combustion Science and Technology*, 81(4-6):221–231, 1992.

[87] Searby, G. and Rochwerger, D. A parametric acoustic instability in premixed flames. *Journal of Fluid Mechanics*, 231:529–543, 1991.

[88] Selle, L., Lartigue, G., Poinsot, T., Koch, R., Schildmacher, K.-U., Krebs, W., Prade, B., Kaufmann, P., and Veynante, D. Compressible large eddy simulation of turbulent combustion in complex geometry on unstructured meshes. *Combustion and Flame*, 137:489–505, 2004.

[89] Smith, G. F. On isotropic integrity bases. *Archive for Rational Mechanics and Analysis*, 18(4):282–292, 1965.

[90] Sommerfeld, A. *Thermodynamics and Statistical Mechanics*. Academic Press, 1956.

[91] Stopper, U. *Weiterentwicklung und Anwendung der Laser-Raman-Streuung zur Untersuchung industrieller Vormischflammen in einer Hochdruckbrennkammer*. PhD thesis, Deutsches Zentrum fr Luft- und Raumfahrt Institut fr Verbrennungstechnik Stuttgart, 2013.

[92] Stopper, U., Meier, W., Sadanandan, R., Stöhr, M., Aigner, M., and Bulat, G. Experimental study of industrial gas turbine flames including quantification of pressure influence on flow field, fuel/air premixing and flame shape. *Combustion and Flame*, 160(10):2103–2118, 2013.

[93] Sung, C. J., Law, C. K., and Chen, J.-Y. Augmented reduced mechanisms for NO emission in methane oxidation. *Combustion and Flame*, 125(1-2):906–919, 2001.

[94] Toro, E. F. *Riemann Solvers and Numerical Methods for Fluid Dynamics*. Springer, 3rd edition, 2009.

[95] Triantafyllidis, A., Mastorakos, E., and Eggels, R. L. G. M. Large Eddy Simulations of forced ignition of a non-premixed bluff-body methane flame with Conditional Moment Closure. *Combustion and Flame*, 156:2328–2345, 2009.

[96] Truesdell, C. Mechanical Basis of Diffusion. *The Journal of Chemical Physics*, 37 (10):2336–2344, 1962.

[97] Truesdell, C. *Rational Thermodynamics*. Springer-Verlag, second edition, 1984.

[98] Truesdell, C. and Noll, W. *The Non-Linear Field Theories of Mechanics*. Springer, 2004.

[99] Truesdell, C. and Toupin, R. *Principles of Classical Mechanics and Field Theory*, volume III/1 of *Encyclopedia of Physics*. Springer-Verlag, 1960.

[100] Truffin, K. and Poinsot, T. Comparison and extension of methods for acoustic identification of burners. *Combustion and Flame*, 142:388–400, 2005.

[101] Tsien, H. S. The Transfer Functions of Rocket Nozzles. *Journal of the American Rocket Society*, pages 139–143, 1952.

[102] Uhlmann, M. Calculation of Compressible Flow Using TVD Schemes on a Collocated Grid. Master's thesis, Imperial College London, 1992.

[103] Vilyunov, V. N. and Ryabinin, V. K. Oscillations in the burning of hydrogen in a well-stirred reactor at low pressures. *Combustion, Explosion and Shock Waves*, 27 (2):203–211, 1991.

[104] Wang, H. and Laskin, A. A Comprehensive Kinetic Model of Ethylene and Acetylene Oxidation at High Temperatures. Technical report, University of Delaware, 1999.

[105] Warnatz, J. The Structure of Laminar Alkane-, Alkene-, and Acetylene Flames. *Symposium (International) on Combustion*, 18(1):369–384, 1981.

[106] Warnatz, J., Maas, U., and Dibble, R. W. *Combustion – Physical and Chemical Fundamentals, Modeling and Simulation, Experiments, Pollutant Formation*. Springer, 2006.

[107] Woolley, R. Private Communication, 2015.

[108] Yang, J., Mossa, F. M. S., Huang, H. W., Wang, Q., Woolley, R., and Zhang, Y. Oscillating flames in open tubes. *Proceedings of the Combustion Institute*, 35: 2075–2082, 2015.

[109] Yoo, C. S. and Im, H. G. Characteristic boundary conditions for simulations of compressible reacting flows with multi-dimensional, viscous and reaction effects. *Combustion Theory and Modelling*, 11(2):259–286, 2007.

[110] Zambon, A. C. and Chelliah, H. K. Self-sustained acoustic-wave interactions with counterflow flames. *Journal of Fluid Mechanics*, 560:249–278, 2006.

[111] Zhong, X. and Shu, C.-W. A simple weighted essentially nonoscillatory limiter for RungeKutta discontinuous Galerkin methods. *Journal of Computational Physics*, 232:397–415, 2013.

[112] Zhou, R. Turbulence Parameters for Non-Reacting conditions of Cambridge Stratified Swirl Burner. Technical report, Cambridge University, 2012.